To the Graduate Council:

I am submitting herewith a dissertation written by Lutz Blätte entitled "Vortex Driven Acoustic Flow Instability." I have examined the final electronic copy of this dissertation for form and content and recommend that it be accepted in partial fulfillment of the requirements for the degree of Doctor of Philosophy, with a major in Aerospace Engineering.

Gary Flandro, Major Professor

We have read this dissertation
and recommend its acceptance:

John Steinhoff

Trevor Moeller

Christian Parigger

Accepted for the Council:

Carolyn R. Hodges

Vice Provost and Dean of the Graduate School

(Original signatures are on file with official student records.)

Vortex Driven Acoustic Flow Instability

A Dissertation Presented for
the Doctor of Philosophy
Degree
The University of Tennessee, Knoxville

Lutz Blätte

May 2011

Acknowledgements

I would first like to acknowledge my advisor, Dr. Flandro, for inviting me into his research group, for sharing his wisdom in many thrilling and enlightening classes and for helping and guiding me through the many pitfalls related to Combustion Instability and the many vagaries unrelated to Combustion Instability. I highly appreciate the advice from the other members of my committee as well.

Furthermore, Keith Walker and Joel Davenport have been tremendously helpful in my experimental struggles and an inexhaustible source of skill and knowledge. Get well soon, Keith!

I'd also like to thank Dr. Eric Jacob for fostering and supporting me countless times - as well as for being a good friend. Without you I couldn't have done it. The same applies to Andrew Wilson and Josh Batterson, thank you for patiently answering all my stupid questions over the years.

Finally, I would like to thank my family for their everlasting support, all my friends I've made at UTSI and all my friends who didn't forget me while I was gone.

Mephistopheles:

Grau, teurer Freund, ist alle Theorie

und grün des Lebens goldner Baum.

-Johann Wolfgang von Goethe, Faust I, 1806

Abstract

Most combustion machines feature internal flows with very high energy densities. If a small fraction of the total energy contained in the flow is diverted into oscillations, large mechanical or thermal loads on the structure can be the result, which are potentially devastating if not predicted correctly. This is particularly the case for lightweight high performing devices like rockets. The problem is commonly known as "Combustion Instability". Several mechanisms have been identified in the past that link the flow field to the acoustics inside a combustion chamber and thereby drive or dampen oscillations, one of them being vortex shedding.

The interaction between the highly sheared flow behind an obstacle and longitudinal acoustic oscillations inside a solid rocket booster is investigated both analytically and experimentally. The analytical approach is developed based on modeling of the second order acoustic energy. The energy model is applied to the specific flow conditions just downstream of a single baffle protruding into the flow. The mean flow profile is assumed to be of the form of a hyperbolic tangent, the unsteady acoustic velocities are assumed to be sinusoidally oscillating. Solutions for the unsteady rotational velocities and the unsteady vorticity are derived. The resulting flow field is utilized in stability calculations for a simplified two-dimensional axial-symmetric geometry. This yields to linear growth rates of the (longitudinal) oscillation modes. The growth rates are functions of the chamber geometry, the mean flow properties and the properties of the shear layer created by the flow restriction.

A cold flow experiment is designed, tested and performed in order to validate the analytical findings. Flow is injected radially into a tube with acoustic closed-closed end conditions. A

single baffle is installed in the tube, the axial position of the baffle is varied as well as its inner diameter. Frequency spectra of pressure oscillations are recorded.
The experimental data is then compared qualitatively to the analytical growth rates. Those longitudinal Normal Modes, which feature the highest theoretical growth rates, are expected to be most prominent in the experimental data. This behavior is clearly observable.

Contents

List of Figures

Chapter 1

Introduction

Combustion instability has been and still is the major problem in rocket propulsion. Problems with unwanted and unexpected oscillations of the propulsion system have been the reason why many of the ambitious programs that appeared in the last 30 years were canceled at some (advanced) point in their development. The most recent example of this is the termination of the constellation program that was supposed to replace the aging space shuttle. Combustion instability can be a problem for solid propellant boosters, for liquid engines and for hyrbids as well. In fact, almost all propulsion and power generating devices are prone to the problem. It seems to be a natural phenomenon that a small fraction of the total energy of a flow with very high energy density goes into oscillations. Figure 1.1 depicts a typical example of the pressure trace of a firing of a solid rocket motor that exhibits heavy vibrations. Sometimes the symptoms can be cured by adding auxiliary systems that dampen the vibrations, but evading the problem in this fashion is problematic, especially for high performance light weight devices like rockets. A fix like this inevitably increases weight and complexity (and cost). On the other hand, even ”minor” oscillations usually can't be simply ignored if the safety factor of the structure is in the range of 1.1 to 1.3, as it typically is for rockets. Therefore, combustion instability needs to be tackled at its source so that the problem not only is alleviated but eliminated. In order to do so, the vastly complex physics of the internal flow inside the combustion chamber need to be thoroughly analyzed, and the

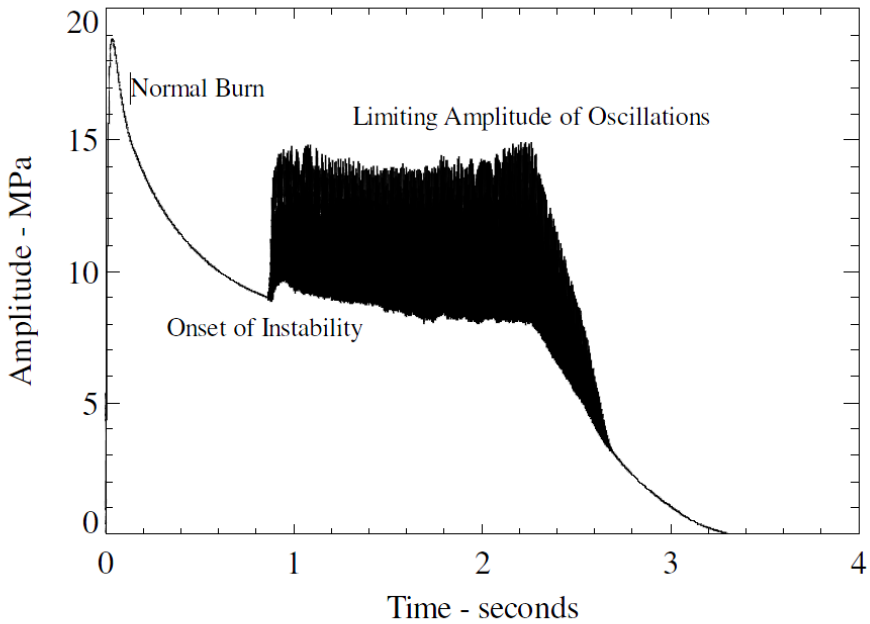

Figure 1.1: Example Pressure Plot from a Solid Rocket Motor [1]

mechanisms that link the flow field to the acoustics and thereby drive or dampen oscillations need to be identified.

Computational, experimental and analytical methods have to work hand in hand to achieve this challenging goal. While performing experiments can be time consuming and expensive, nowadays great hopes are set on computational analyses with their ever increasing processing power. CFD solutions certainly provide very valuable insights but cannot be trusted if the underlying physics of the fluid remain obscure. Especially the analytical approach provides a fast and effective way to identify physical mechanisms. For this reason, experimental and analytical work still is indispensable.

In fact, the term ”combustion instability” is misleading. Many examples show that often the combustion process itself has little or nothing to do with the occurrence of oscillations [2] [3]. Oscillations are driven by interactions between the flow field and the acoustics, much like in a simple system like a flute - only on a larger scale, with more severe consequences. Therefore the term ”flow instability” appears to be more appropriate.

Oscillations of the flow are sustained if the net change of oscillatory energy is greater or equal to zero and decay if it is less than zero. Mechanisms that increase the oscillatory energy typically link the mean flow to the internal acoustics and enable a transfer of energy from the mean flow into oscillations. Some of these mechanisms are boundary layer pumping [2], distributed combustion [5] [6], the propellant burning response [7] or vortex shedding [8] [9]. Counteracting mechanisms that dissipate the oscillatory energy are particle damping [10] [11], flow turning [12], viscous damping [13], nozzle damping [14] and others.

A number of large solid rocket motors, including Ariane 5 [15], Space Shuttle [16] or Titan family [17], are reported to exhibit instabilities during operation. Vortex shedding seems to be the major driving mechanism for these instabilities.

The work presented here focuses on this aspect, strictly speaking on the interaction between unsteady vorticity created by the highly sheared flow behind an obstacle and longitudinal acoustic oscillations inside a solid rocket motor.

1.1 Vortex Shedding in Solid Propellant Motors

Often the internal flow in the combustion chamber of solid propellant motors is prone to vortex shedding. Vortices are shed wherever the internal geometry causes the flow to separate.

Figure 1.2 shows a schematic of a solid motor with an internal geometry that features potential points of flow separation. These points can be backward facing steps in the propellant profile ("corner vortex"), obstacles like inhibitors protruding into the flow ("obstacle vortex") or unstable boundary layers at the burning surfaces ("parietal vortex"). For various reasons not all sources of vortex shedding can be eliminated from (large) solid propellant rocket motors. The thrust profile of a solid motor is controlled only by the burning surface area of the propellant grain. The area of a simple cylindrical grain shape monotonically increases as the propellant regresses. Therefore the thrust continuously increases over the burn time, which can be unfavorable for certain missions. Hence, more complex geometries can be required that include steps in the propellant surface which can lead to the creation of shear layers and vortex shedding. Figure 1.3 depicts the burn back of a more elaborate grain design.

Most solid rockets also feature inhibitors which are typically annularly shaped and serve for various purposes. Mainly they prevent certain surfaces of the propellant from igniting and therefore provide control over the burning area. This of course means that they regress at a slower rate than the propellant, if at all, which makes them protrude into the flow. Furthermore, inhibitors stabilize the grain mechanically, which is essential, if it is subjected to vibrations. Any irregularities in the propellant like cracks or bubbles cannot be tolerated, since they alter the burning surface and therefore the thrust profile and pressure uncontrollably. Lastly, segmentation of the rocket with inhibitors enables the disassembly of the pressure vessel. This can be required for transportation or by the casting process of the propellant into the motor casing.

Different mechanisms for the coupling of the internal acoustics and vortex shedding have been identified. One corresponds to the interaction of an unstable shear layer and acoustic

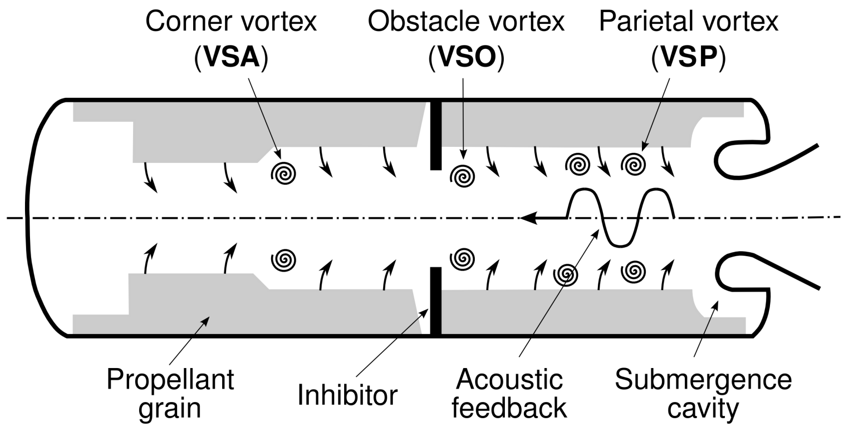

Figure 1.2: Sources of Vortex Shedding [18]

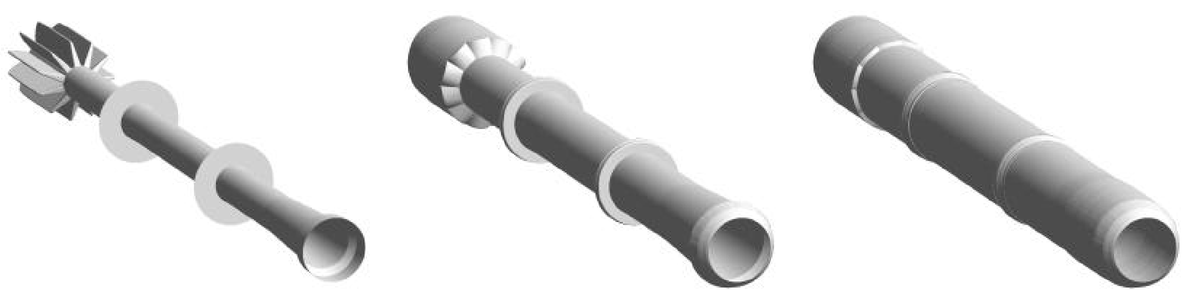

(a) Time=0.5 Seconds (b) Time=52.5 Seconds (c) Time=108.3 Seconds

Figure 1.3: ASRM Test Motor Burn Back at Different Time Steps [19]

pressure oscillations. A non-dimensional parameter that characterizes this effect is the Strouhal number, for this case defined by Vuillot [9] as:

$$\mathrm{St} = \frac{f\theta}{\Delta U_e} \tag{1.1}$$

This definition is based on the properties of the shear layer, as θ signifies its thickness and ΔU_e the velocity difference across it. The frequency of the vortex shedding is denoted by f. A different but similar definition is used by Brown et al. [17]. They investigated the effect of baffles protruding into the internal flow on pressure oscillations of the Titan 34D booster.

$$\mathrm{St} = \frac{fD}{U} \tag{1.2}$$

D stands for the inner diameter of the baffle and U for the flow speed. For given flow conditions the shear layer thickness θ and the diameter D are undoubtedly related. A value of the Strouhal number of the order of or less than unity is considered critical for the apparition of instabilities [17].

Another mechanism which can drive pressure oscillations is periodic impingement of vortices on a hard surface. This potentially occurs if the geometry features cavities, such as two obstacles close to each other or abrupt steps in the propellant surface. Since the underlying physics of this cavity flow type process are different, the corresponding Strouhal number is defined as:

$$\mathrm{St} = \frac{fl}{U} \tag{1.3}$$

Here l signifies the standoff distance between the point of flow separation and the point of impingement.

The standoff distances in large solid rocket boosters are typically large as well. Considering the highly turbulent internal flow, it is questionable whether a coherent vortex would exist long enough to travel the distance l.

1.2 Examples of Vortex Driven Flow Instability

Most of the research efforts to understand the mechanisms for vortex shedding driven oscillations were conducted with the development of large segmented solid propellant boosters, such as the Space Shuttle, Titan and Ariane 5 booster. All of these motors developed low level pressure and thrust oscillations although they were predicted stable by classical stability prediction codes [1]. The Amplitudes were typically less than 0.5% for the pressure and less than 5% for thrust oscillations [9]. Even these low level oscillations translate into significant alternating forces on the structure of the launch vehicle because of the high thrust level. Furthermore the large size of the boosters causes oscillations to occur at low frequencies at the order of 10-20 Hz, which is typically close to the natural frequencies of the structure, the payload - or for man rated vehicles, the crew. Resonance with any of the above is highly dangerous.

1.2.1 Minuteman III, 3rd Stage

The third stage of the Minuteman III ICBM is a clear example of vortex driven flow instability [8]. The internal configuration of the propellant grain causes the formation of strong shear layers and vortex shedding as the flow passes over it. The vortices travel downstream and impinge on the nozzle entrance of the motor. This porcess is depicted in figure 1.4. The flow conditions and internal geometry are subjected to constant change as the propellant burns back. This means that both the frequency of the vortex shedding and the standoff

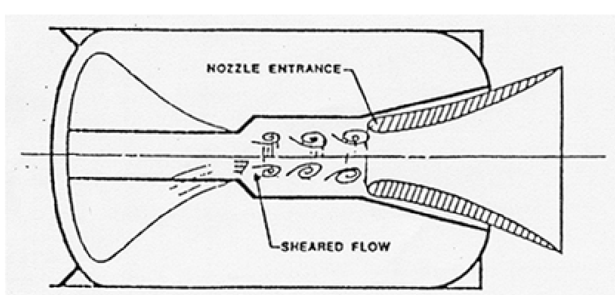

Figure 1.4: Minuteman III Internal Flow [20]

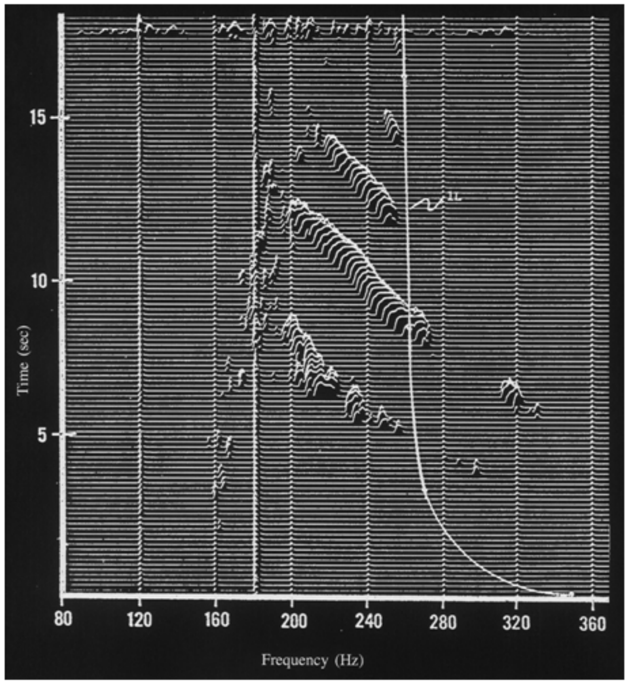

Figure 1.5: Typical Pressure Amplitude Waterfall for Minuteman III, Third Stage [21]

distance between the point of flow separation and the impingement vary in time. Oscillation amplitudes are highest when the impinging frequency happens to resonate with a natural frequency of the chamber. Since the pressure oscillations also alter the vortex shedding frequency, the chamber acoustics and the vortex shedding are coupled. This "locking in" phenomenon can be seen in figure 1.5. The instability problem was solved by smoothing out the abrupt steps in the propellant surface, which almost completely eliminated the vibrations [22].

1.2.2 Titan Solid Rocket Motor

The Titan family of launch vehicles has been the workhorse in America's fleet of expendable launch vehicles for over half a century. Since 1959 various configurations have launched, later models feature strap on solid boosters for increased payload and performance. The heritage of the Titan family can be seen in figure 1.6. Each booster comprises three, five, five and a half or seven segments, depending on the model and configuration. These segments are separated

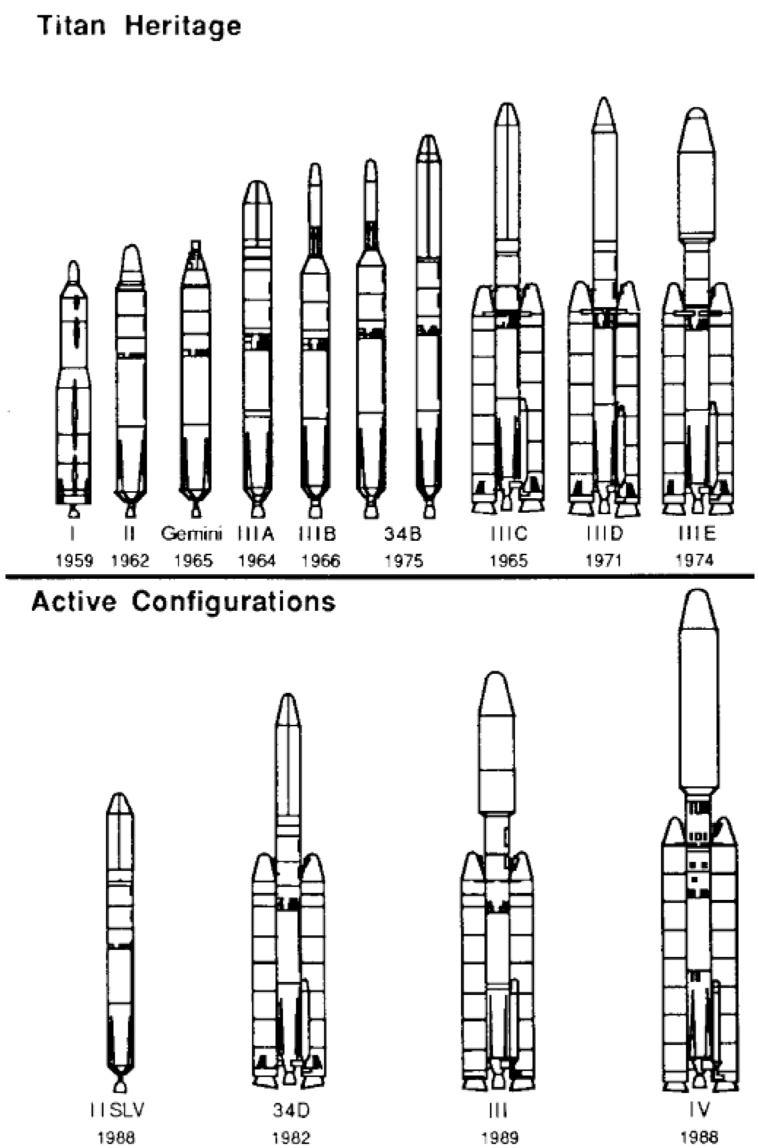

Figure 1.6: Titan Launch Vehicle Family [23]

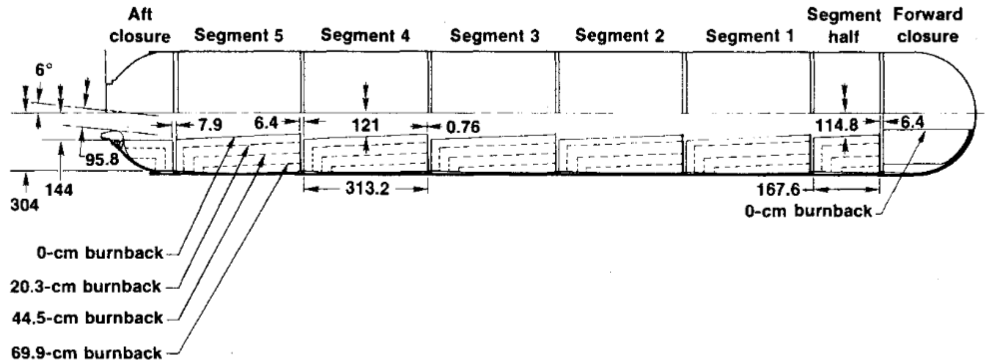

Figure 1.7: Schematic of Titan 34D SRM [17]

by inhibitors that protrude into the flow as the propellant burns back. A schematic of the propellant configuration and burnback is given in figure 1.7. Brown et al. report pressure oscillations of the full scale Titan 34D solid rocket motor with amplitudes of approximately 2% of the mean pressure [17]. The Frequencies of these oscillations match the first and second longitudinal mode of the motor with 23Hz and 47Hz respectively. These findings are validated with subscale hot and cold flow experiments. Figure 1.8 shows a waterfall plot of the instabilities during a firing of a full scale Titan 34D motor. Brown et al. conclude that the oscillations are driven by vortices shed from the inhibitors [17]. However, stability calculations performed for the first four longitudinal modes with the Standard Stability Prediction Method for Rocket Motors [24] predicts these modes to be stable throughout the burn.

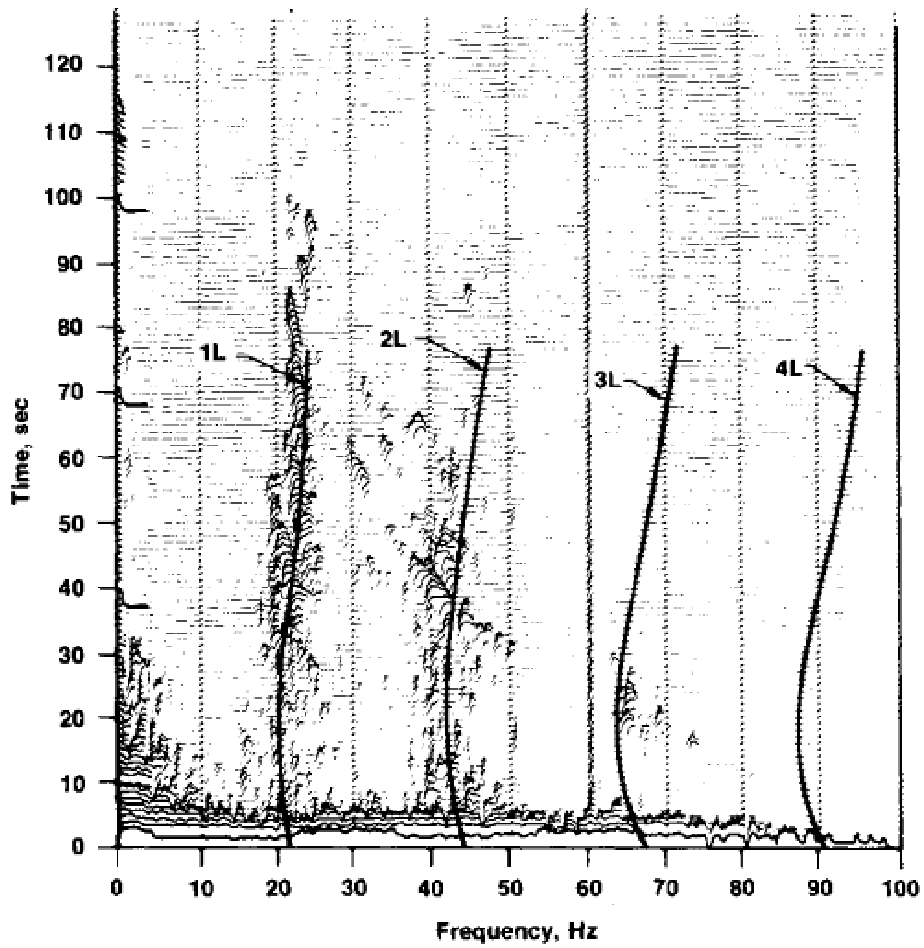

Figure 1.8: Waterfall Plot of Titan 34D Firing [17]

1.2.3 Ariane 5 MPS 230

The Ariane 5 launch vehicle is boosted by a pair of large solid rocket motors with a diameter of 3 meters and an overall motor length of 27 meters. The two solid rocket motors deliver more than 90% of the thrust level required during the first two minutes of flight.

The large propellant mass of 237 tons is distributed on three segments. The small forward segment holds 23 tons of propellant and features a star shaped grain, in order to deliver the take-off thrust level. The central and aft segments carry about 107 tons of propellant each. A schematic view of the Ariane 5 MPS 230 motor is given in figure 1.9. Unlike other motors it does not feature inhibitor rings but still exhibits oscillations characteristic for vortex shedding driven flow instability. Figure 1.10 shows a waterfall plot of these instabilities during a firing of a full scale MPS 230 motor. Lupoglazoff and Vuillot identify a slightly different mechanism that leads to the formation of vortices and driving of instabilities, called parietal vortex shedding [26]. Vortices are not generated by geometrical discontinuities but by hydrodynamic instabilities at the propellant surface. These vortices are convected with the flow and impact with the solid surface of the nozzle entrance. This is a periodic process, which can drive oscillations.

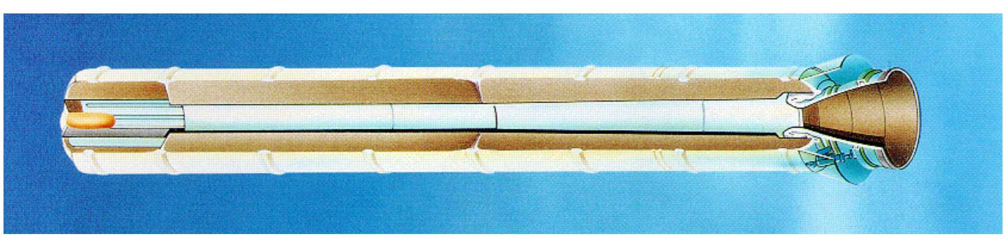

Figure 1.9: Schematic View of Ariane 5 MPS [25]

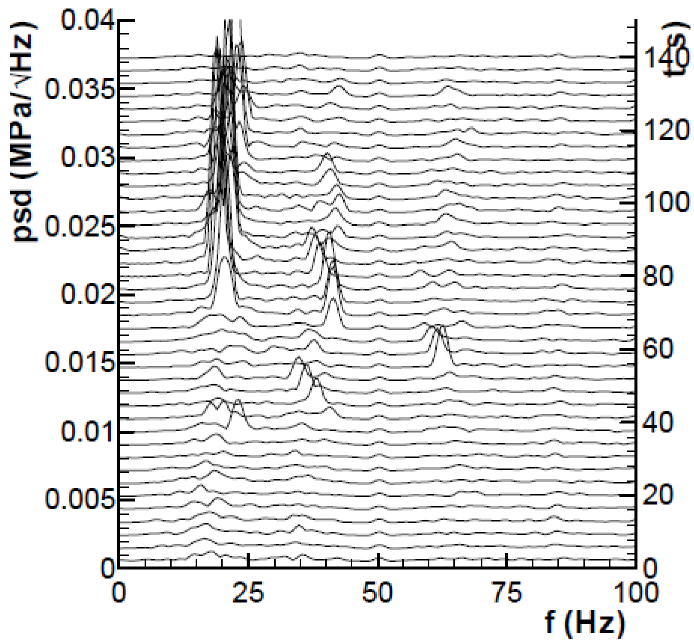

Figure 1.10: Waterfall Plot of Ariane 5 MPS Firing [25]

1.2.4 Space Shuttle Booster and Ares I

The Space Shuttle utilizes thrust provided by a combination of the Shuttle's main engines and two solid propellant rocket booster motors for liftoff and early ascent. The booster motors burn for approximately 2 minutes. Because of their size, the motors are manufactured in four sections which are assembled prior to launch. The motors have a 12 feet diameter and are 126 feet long. They contain over 1.1 million pounds of propellant and produce 2.6 millions pounds of thrust [27].

Combustion instability was considered in the system from the very early days of development. The instabilities are believed to be caused by coupling between large scale vortices and the acoustic modes of the motor chamber. The vortices are thought to be created in the region of the motor segment interfaces and are inherent in the design of the motor [28]. Measurements on the boosters detected first and second mode longitudinal oscillations on the order of one to three psi peak-to-peak. This appears to be relatively low, considering that the mean pressure is 600-800psi, but due to the large size of the boosters, pressure oscillations with an amplitude of 1psi translate into 33,000lbs of thrust oscillations. Oscillations of the first mode are plotted in figure 1.11.

The first mode frequency is 14Hz. It turns out that this is a frequency that is very close to the human brains reaction time to external stimuli. There was some worry by NASA that the booster oscillations might interfere with the astronaut's abilities to control the vehicle. Fortunately, this was not the case, although astronauts are warned and feel the vibrations during booster operation [27].

However, the vibrations caused by the boosters have not been problematic to the structure or systems of the Space Shuttle orbiter, presumably because of the configuration of the boosters. They are connected to the orbiter only through the main tank which acts as a vibration damper.

The Space Shuttle solid rocket booster has been adapted for future use in both the ARES I and ARES V flight vehicles. The first stage of Ares I consists of an extended version of a Space Shuttle booster, to which a fifth section has been added. A schematic view

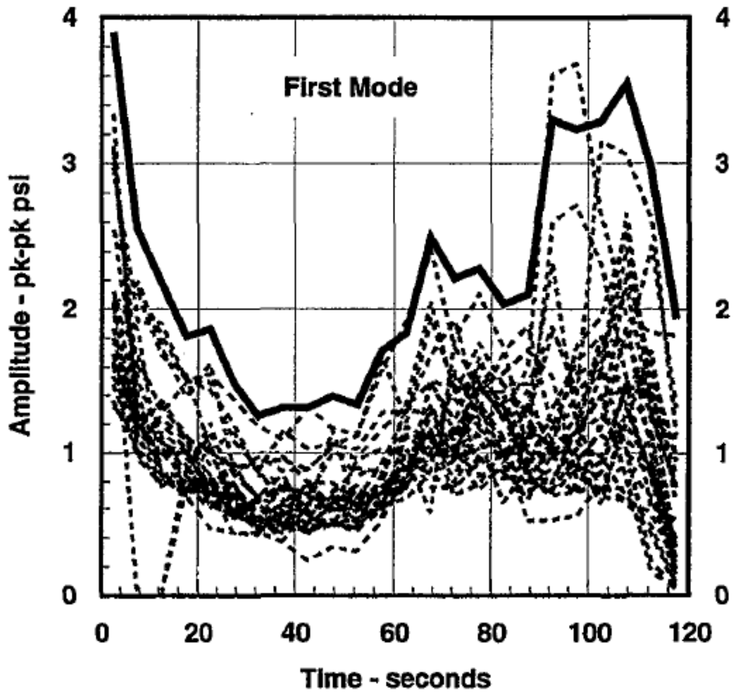

Figure 1.11: Space Shuttle Booster First Mode Pressure Oscillations [29]

of the ARES I vehicle is shown in figure 1.12. The first stage exhibits similar oscillation like the Shuttle booster, but the increase in length decreases the fundamental harmonic to approximately 12Hz. Unlike the space shuttle, the ARES I vehicle has structural harmonics near to the frequencies created by the motor. This causes the structure to resonate and imposes large accelerations on the rocket, large enough that the astronauts lives and the integrity of the rocket itself are endangered [31].

The oscillation problem of the ARES I vehicle could not be solved and finally led to the cancellation of the program at a very advanced stage.

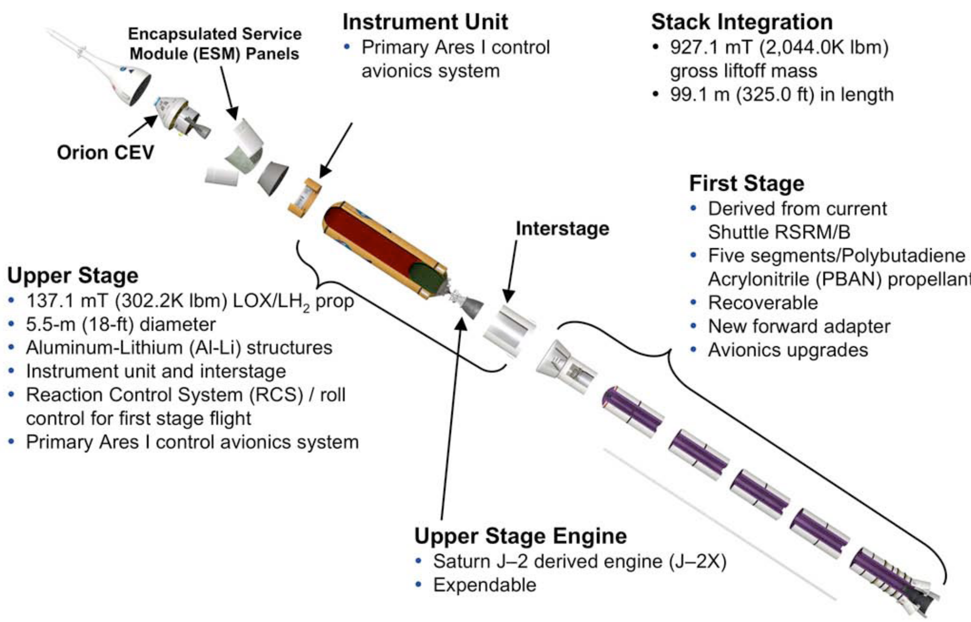

Figure 1.12: ARES I Vehicle Launch Vehicle [30]

1.3 Other Remarkable Examples in History

1.3.1 Brownlee-Marble Experiments

The experiments performed by Brownlee and Marble in 1959 at the Caltech Jet Propulsion Laboratory provided one of the first complete data sets on the combustion instability problem of solid propellant motors [32] [33] [34]. The experimental setup is shown in figure 1.13. More than 400 firings of a 5 inch solid rocket motor were recorded. Important nonlinear features like the mean pressure increase (or "DC-shift") or the formation of limit cycle amplitudes were manifested for the first time. Culick [35] recognized the great value of Brownlee's data set as a vehicle for testing theoretical models. Flandro et al. analysed the data using current analytical methods [3], a comparison between experiment and analytics is given in figure 1.14.

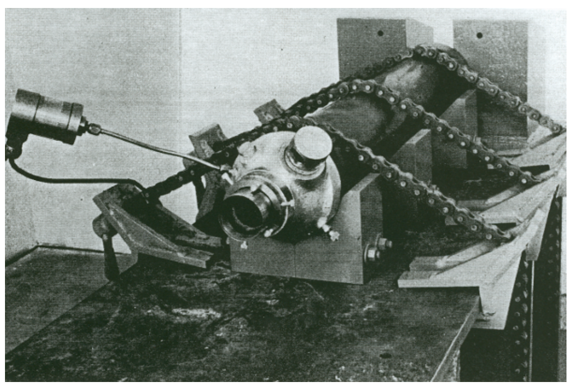

Figure 1.13: Experimental Setup of 5in Motor [33]

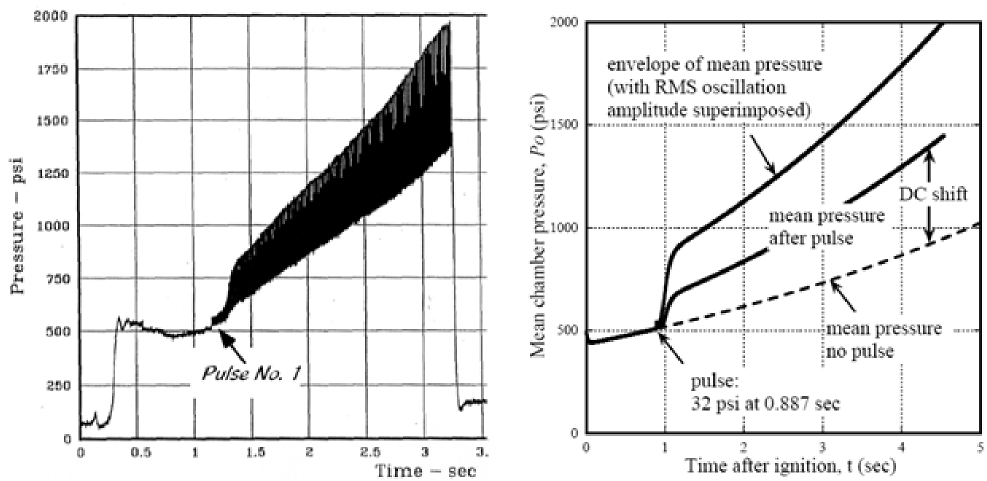

Figure 1.14: Experimental Data (left) vs. Simulation Data (right) [3]

1.3.2 Rocketdyne F-1 Engine

The Rocketdyne F-1 Engines were liquid engines running on RP1 jet fuel and liquid oxygen. This example is mentioned here, because how the solution to their vibration problems was found, is truly remarkable, even though the fluid physics of liquid engines and solid boosters are not closely related.

Five F-1 Engines were used in the first stage of the famous Saturn V rocket, the launch vehicle for the Apollo and Skylab programs from 1967 to 1973. The Saturn V still remains the largest and most powerful launch vehicle ever brought to operational status from a height, weight and payload standpoint, with each of the F-1 Engines producing over 1.5 million pounds of thrust. A F-1 engine is depicted in figure 1.15. The motors encountered serious combustion instability problems during the development phase [4]. Figure 1.16 shows a pressure trace. Peaks of the oscillation amplitudes reach roughly 1000psi which is on the same order as the "on design" mean chamber pressure of 965psi. The severe local overpressure causes the engine to fail due to burning and melting of the delicate injector surface. A damaged injector surface can be seen in figure 1.17(a). The problem could be traced back to tangential oscillations in the chamber and their interaction with the injection process [4]. In order to break up the coherent wave structure baffles were added to the original design, which reduced the oscillation amplitudes to a acceptable level of 10% of the mean pressure. Figure 1.17(b) shows the improved design of the injector.

With a time frame of less than 10 years but virtually unlimited funds, the lack of insight of the physics of the flow forced the designers to follow a trial and error approach. In the end over 2700 full scale tests had been necessary to find an operational configuration. This would be simply impossible with today's tight budgets.

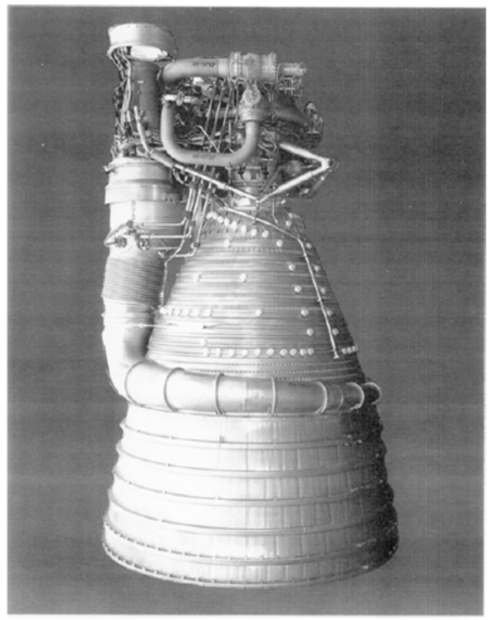

Figure 1.15: F-1 Liquid Rocket Engine [4]

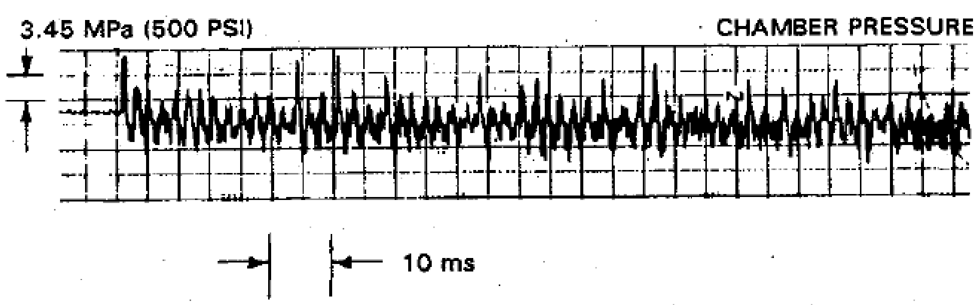

Figure 1.16: F-1 Example Pressure Trace [4]

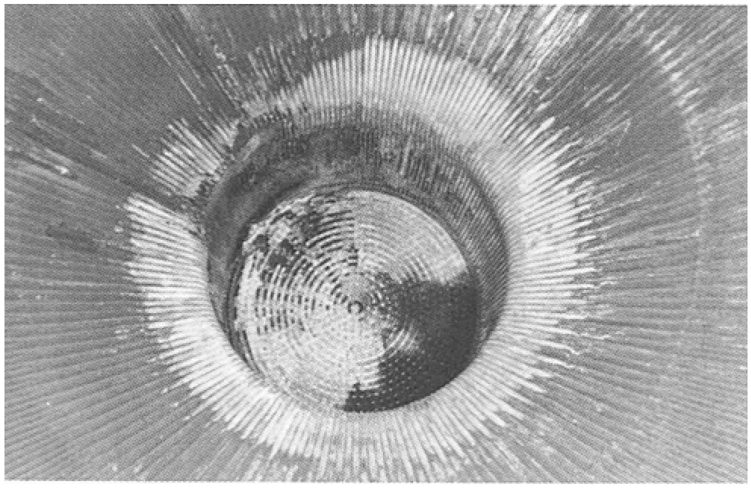

(a) Original Design

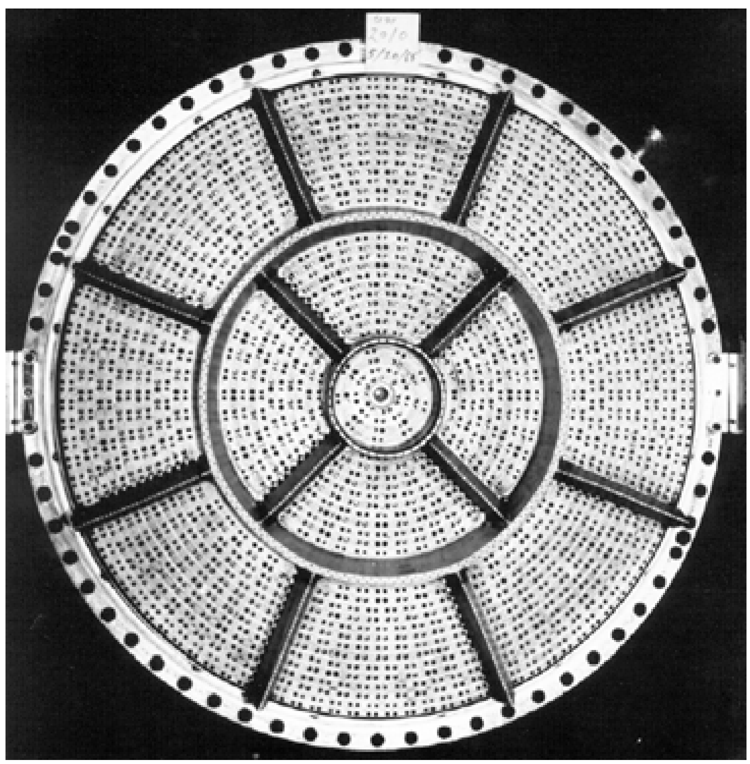

(b) Modified Design

Figure 1.17: F-1 Injector Plate [4]

Chapter 2

Genesis of Applicable Theory

The stability of a rocket motor is determined by the balance of acoustic energy gains and losses. A motor is considered stable if the net change of acoustic energy is equal to or less than zero. In this case oscillations are not sustained and decay over time. Therefore, in order to make a prediction on a motor's stability, the flux of energy from the mean flow (and the combustion) into the acoustics have to be carefully traced.

The principle of energy conservation in a acoustic system is well known. The change in the oscillatory energy must equal the work done on the system in addition to the energy sources [36].

$$\frac{\partial E}{\partial t} + \nabla \cdot W = D \tag{2.1}$$

E is the system energy, W the total work done on the system and D the summation of all energy sources and sinks. Early acoustic stability calculations were conducted for "classical" cavities where there is no steady-state flow field and there is an absence of acoustic disturbances.

However, the effect of mean flow is often of considerable importance, and the extent to which flow tends to excite or damp the acoustic field is related to mode configuration and flow-field geometry. Cantrell and Hart addressed this problem considering homentropic, irrotational flow [37]. They use the equations for conservation of mass, momentum and energy, which are expanded to second order. The resulting relations are combined in such a way that leads to a single growth-rate expression for acoustic oscillations. Morfey extends the concept of acoustic energy to non-uniform flows [38].

Myers then establishes the full energy balance for an arbitrary case including entropy fluctuations [36]. The individual terms in equation 2.1 are expressed as:

$$E = \rho \left[H - H_0 - T_0 \left(s - s_0 \right) \right] - \mathbf{m}_0 \cdot \left(\mathbf{u} - \mathbf{u}_0 \right) - \left(p - p_0 \right) \tag{2.2}$$

$$\begin{aligned} W = {} & \left(\mathbf{m} - \mathbf{m}_0 \right) \left[H - H_0 + T_0 \left(s - s_0 \right) \right] + \mathbf{m}_0 \left(T - T_0 \right) \left(s - s_0 \right) \\ & - \left(m_j - m_{0_j} \right) \left(\frac{P_{ij}}{\rho} - \frac{P_{0_{ij}}}{\rho_0} \right) + \left(T - T_0 \right) \left(\frac{\mathbf{q}}{T} - \frac{\mathbf{q_0}}{T_0} \right) \end{aligned} \tag{2.3}$$

$$\begin{aligned} D = {} & \mathbf{m} \cdot \boldsymbol{\zeta}_0 + \mathbf{m}_0 \boldsymbol{\zeta} - \left(s - s_0 \right) \mathbf{m} \cdot \nabla T_0 + \left(s - s_0 \right) \mathbf{m}_0 \cdot \nabla T \\ & - \left(\frac{P_{ij}}{\rho} - \frac{P_{0_{ij}}}{\rho_0} \right) \frac{\partial}{\partial x_i} (m_j - m_{0_j}) + (m_j - m_{0_j}) \left(\frac{P_{ij}}{\rho^2} \frac{\partial \rho}{\partial x_i} - \frac{P_{0_{ij}}}{\rho_0^2} \frac{\partial \rho_0}{\partial x_i} \right) \\ & + \left(T - T_0 \right) \left(\frac{\phi}{T} - \frac{\phi_0}{T_0} \right) + \left(\frac{\mathbf{q}}{T} - \frac{\mathbf{q_0}}{T_0} \right) \cdot \nabla (T - T_0) \\ & - \left(T - T_0 \right) \left(\frac{\mathbf{q} \cdot \nabla T}{T^2} - \frac{\mathbf{q_0} \cdot \nabla T_0}{T_0^2} \right) \end{aligned} \tag{2.4}$$

P_{ij} denotes the components of the viscous stress tensor, while ϕ is the dissipation function.

$$P_{ij} = \mu \left(\frac{\partial u_j}{\partial x_i} + \frac{\partial u_i}{\partial x_j} - \frac{2}{3} \delta_{ij} \frac{\partial u_k}{\partial x_k} \right) + \eta \delta_{ik} \frac{\partial u_k}{\partial x_k} \tag{2.5}$$

$$\phi = P_{ij} \frac{\partial u_i}{\partial x_i} \tag{2.6}$$

The vector $\boldsymbol{\zeta}$ is defined as:

$$\boldsymbol{\zeta} = \boldsymbol{\omega} \times \mathbf{u} \tag{2.7}$$

In this form these relations describe the acoustic energy flux in rocket motors. Current work from Flandro applies this to the combustion instability problem, eg. [3] [8] [39] [40] and many more. His work combines previous combustion instability analysis with the modern acoustic energy method which yields a more complete picture of the system and full understanding on interior motor dynamics and their impact on combustion instability, while making minimal assumptions.

Chapter 3

Combustion Instability Framework

The general combustion instability framework summarized here is based on work by Myers [36] and exactly follows the steps laid out by Flandro [41] and Jacob [42]. In chapter 5 this general framework will then be novelly applied to the vortex shedding case.

Every analysis of a fluid dynamics problem has to start with a complete set of governing fluid dynamics and thermodynamic equations. This complex system is handled using perturbation expansions for which each field variable is split into a slowly changing mean flow and oscillatory parts. Doing so, all important mechanisms that direct the flux of energy from the mean flow into oscillations unravel. Expansions are carried out up to the second order, so that the linear wave amplitude growth is captured.

3.1 Fluid Dynamic Relations

Three governing equations are required to fully define a fluid dynamics problem, a forth equation is a combination of any set of the three others. However, for convenience and completeness all four conservation relations are listed below. The derivation of the fluid mechanic equations is shown clearly in "Fluid Mechanics" by Landau and Lifshitz [43] and "Theory of Nonlinear Acoustics in Fluids" by Enflo and Hedberg [44].

Continuity:

$$\frac{\partial \rho}{\partial t} + \nabla \cdot \mathbf{m} = 0 \tag{3.1}$$

Momentum:

$$\frac{\partial \mathbf{u}}{\partial t} + \boldsymbol{\omega} \times \mathbf{u} + \nabla H - T \nabla s = \boldsymbol{\psi} \tag{3.2}$$

Entropy:

$$\frac{\partial \rho s}{\partial t} + \nabla \cdot (\mathbf{m} s) = Q \tag{3.3}$$

Energy:

$$\frac{\partial}{\partial t} (\rho H - p) + \nabla \cdot (\mathbf{m} H) - \mathbf{m} \cdot \boldsymbol{\psi} - T Q = 0 \tag{3.4}$$

Definitions:

$$\text{Enthalpy:} \qquad h = e + \frac{p}{\rho} \tag{3.5}$$

$$\text{Total Enthalpy:} \qquad H = h + \frac{1}{2} \mathbf{u}^2 \tag{3.6}$$

$$\text{Mass Flow Rate:} \qquad \mathbf{m} = \rho \mathbf{u} \tag{3.7}$$

$$\text{Vorticity:} \qquad \boldsymbol{\omega} = \nabla \times \mathbf{u} \tag{3.8}$$

$$\text{Zeta Vector:} \qquad \boldsymbol{\zeta} = \boldsymbol{\omega} \times \mathbf{u} \tag{3.9}$$

$$\text{Heat Release:} \qquad Q = \frac{\Phi - \nabla \mathbf{q} + \mathcal{H}}{T} \tag{3.10}$$

$$\boldsymbol{\psi} = \frac{1}{\rho} \left[-\mu \nabla \times \nabla \times \mathbf{u} + \left(\eta + \frac{4}{3} \mu \right) \nabla \left(\nabla \cdot \mathbf{u} \right) + \mathbf{F} \right] \tag{3.11}$$

$$\Phi = P_{ij} \frac{\partial u_j}{\partial x_i} \tag{3.12}$$

$$P_{ij} = {\sigma'}_{ij} = \mu \left(\frac{\partial v_i}{\partial x_j} + \frac{\partial v_j}{\partial x_i} - \frac{2}{3} \delta_{ik} \frac{\partial v_l}{\partial x_l} \right) + \eta \delta_{ik} \frac{\partial v_l}{\partial x_l} \tag{3.13}$$

$\mathcal{H}$ defines the distributed combustion heat release, $\mathbf{q}$ the heat transfer, $\boldsymbol{\psi}$ the viscous stress, η the bulk viscosity, μ the dynamic viscosity and $\mathbf{F}$ external body forces. Bold print signifies vector quantities.

3.2 Thermodynamic Relations

A set of three thermodynamic variables defines a system completely, additional relations have been stated for use in later algebra. More information on the thermodynamic equations can be found in Liepmann and Roshko's "Gas Dynamics" [45].

$$de = Tds + \frac{p}{\rho^2}d\rho \tag{3.14}$$

$$dh = Tds + \frac{1}{\rho}dp \tag{3.15}$$

$$dh = \gamma Tds + \frac{a^2}{\rho}d\rho \tag{3.16}$$

$$dp = \frac{a^2\rho}{c_p}ds + a^2 d\rho \tag{3.17}$$

$$dT = \frac{T}{c_p}ds + \frac{1}{\rho c_p}dp \tag{3.18}$$

$$dT = \frac{1}{c_p}\left(\gamma Tds + \frac{a^2}{\rho}d\rho\right) \tag{3.19}$$

Here p is the pressure, ρ is the density, T is the temperature, s is the entropy, e is the internal energy, h is the enthalpy, a is the speed of sound, γ is the specific heat ratio, and c_p is the constant pressure specific heat. Furthermore it is assumed that the gas is thermally perfect, so that:

$$p = \rho RT \tag{3.20}$$

The speed of sound is defined as:

$$\sqrt{\left(\frac{\partial p}{\partial \rho}\right)_s} = \sqrt{\gamma\left(\frac{\partial p}{\partial \rho}\right)_T} \tag{3.21}$$

Or for thermally perfect gas:

$$a = \sqrt{\gamma RT} \tag{3.22}$$

3.3 Introduction to Perturbation Methods

Trying to find an exact closed form solution to a complex fluid dynamics problem usually is simply hopeless. Exact solutions only exist for special cases. Solutions can be obtained numerically, but isolating and tracing back physical mechanisms is difficult because all individual contributions to the solution would be lumped into one final answer.

For this reason all modern analytical work by Cantrell and Hart [37], Myers [36] and Flandro [3] uses a different approach, so called perturbation techniques. These techniques make it possible to find closed form approximate solutions to almost all kinds of non-linear equations. They assume the existence of a small parameter ϵ and break down the governing equations into orders of magnitude. Each order of magnitude is solved individually and recombined to a general answer. Many advanced perturbation tools like WKB or generalized scales methods are available in the literature [46], but simple regular perturbations are sufficient for the problem discussed here.

Regular perturbation methods are based on the assumption that a solution to a differential equation $y(\mathbf{x}, t)$ with a recurring small parameter ϵ can be approximated by a series of successive solutions of the form:

$$y(\mathbf{x}, t) = y_0(\mathbf{x}, t) + \epsilon y_1(\mathbf{x}, t) + \epsilon^2 y_2(\mathbf{x}, t) + \epsilon^3 y_3(\mathbf{x}, t) + ... \tag{3.23}$$

Each new order of the solution $y_i(\mathbf{x}, t)$ contributes an increasingly small correction to the total approximate solution $y(\mathbf{x}, t)$.

$$\epsilon^{i+1} y_{i+1}(\mathbf{x}, t) \ll \epsilon^i y_i(\mathbf{x}, t) \tag{3.24}$$

The governing equations are broken down into orders of magnitude by expanding all thermodynamic and fluid dynamic field variables $q(\mathbf{x}, t)$ around ϵ. Physically speaking, the variables are split into a quasi steady mean flow parameter and higher order fluctuating corrections, which is an idea widely used in acoustics theory.

$$q(\mathbf{x}, t) = q_0(\mathbf{x}) + \sum_{n=1}^{\infty} \epsilon^n q_n(\mathbf{x}, t) \tag{3.25}$$

The leading order parameters $q_0(\mathbf{x})$ are assumed to be steady state as their change in time is considered negligible within the time scale of the oscillations.

The small parameter ϵ is justified by the fact that the magnitude of the oscillations of all variables are much smaller than their mean flow properties, thus:

$$\epsilon = \frac{q_1}{q_0} \ll 1 \tag{3.26}$$

Even though ϵ is not identical for all variables the successive approximation remains valid as long as the orders of magnitude are comparable.

3.4 Application of Perturbations

In order to gain insight into the flux of energy from the mean flow into oscillations, the governing fluid dynamics equations 3.1 through 3.4 are split into orders of magnitude as described in the previous section. All variables are expanded according to equation 3.25, substituted back and terms of matching orders of ϵ are carefully collected. Following Jacob [42], this process yields to the following relations:

Mean Flow (ϵ^0):

$$\nabla \cdot \mathbf{m}_0 = 0 \tag{3.27}$$

$$\boldsymbol{\zeta}_0 + \nabla H_0 - T_0 \nabla s_0 = \boldsymbol{\psi}_0 \tag{3.28}$$

$$\nabla \cdot (\mathbf{m}_0 s_0) = Q_0 \tag{3.29}$$

$$\nabla \cdot (\mathbf{m}_0 H_0) - \mathbf{m}_0 \cdot \boldsymbol{\psi}_0 - T_0 Q_0 = 0 \tag{3.30}$$

First Order (ϵ^1):

$$\frac{\partial \rho_1}{\partial t} + \nabla \cdot \mathbf{m}_1 = 0 \tag{3.31}$$

$$\frac{\partial \mathbf{u}_1}{\partial t} + \boldsymbol{\zeta}_1 + \nabla H_1 - T_0 \nabla s_1 - T_1 \nabla s_0 = \boldsymbol{\psi}_1 \tag{3.32}$$

$$\frac{\partial(\rho_0 s_1 + \rho_1 s_0)}{\partial t} + \nabla \cdot (\mathbf{m}_0 s_1 + \mathbf{m}_1 s_0) = Q_1 \tag{3.33}$$

$$\frac{\partial}{\partial t}(\rho H - p)_1 + \nabla \cdot (\mathbf{m}_0 H_1 + \mathbf{m}_1 H_0) - \mathbf{m}_0 \cdot \boldsymbol{\psi}_1 - \mathbf{m}_1 \cdot \boldsymbol{\psi}_0 - T_0 Q_1 - T_1 Q_0 = 0 \tag{3.34}$$

Second Order (ϵ^2):

$$\frac{\partial \rho_2}{\partial t} + \nabla \cdot \mathbf{m}_2 = 0 \tag{3.35}$$

$$\frac{\partial \mathbf{u}_2}{\partial t} + \boldsymbol{\zeta}_2 + \nabla H_2 - T_0 \nabla s_2 - T_1 \nabla s_1 - T_2 \nabla s_0 = \boldsymbol{\psi}_2 \tag{3.36}$$

$$\frac{\partial(\rho_0 s_2 + \rho_1 s_1 + \rho_2 s_0)}{\partial t} + \nabla \cdot (\mathbf{m}_0 s_2 + \mathbf{m}_1 s_1 + \mathbf{m}_2 s_0) = Q_2 \tag{3.37}$$

$$\frac{\partial}{\partial t}(\rho H - p)_2 + \nabla \cdot (\mathbf{m}_0 H_2 + \mathbf{m}_1 H_1 + \mathbf{m}_2 H_0)$$
$$- \mathbf{m}_0 \cdot \boldsymbol{\psi}_2 - \mathbf{m}_1 \cdot \boldsymbol{\psi}_1 - \mathbf{m}_2 \cdot \boldsymbol{\psi}_0 - T_0 Q_2 - T_1 Q_1 - T_2 Q_0 = 0 \quad (3.38)$$

To save time in further analysis the following notation may be used:

$$C_n = \text{continuity of order n}$$
$$L_n = \text{momentum of order n}$$
$$S_n = \text{entropy of order n}$$

Then the three fluid dynamic governing equations can be written as:

$$C = 0 \quad (3.39)$$

$$\mathbf{L} - \boldsymbol{\psi} = 0 \quad (3.40)$$

$$S - Q = 0 \quad (3.41)$$

3.5 Acoustic Energy Flux

The flux of acoustic energy is contained in the expansions of the energy equation 3.30, 3.34 and 3.38. The physics underlying the coupling between the mean flow and the oscillations unravel if these equations are carefully analyzed. It turns out that the leading and the first order energy represented in equation 3.30 and 3.34 yield to solutions that are mathematically correct, but don't hold any new physical information. The details of this can be seen in appendix A.3.

However, the second order equation produces a relation between the first order oscillatory field variables.

Recalling the second order energy equation 3.38

$$\frac{\partial}{\partial t}(\rho H - p)_2 + \nabla \cdot (\mathbf{m}_0 H_2 + \mathbf{m}_1 H_1 + \mathbf{m}_2 H_0) \\ - \mathbf{m}_0 \cdot \boldsymbol{\psi}_2 - \mathbf{m}_1 \cdot \boldsymbol{\psi}_1 - \mathbf{m}_2 \cdot \boldsymbol{\psi}_0 - T_0 Q_2 - T_1 Q_1 - T_2 Q_0 = 0$$

First the time derivative terms are expanded upon. The details of this expansion are laid out in great detail by Jacob [42] and involve power series expansions of the thermodynamic variables and a lot of tedious algebra. In the end one finds that:

$$(\rho H - p)_2 = H_0 \rho_2 + T_0(\rho_1 s_1 + \rho_0 s_2) + \frac{{p_1}^2}{2\rho_0 {a_0}^2} + \frac{\rho_0 T_0 {s_1}^2}{2c_p} \\ + \rho_1 \mathbf{u}_0 \cdot \mathbf{u}_1 + \frac{1}{2}\rho_0 {u_1}^2 + \mathbf{m}_0 \cdot \mathbf{u}_2 \quad (3.42)$$

To assist in the bookkeeping the following terms in the time derivative are combined as:

$$E_2 = \frac{{p_1}^2}{2\rho_0 {a_0}^2} + \frac{\rho_0 T_0 {s_1}^2}{2c_p} + \rho_1 \mathbf{u}_0 \cdot \mathbf{u}_1 + \frac{1}{2}\rho_0 {u_1}^2 \quad (3.43)$$

After applying the field variable expansions according to equation 3.25 and inserting the other second order governing equations 3.35, 3.36 and 3.37 and some simplifications the following expression is found:

$$\frac{\partial E_2}{\partial t} + (H_0 - T_0 s_0)\, C_2 + \mathbf{m}_0 \cdot (L_2 - \boldsymbol{\psi}_2) + T_0\,(S_2 - Q_2) \\ - T_0 \nabla \cdot (\mathbf{m}_1 s_1) - \mathbf{m}_0 \cdot \boldsymbol{\zeta}_2 + T_1 \nabla \cdot (\mathbf{m}_0 s_1) + \nabla \cdot (\mathbf{m}_1 H_1) \\ - \mathbf{m}_1 \cdot \boldsymbol{\psi}_1 - \mathbf{m}_2 \cdot \boldsymbol{\zeta}_0 - T_1 Q_1 = 0 \quad (3.44)$$

Special attention is directed to the vorticity terms, for they are obviously of great importance when analyzing vortex driven flow instability. First the ζ-vector is expanded to the second order:

$$\boldsymbol{\zeta}_2 = \boldsymbol{\omega}_0 \times \mathbf{u}_2 + \boldsymbol{\omega}_1 \times \mathbf{u}_1 + \boldsymbol{\omega}_2 \times \mathbf{u}_0 \quad (3.45)$$

Then the mass flow $\mathbf{m}$ is expanded as well:

$$\mathbf{m}_2 = \rho_0 \mathbf{u}_2 + \rho_1 \mathbf{u}_1 + \rho_2 \mathbf{u}_0 \quad (3.46)$$

Therefore, the second order vorticity terms simplify to:

$$\begin{aligned} \mathbf{m}_0 \cdot \boldsymbol{\zeta}_2 + \mathbf{m}_2 \cdot \boldsymbol{\zeta}_0 &= \rho_0 \mathbf{u}_0 \cdot (\boldsymbol{\omega}_0 \times \mathbf{u}_2 + \boldsymbol{\omega}_1 \times \mathbf{u}_1 + \boldsymbol{\omega}_2 \times \mathbf{u}_0) \\ &\quad + (\rho_0 \mathbf{u}_2 + \rho_1 \mathbf{u}_1 + \rho_2 \mathbf{u}_0) \cdot (\boldsymbol{\omega}_0 \times \mathbf{u}_0) \\ &= \rho_0 \mathbf{u}_0 \cdot (\boldsymbol{\omega}_1 \times \mathbf{u}_1) + \rho_1 \mathbf{u}_1 \cdot (\boldsymbol{\omega}_0 \times \mathbf{u}_0) \end{aligned} \quad (3.47)$$

Terms are then arranged into three parts, analogous to equation 2.1:

$$\frac{\partial E}{\partial t} + \nabla \cdot W = D$$

The time derivative terms represent the change of Energy, the divergence terms the work done to the system and the remaining terms energy sources and energy sinks, depending on whether D is positive or negative. The viscous and heat release components require some additional treatment which is not demonstrated here, because they will be dropped in the further analysis.

Writing equation 3.44 in the form of equation 2.1 gives:

$$E_2 = \frac{{p_1}^2}{2\rho_0 {a_0}^2} + \frac{\rho_0 T_0 {s_1}^2}{2c_p} + \rho_1 \mathbf{u}_0 \cdot \mathbf{u}_1 + \frac{1}{2}\rho_0 {u_1}^2 \tag{3.48}$$

$$W_2 = \mathbf{m}_1 \left(h_1 + \mathbf{u}_0 \cdot \mathbf{u}_1 - T_0 s_1\right) + \mathbf{m}_0 T_1 s_1 + T_1 \left(\frac{q}{T}\right)_1 - m_{1j} \left(\frac{P_{ij}}{\rho}\right)_1 \tag{3.49}$$

$$\begin{aligned} D_2 = -\mathbf{m}_1 s_1 \cdot \nabla T_0 + \mathbf{m}_0 s_1 \cdot \nabla T_1 - \rho_0 \mathbf{u}_0 \cdot (\mathbf{u}_1 \times \boldsymbol{\omega}_1) - \rho_1 \mathbf{u}_1 \cdot (\mathbf{u}_0 \times \boldsymbol{\omega}_0) \\ - \left(\frac{P_{ij}}{\rho}\right)_1 \frac{\partial m_{1j}}{\partial x_i} + m_{1j} \left(\frac{P_{ij}}{\rho^2} \frac{\partial \rho}{\partial x_i}\right)_1 \\ + T_1 \left(\frac{\phi}{T}\right)_1 + \left(\frac{q}{T}\right)_1 \cdot \nabla T_1 - T_1 \left(\frac{q \cdot \nabla T}{T^2}\right)_1 \end{aligned} \tag{3.50}$$

The equations 3.48, 3.49 and 3.50 represent the second order change of oscillatory energy in a closed system. They can be used to analyze the stability of the internal flow of a rocket with a given geometry. For this, they have to be integrated over the volume and time averaged. The resulting system can then be solved for the (linear) growth rates of the wave amplitudes. This process is illustrated in detail for the vortex shedding case in chapter 5.

Chapter 4

Principles of the Stability Analysis

The stability of a propulsion system can be defined in many ways. Since combustion instability is an inherent problem of almost all rockets, it is a common practice to consider a rocket stable, if it exhibits pressure oscillations of less than a certain percentage of the mean pressure. Finding a reliable definition for this percentage is difficult because which level of oscillations is tolerable depends on the propulsion system, the payload and the mission. Furthermore, a definition like this actually does not describe whether a system is stable, but only how unstable it is.

A more rigorous way to determine stability is to calculate the growth rates of the oscillation amplitudes for each mode individually. If the growth rate for a oscillatory mode is less than zero, the oscillation decays over time and this mode is considered to be stable. If the growth rate is greater than zero, energy is diverted form the mean flow into the oscillation which are therefore sustained and this mode is considered unstable.

Doing this requires an in depth analysis of the flow field for which the results from chapter 3 are utilized. The equations 3.48, 3.49 and 3.50 describe the local change of energy at any given time. Therefore the energy balance is integrated over the volume of the combustion chamber yielding the net change of energy in the system. Then the result is time averaged over one period of the oscillations. This is necessary because the problem involves two different time scales. The fast scale represents the oscillations of the fluid properties, the

slow scale the change of the oscillation amplitudes. Only the long term net change of the amplitudes is of interest, therefore the momentary (fast) oscillations are averaged out.
This process is a vastly complex. However, it can be simplified and organized by decomposing the fluctuating properties.

4.1 Decomposition of Fluctuating Properties

4.1.1 Galerkin Spectral Decomposition

Following Galerkin all fluctuating properties can be understood as a superposition of all harmonics with varying amplitudes for each mode [50]. If this is applied to the pressure and the amplitudes are scaled by the mean pressure P_0, for longitudinal oscillations we get:

$$p_1(\mathbf{r}, t) = P_0(t) \sum_{m=1}^{\infty} \eta_m(t) \, \psi_m(\mathbf{r}) \tag{4.1}$$

with the mode shapes

$$\psi_m(\mathbf{r}) = R_m(t) \cos(k_m z) \tag{4.2}$$

$$\eta_m(t) = \cos(\omega_m t) \tag{4.3}$$

and the dimensional wave number

$$k_m = \frac{m\pi}{L} = \frac{\omega_m}{a_0} = \frac{2\pi f_m}{a_0} \tag{4.4}$$

$R_m(t)$ signifies oscillation amplitude, m the mode number, L the chamber length and f_m the frequency of a mode. It is important to mention that the amplitudes $R_m(t)$ are considered to change slowly in time compared to the time scale of the oscillations.

4.1.2 Helmholtz Decomposition

The fundamental theorem of vector calculus states that any sufficiently smooth, rapidly decaying vector field in three dimensions can be resolved into the sum of an irrotational vector field and a solenoidal vector field. This theorem is also known as the Helmholtz decomposition. Applied to fluid dynamics this means that a flow field can be split into an irrotational compressible part and a rotational incompressible part. The irrotational part is defined by the gradient of a flow potential Φ, the rotational part by the curl of a stream function Ψ. This split greatly simplifies the further analysis and enables to trace back the energy flux and identify energy sources and sinks. Therefore the fluctuating velocity $\mathbf{u}_1$ is written as:

$$\mathbf{u}_1 = \hat{\mathbf{u}}_1 + \tilde{\mathbf{u}}_1 \tag{4.5}$$

Here $\hat{\mathbf{u}}_1$ signifies the compressible acoustic part, where $\tilde{\mathbf{u}}_1$ stands for the incompressible rotational part. Furthermore $\hat{\mathbf{u}}_1$ and $\tilde{\mathbf{u}}_1$ are defined as:

$$\hat{\mathbf{u}}_1 = \nabla\Phi \tag{4.6}$$

$$\tilde{\mathbf{u}}_1 = \nabla \times \Psi \tag{4.7}$$

4.2 Integration and Orthogonality

Generally speaking two functions $f(x)$ and $g(x)$ are considered orthogonal if

$$\int_a^b f(x)g(x)dx = 0. \tag{4.8}$$

Exactly this characteristic applies to many terms in the later analysis when performing the integration over the volume and taking the time average.

4.2.1 Volume Integral

In order to solve for the total system energy flux equation 2.1 is integrated over the volume.

$$\int_V \frac{\partial E_2}{\partial t} dV = \int_V D_2 dV - \int_V \nabla \cdot W_2 dV \tag{4.9}$$

The work integral is transformed into a surface integral using the Gauss theorem.

$$\int_V \frac{\partial E_2}{\partial t} dV = \int_V D_2 dV - \int_S \hat{n} \cdot W_2 dS \tag{4.10}$$

The left hand side represents the change in the fluctuating energy, the right hand side represents the volumetric energy production and surface energy flux. The right hand side yields the definition of α, the linear growth rate, or the change in oscillatory energy in time. Products of the mode shapes ψ_m are encountered frequently in the process of the integration over the volume. Knowing that $\psi_m = \cos(k_m z)$ and $k_m = m\pi/L$, where L is the chamber length and R the chamber radius

$$\int_V \psi_m \psi_n dV = \pi R^2 \int_0^L \psi_m \psi_n dz \tag{4.11}$$

$$= \pi R^2 \int_0^L \cos(k_m z) \cos(k_n z)\, dz = \begin{cases} \dfrac{\pi R^2 L}{2} \text{ for } (m = n) \\ 0 \text{ for } (m \neq n) \end{cases} \tag{4.12}$$

$$\int_V \nabla\psi_m \cdot \nabla\psi_n dV = \pi R^2 \int_0^L \nabla\psi_m \cdot \nabla\psi_n dz \tag{4.13}$$

$$= \pi R^2 \int_0^L k_m k_n \sin(k_m z) \sin(k_n z)\, dV = \begin{cases} k_m^2 \dfrac{\pi R^2 L}{2} \text{ for } (m = n) \\ 0 \text{ for } (m \neq n) \end{cases} \tag{4.14}$$

Therefore only the product of equal modes when $m = n$ contributes to the final result, all other terms for $m \neq n$ can be disregarded.

4.2.2 Time Averaging

As mentioned earlier time averaging is performed in order to eliminate the fast oscillatory time scale from the slow scale of the amplitude growth. The definition of a time average is:

$$\langle f(t) \rangle = \frac{1}{\tau} \int_0^\tau f(t)dt \tag{4.15}$$

Here τ stands for one period of the (first mode) oscillation, thus

$$\tau = \frac{2\pi}{\omega_1} \tag{4.16}$$

with

$$\omega_m = \frac{m\pi a_0}{L} \tag{4.17}$$

Carrying out the time wise integration yields:

$$\frac{1}{\tau} \int_0^\tau \sin(\omega_m t)dt = 0 \tag{4.18}$$

$$\frac{1}{\tau} \int_0^\tau \cos(\omega_m t)dt = 0 \tag{4.19}$$

$$\frac{1}{\tau} \int_0^\tau \sin(\omega_m t)\cos(\omega_n t)dt = 0 \tag{4.20}$$

$$\frac{1}{\tau} \int_0^\tau \sin^2(\omega_m t)dt = \frac{1}{2} \tag{4.21}$$

$$\frac{1}{\tau} \int_0^\tau \cos^2(\omega_m t)dt = \frac{1}{2} \tag{4.22}$$

Chapter 5

Stability Analysis of Vortex Driven Flow Instability

In this chapter all the methods and tools described above are pulled together and applied to a flow field that exhibits vortex driven flow instability. While there are different types of vortex driven instabilities as elucidated in section 1.1, the focus here will be on the direct interaction of unsteady vorticity created in an unstable shear layer with the acoustics inside a rocket chamber. The shear layer is created by the presence of an annular obstacle in the flow, which resembles an inhibitor in a solid rocket motor.

Several assumptions and simplifications have to be made in order to find a closed form solution to a complex flow field like this. On the mathematical side perturbation techniques will be used extensively to simplify the governing equations. An important small parameter involved in the problem is the mean flow Mach number M_0. Higher orders of M_0 will be dropped in the calculations for the sake of simplicity.

5.1 General Assumptions for the Flow Field

According to Lin the instability mechanism of free boundary layers can be considered an inviscid process [51]. It is caused by induction effects, and viscosity only has a damping influence. Experimental investigations by Michalke [52] show that for large Reynolds numbers the instability properties of shear layers are not noticeably affected by viscosity.

Furthermore it is assumed that the instability mechanism is a pure flow phenomenon and decoupled from the actual combustion process. Unsteady heat release is therefore ignored, which also implies that there are no entropy waves in the flow and no fluctuations in the temperature.

These assumptions greatly simplify the energy balance, since all viscous components and terms including unsteady entropy s_1 and temperature fluctuations T_1 can be dropped. Then the equations 3.48, 3.49 and 3.50 reduce to:

$$E_2 = \frac{{p_1}^2}{2\rho_0{a_0}^2} + \rho_1\mathbf{u}_0 \cdot \mathbf{u}_1 + \frac{1}{2}\rho_0{\mathbf{u_1}}^2 \tag{5.1}$$

$$W_2 = \mathbf{u}_1 p_1 + \frac{1}{\gamma p_0}\mathbf{u}_0 p_1^2 \tag{5.2}$$

$$D_2 = -\rho_0\mathbf{u}_0 \cdot (\mathbf{u}_1 \times \boldsymbol{\omega}_1) - \rho_1\mathbf{u}_1 \cdot (\mathbf{u}_0 \times \boldsymbol{\omega}_0) \tag{5.3}$$

Note that there is only a single term left that contains unsteady vorticity $\boldsymbol{\omega}_1$. The $\rho_0\mathbf{u}_0 \cdot (\mathbf{u}_1 \times \boldsymbol{\omega}_1)$-term must therefore represent the energy source that links the vortex shedding to the acoustics!

Having this in mind the total change of energy in the system <u>due to vortex shedding</u> can be isolated:

$$\frac{\partial}{\partial t}\iiint\limits_V E_2 dV = \iiint\limits_V -\rho_0\mathbf{u}_0 \cdot (\mathbf{u}_1 \times \boldsymbol{\omega}_1) dV \tag{5.4}$$

Solving this equation yields the (linear) growth rate α_{VS} for vortex driven flow instability.

5.2 Assumptions for the Near Field

The stability analysis strongly depends on the correct modeling of the complex flow field downstream from the separation point of the shear layer. The model for the near field used here is based on computational investigations of this region by Dr. Jonathan French and personal communication with Dr. Gary Flandro [53].

For later use it is convenient to shift the coordinate system into the point of separation of the shear layer. The axial position of the point of separation is denoted with Z_0, the radial position with R_0. The chamber radius is denoted with R (see figure 5.1). The new coordinates x and ξ are introduced:

$$x = z - Z_0 \tag{5.5}$$

$$\xi = \frac{y}{\theta} \tag{5.6}$$

French's computations reveal two important features of the flow: Firstly, the interaction between the shear layer and the acoustics happens within a short distance from the flow separation. This so called "hot zone" d spans typically 20 times the shear layer thickness θ. Further downstream coherent vortex structures have decayed due to turbulence and non-linear effects.

Secondly, the acoustic streamlines are deformed by the presence of an obstacle in the flow. The assumption that the unsteady acoustic velocity $\hat{\mathbf{u}}_1$ and the unsteady rotational velocity $\tilde{\mathbf{u}}_1$ are parallel can therefore not be maintained. An angle i between the two components has to be introduced.

Determining a precise function for the angle $i[\mathbf{r}]$ with axial and radial dependence is difficult, but the following thought process leads to a simple model, which will be used here:

Later calculations show that the growth rate α_{VS} is a function of $\sin^2(i)$. This dependence holds the mechanism that ends the driving of oscillations as the end of the hot zone is reached. Therefore we know:

$$\lim_{x \to d} i[\mathbf{r}] = 0 \tag{5.7}$$

The angle $i[\mathbf{r}]$ also causes the growth rate α_{VS} to decrease as the point of separation moves closer to the wall of the chamber. In the limit, when the point of separation is at the wall - that is there is no obstacle protruding into the flow - α_{VS} has to vanish. Therefore:

$$\lim_{R_0 \to R} i[\mathbf{r}] = 0 \tag{5.8}$$

In the theoretical case that the point of separation is at the chamber axis - that is an obstacle is blocking the flow completely - the deformation of the streamlines has to reach a maximum. Therefore, the angle $i[\mathbf{r}]$ has to have its largest physically plausible value of 90 degrees.

$$\lim_{R_0 \to 0} i[\mathbf{r}] = \frac{\pi}{2} \tag{5.9}$$

As a first approximation linear behavior of $i[\mathbf{r}]$ is assumed using equations 5.7, 5.8 and 5.9 as boundary conditions:

$$i[\mathbf{r}] = \frac{\pi}{2}\left(1 - \frac{x}{d}\right)\left(1 - \frac{R_0}{R}\right) \tag{5.10}$$

A model for the mean flow in the sheared region is readily available. Michalke shows that the classical hyperbolic tangent profile matches experimental data [52]. W_0 represents the velocity at the center line.

$$U_0[y] = W_0 \frac{1}{2}\left(1 + \tanh\left[\frac{y}{\theta}\right]\right) \tag{5.11}$$

The steady vorticity Ω_0 is then defined as:

$$\Omega_0 = \nabla \times U_0 = \tag{5.12}$$

$$\frac{\partial U_0}{\partial y} = \frac{W_0}{2\theta}\mathrm{sech}^2\left[\frac{y}{\theta}\right] \tag{5.13}$$

Figure 5.1 displays all the considerations above.

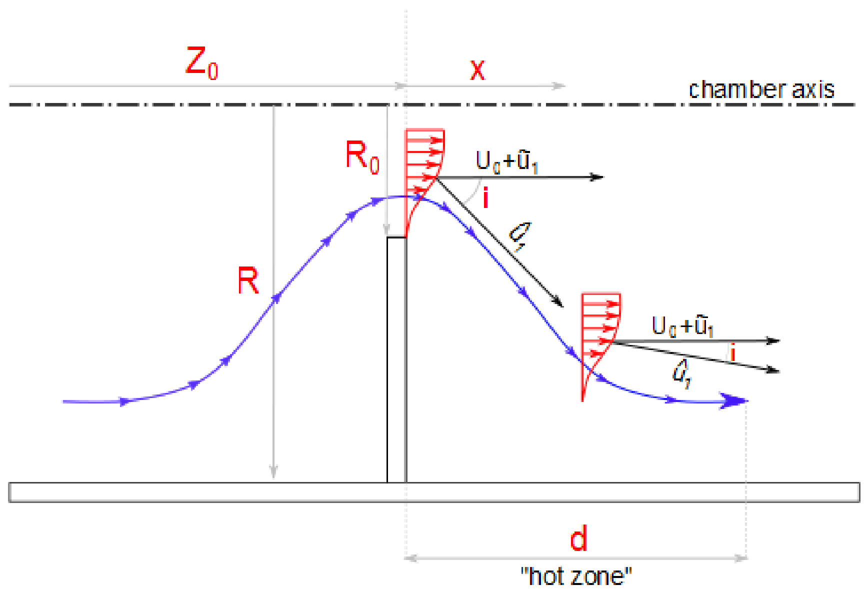

Figure 5.1: Flow Field Downstream of an Obstacle

5.3 Unsteady Acoustic Velocity $\hat{\mathbf{u}}_1$

In order to solve equation 5.4 the acoustic field has to be known. The irrotational acoustic velocity $\hat{\mathbf{u}}_1$ can be linked to the pressure using linear acoustics as demonstrated by Jacob [42]. First recalling Galerkins formulation of the pressure waves [50]:

$$p_1(\mathbf{r}, t) = P_0(t) \sum_{m=1}^{\infty} \eta_m(t) \psi_m(\mathbf{r})$$

From the linearized momentum equation,

$$\rho_0 \frac{\partial \hat{\mathbf{u}}_1}{\partial t} + \nabla p_1 = 0. \tag{5.14}$$

Inserting the pressure summation,

$$\rho_0 \frac{\partial \hat{\mathbf{u}}_1}{\partial t} + \nabla \left[P_0(t) \sum_{m=1}^{\infty} \eta_m(t) \psi_m(\mathbf{r}) \right] = 0. \tag{5.15}$$

Pulling the gradient inside the summation,

$$\frac{\partial \hat{\mathbf{u}}_1}{\partial t} = -\frac{P_0(t)}{\rho_0} \sum_{m=1}^{\infty} \eta_m(t) \nabla \psi_m(\mathbf{r}). \tag{5.16}$$

Remembering that,

$$\frac{P_0}{\rho_0} = \frac{\gamma R T_0}{\gamma} = \frac{{a_0}^2}{\gamma} \tag{5.17}$$

$$\frac{\partial \hat{\mathbf{u}}_1}{\partial t} = -\frac{{a_0}^2}{\gamma} \sum_{m=1}^{\infty} \eta_m(t) \nabla \psi_m(\mathbf{r}) = -\sum_{m=1}^{\infty} \frac{{a_0}^2 \eta_m(t)}{\gamma} \nabla \psi_m(\mathbf{r}) \tag{5.18}$$

Then using equation 4.4

$$\frac{\partial \hat{\mathbf{u}}_1}{\partial t} = -\sum_{m=1}^{\infty} \frac{{w_m}^2 \eta_m(t)}{\gamma {k_m}^2} \nabla \psi_m(\mathbf{r}) \tag{5.19}$$

Since R_m is a slow function in time:

$$\dot{\eta}_m(t) = R_m(t)\, w_m \sin(w_m t) \tag{5.20}$$

$$\ddot{\eta}_m(t) = -R_m(t)\, {w_m}^2 \cos(w_m t) = -{w_m}^2 \eta_m(t) \tag{5.21}$$

$$\frac{\partial \hat{\mathbf{u}}_1}{\partial t} = \sum_{m=1}^{\infty} \frac{\ddot{\eta}_m(t)}{\gamma {k_m}^2} \nabla \psi_m(\mathbf{r}) \tag{5.22}$$

$$\frac{\partial \hat{\mathbf{u}}_1}{\partial t} = \sum_{m=1}^{\infty} \frac{\ddot{\eta}_m(t)}{\gamma {k_m}^2} \nabla \psi_m(\mathbf{r}) = \frac{\partial}{\partial t}\left[\sum_{m=1}^{\infty} \frac{\dot{\eta}_m(t)}{\gamma {k_m}^2} \nabla \psi_m(\mathbf{r})\right] \tag{5.23}$$

Finally solving for the irrotational velocity $\hat{\mathbf{u}}_1$:

$$\hat{\mathbf{u}}_1(\mathbf{r}, t) = \sum_{m=1}^{\infty} \frac{\dot{\eta}_m(t)}{\gamma {k_m}^2} \nabla \psi_m(\mathbf{r}) \tag{5.24}$$

Now the acoustic field can be written as

$$p_1(\mathbf{r}, t) = p_0 R_m \cos(\omega_m t) \cos(k_m z) \tag{5.25}$$

$$\hat{\mathbf{u}}_1(\mathbf{r}, t) = \frac{a_0 R_m}{\gamma} \sin(\omega_m t) \sin(k_m z) \tag{5.26}$$

More detail on the acoustics can be found in appendix A.2.

Deviating from Jacob [42] the deformation of the streamlines in the near field has to be taken into account. The components of $\hat{\mathbf{u}}_1$ are rotated by the angle i, which yields to:

$$\hat{\mathbf{u}}_1(\mathbf{r}, t) = \begin{pmatrix} \hat{u}_1 \\ \hat{v}_1 \end{pmatrix} \tag{5.27}$$

$$\hat{u}_1 = -i \frac{a_0 R_m}{\gamma} \cos[i[x]] \exp[i\omega_m t] \sin[k_m (Z_0 + x)] \tag{5.28}$$

$$\hat{v}_1 = i \frac{a_0 R_m}{\gamma} \sin[i[x]] \exp[i\omega_m t] \sin[k_m (Z_0 + x)] \tag{5.29}$$

5.4 Unsteady Rotational Velocity $\tilde{\mathbf{u}}_1$ and Vorticity ω_1

The rotational field is of special importance for the vortex driven flow instability problem. In order to capture the properties of the rotational field, a stream function Ψ is introduced, and a solution based on the assumptions for the near field (see section 5.2) is derived:
The unsteady rotational velocity $\tilde{\mathbf{u}}_1$ can be expressed as the curl of a stream function Ψ.

$$\tilde{\mathbf{u}}_1(\mathbf{r}, t) = \begin{pmatrix} \tilde{u}_1 \\ \tilde{v}_1 \end{pmatrix} = \nabla \times \Psi \tag{5.30}$$

$$\begin{aligned} \tilde{u}_1 &= \frac{\partial \Psi}{\partial y} \\ \tilde{v}_1 &= -\frac{\partial \Psi}{\partial x} \end{aligned} \tag{5.31}$$

The unsteady vorticity $\boldsymbol{\omega}_1$ is defined as

$$\boldsymbol{\omega}_1 = \nabla \times \tilde{\mathbf{u}}_1 = \nabla \times \nabla \times \Psi \tag{5.32}$$

$$= -\frac{\partial^2 \Psi}{\partial x^2} - \frac{\partial^2 \Psi}{\partial y^2} \tag{5.33}$$

$$= \omega[y] \exp[i\omega_m t] \exp[ik_m (Z_0 + x)] \tag{5.34}$$

Note that the amplitude $\omega[y]$ is a complex variable and that sinusoidial mode shapes for the spatial and time-wise fluctuations of the vorticity have been assumed.

$$\omega[y] = \omega_r[y] + i\omega_i[y] \tag{5.35}$$

$$\exp[ik_m (Z_0 + x)] = \cos[k_m (Z_0 + x)] + i \sin[k_m (Z_0 + x)] \tag{5.36}$$

The stream function Ψ has yet to be determined. Conveniently let it be of the form:

$$\Psi = \phi[y] \exp[i\omega_m t] \exp[ik_m (Z_0 + x)] \tag{5.37}$$

$$\phi[y] = \phi_r[y] + i\phi_i[y] \tag{5.38}$$

Inserting this into equation 5.33 yields to:

$$\omega_1 = \left(k_m^2\phi - \phi''\right)\exp[i\omega_m t]\exp[ik_m\left(Z_0 + x\right)] \tag{5.39}$$

Comparing to equation 5.34 gives:

$$\omega[y] = \left(k_m^2\phi - \phi''\right) \tag{5.40}$$

This proves that both $\tilde{\mathbf{u}}_1$ and ω_1 only depend on a single unknown variable, the amplitude $\phi[y]$ of the stream function. If a solution for $\phi[y]$ can be found, then the rotational field is fully determined. In order to do so, an additional equation besides the conservation of mass, momentum and energy, which have already been used, is needed.
Taking the curl of the conservation of momentum yields to a new relation for the vorticity:

$$\frac{D\boldsymbol{\omega}}{Dt} = \frac{\partial\boldsymbol{\omega}}{\partial t} + \left(\mathbf{u}\cdot\nabla\right)\boldsymbol{\omega} = \boldsymbol{\omega}\cdot\nabla\mathbf{u} - \boldsymbol{\omega}\left(\nabla\cdot\mathbf{u}\right) + \frac{1}{\rho^2}\nabla\rho\times\nabla p + \nu\nabla^2\boldsymbol{\omega} + \nabla\times\mathbf{B} \tag{5.41}$$

Dropping the viscous term and body forces and assuming barotropic flow ($\nabla\rho\times\nabla p = 0$), since temperature and density iso-surfaces hardly intersect for rocket gas flow in general and for this particular case temperature fluctuations have already been eliminated.

$$\frac{\partial\boldsymbol{\omega}}{\partial t} + \left(\mathbf{u}\cdot\nabla\right)\boldsymbol{\omega} = \boldsymbol{\omega}\cdot\nabla\mathbf{u} - \boldsymbol{\omega}\left(\nabla\cdot\mathbf{u}\right) \tag{5.42}$$

Expanding of the vector quantities leads to a scalar expression for the vorticity amplitude:

$$\frac{\partial\Omega}{\partial t} + u\frac{\partial\Omega}{\partial x} + v\frac{\partial\Omega}{\partial y} + \Omega\left(\frac{\partial\hat{u}}{\partial x} + \frac{\partial\hat{v}}{\partial y}\right) = 0 \tag{5.43}$$

As before the steady and unsteady as well as the rotational and acoustic components have to be separated.

$$\begin{aligned}\Omega &= \Omega_0 + \varepsilon\omega_1 + ... \\ u &= U_0 + \varepsilon\left(\hat{u}_1 + \tilde{u}_1\right) + ... \\ v &= \varepsilon\left(\hat{v}_1 + \tilde{v}_1\right) + ...\end{aligned} \tag{5.44}$$

Inserting, collecting first order terms and rearranging gives the equation for the unsteady vorticity amplitude:

$$\frac{\partial\omega_1}{\partial t} + U_0\frac{\partial\omega_1}{\partial x} + \tilde{v}_1\frac{\partial\Omega_0}{\partial y} = -\left(\hat{v}_1\frac{\partial\Omega_0}{\partial y} + \Omega_0\frac{\partial\hat{u}_1}{\partial x} + \Omega_0\frac{\partial\hat{v}_1}{\partial y}\right) \tag{5.45}$$

All terms in equation 5.45 can now be expressed in terms of the stream function Ψ and the mean flow U_0.

$$\frac{\partial\omega_1}{\partial t} = i\omega_m\left(k_m^2\phi - \phi''\right)\exp[i\omega_m t]\exp[ik_m\left(Z_0 + x\right)] \tag{5.46}$$

$$U_0\frac{\partial\omega_1}{\partial x} = U_0\left[ik_m\left(k_m^2\phi - \phi''\right)\right]\exp[i\omega_m t]\exp[ik_m\left(Z_0 + x\right)] \tag{5.47}$$

$$\tilde{v}_1\frac{\partial\Omega_0}{\partial y} = {U_0}''\left[-ik_m\phi\right]\exp[i\omega_m t]\exp[ik_m\left(Z_0 + x\right)] \tag{5.48}$$

$$\hat{v}_1\frac{\partial\Omega_0}{\partial y} = {U_0}''\frac{a_0 R_m}{\gamma}\sin\left[i[x]\right]\exp[i\omega_m t]\sin[k_m\left(Z_0 + x\right)] \tag{5.49}$$

$$\Omega_0\frac{\partial\hat{u}_1}{\partial x} = -{U_0}'\frac{a_0 R_m}{\gamma}k_m\cos\left[i[x]\right]\exp[i\omega_m t]\cos[k_m\left(Z_0 + x\right)] \tag{5.50}$$

$$\Omega_0\frac{\partial\hat{v}_1}{\partial y} \approx 0 \tag{5.51}$$

Plugging equations 5.46 through 5.51 back into equation 5.45 and simplifying:

$$\left\{\phi'' + \left[\frac{k_m {U_0}''}{\omega_m + U_0 k_m} - k_m^2\right]\phi\right\}\exp[ik_m\left(Z_0 + x\right)] = \frac{a_0 R_m}{\gamma\left(\omega_m + U_0 k_m\right)}\begin{pmatrix}{U_0}''\sin\left[i[x]\right]\sin[k_m\left(Z_0 + x\right)] \\ -{U_0}'k_m\cos\left[i[x]\right]\cos[k_m\left(Z_0 + x\right)]\end{pmatrix} \tag{5.52}$$

The acoustic velocity $\hat{v}_1$ was regraded as constant with respect to y. The time dependence of the stream function amplitude $\phi[y]$ disappeared as expected. Separating the real and imaginary part of the right hand side of equation 5.52 and working with the real part:

$$\begin{aligned}\mathrm{Re}\left\{\phi'' + \left[\frac{k_m U_0''}{\omega_m + U_0 k_m} - k_m^2\right]\phi\right\}\exp[ik_m(Z_0+x)] = \\ -\left\{\phi''_i + \left[\frac{k_m U_0''}{\omega_m + U_0 k_m} - k_m^2\right]\phi_i\right\}\sin[k_m(Z_0+x)] \\ +\left\{\phi''_r + \left[\frac{k_m U_0''}{\omega_m + U_0 k_m} - k_m^2\right]\phi_r\right\}\cos[k_m(Z_0+x)]\end{aligned} \tag{5.53}$$

Both ϕ_r and ϕ_i have to have non-trivial solutions that vanish as $y \to \pm\infty$. Considering this yields to:

$$\phi''_i + \left[\frac{k_m U_0''}{\omega_m + U_0 k_m} - k_m^2\right]\phi_i = -\left(\frac{R_m a_0 \sin[i[x]]}{\gamma k_m}\right)\left(\frac{k_m U_0''}{\omega_m + U_0 k_m}\right) \tag{5.54}$$

$$\phi''_r + \left[\frac{k_m U_0''}{\omega_m + U_0 k_m} - k_m^2\right]\phi_r = -\left(\frac{R_m a_0 \cos[i[x]]}{\gamma}\right)\left(\frac{k_m U_0'}{\omega_m + U_0 k_m}\right) \tag{5.55}$$

The Equations 5.54 and 5.55 can be simplified by dropping terms that are small compared to the others. The mean flow Mach number M_0 is of the order 0.1, therefore only a small error is introduced when neglecting terms that multiply M_0 while keeping terms of the order 1. Defining:

$$\begin{aligned}f_1[y] = \left(\frac{k_m U_0''}{\omega_m + U_0 k_m}\right) = \frac{U_0''}{a_0 + U_0} = \\ -\frac{W_0}{\theta^2}\left[\frac{\mathrm{sech}^2\left[\frac{y}{\theta}\right]\tanh\left[\frac{y}{\theta}\right]}{a_0 + \frac{W_0}{2}\left(1+\tanh\left[\frac{y}{\theta}\right]\right)}\right] = -\frac{M_0}{\theta^2}\left[\frac{\mathrm{sech}^2\left[\frac{y}{\theta}\right]\tanh\left[\frac{y}{\theta}\right]}{1 + \frac{M_0}{2}\left(1+\tanh\left[\frac{y}{\theta}\right]\right)}\right] \\ \approx -\frac{M_0}{\theta^2}\mathrm{sech}^2\left[\frac{y}{\theta}\right]\tanh\left[\frac{y}{\theta}\right] + O[{M_0}^2]\end{aligned} \tag{5.56}$$

$$f_2[y] = \left(\frac{k_m {U_0}'}{\omega_m + U_0 k_m}\right) = \frac{{U_0}'}{a_0 + U_0} =$$
$$\frac{W_0}{2\theta}\left[\frac{\operatorname{sech}^2\left[\frac{y}{\theta}\right]}{a_0 + \frac{W_0}{2}\left(1 + \tanh\left[\frac{y}{\theta}\right]\right)}\right] = \frac{M_0}{2\theta}\left[\frac{\operatorname{sech}^2\left[\frac{y}{\theta}\right]}{1 + \frac{M_0}{2}\left(1 + \tanh\left[\frac{y}{\theta}\right]\right)}\right]$$
$$\approx \frac{M_0}{2\theta}\operatorname{sech}^2\left[\frac{y}{\theta}\right] + O[{M_0}^2] \quad (5.57)$$

The functions $f_1[y]$ and $f_2[y]$ are of the order M_0, while the wave number k_m is of the order unity. Concluding this, we know that:

$$f_1[y], f_2[y] \ll k_m \quad (5.58)$$

Hence the equations 5.54 and 5.55 reduce to:

$$\phi''_i - k_m^2\phi_i \approx \left(\frac{R_m a_0 \sin[i[x]]}{\gamma k_m}\right)\frac{M_0}{\theta^2}\operatorname{sech}^2\left[\frac{y}{\theta}\right]\tanh\left[\frac{y}{\theta}\right] \quad (5.59)$$
$$\phi''_r - k_m^2\phi_r \approx -\left(\frac{R_m a_0 \cos[i[x]]}{\gamma}\right)\frac{M_0}{2\theta}\operatorname{sech}^2\left[\frac{y}{\theta}\right] \quad (5.60)$$

5.4.1 Solution to the Unsteady Vorticity ω_1

When recalling equation 5.40 it becomes apparent that a solution for the unsteady vorticity amplitude $\omega[y]$ can be carried out without knowing an explicit solution for the stream function amplitude ϕ.

$$\omega[y] = \left(k_m^2\phi - \phi''\right)$$

Split real and imaginary part:

$$\omega_r[y] = \left(k_m^2\phi_r - \phi''_r\right) \quad (5.61)$$

$$\omega_i[y] = \left(k_m^2\phi_i - \phi''_i\right) \quad (5.62)$$

Simply comparing the equations 5.61 and 5.62 to the equations 5.59 and 5.60 yields the desired solution:

$$\omega_r = \left(\frac{R_m a_0 \cos[i[x]]}{\gamma}\right)\frac{M_0}{2\theta}\mathrm{sech}^2\left[\frac{y}{\theta}\right] + O[M_0] \tag{5.63}$$

$$\omega_i = -\left(\frac{R_m a_0 \sin[i[x]]}{\gamma k_m}\right)\frac{M_0}{\theta^2}\mathrm{sech}^2\left[\frac{y}{\theta}\right]\tanh\left[\frac{y}{\theta}\right] + O[M_0] \tag{5.64}$$

Note that terms of the order of M_0 have been dropped for the sake of simplicity!

Now all the components for the unsteady vorticity ω_1 have been determined. Putting everything together and only keeping the real part finally gives:

$$\begin{aligned}
\omega_1 &= \omega[y]\exp[ik_m(Z_0+x)]\exp[i\omega_m t] \\
&= \{\omega_r\cos[k_m(Z_0+x)] - \omega_i\sin[k_m(Z_0+x)\}\exp[i\omega_m t] \\
&= \left\{\begin{array}{l} \left(\frac{R_m a_0 \cos[i[x]]}{\gamma}\right)\frac{M_0}{2\theta}\mathrm{sech}^2\left[\frac{y}{\theta}\right]\cos[k_m(Z_0+x)] \\ +\left(\frac{R_m a_0 \sin[i[x]]}{\gamma k_m}\right)\frac{M_0}{\theta^2}\mathrm{sech}^2\left[\frac{y}{\theta}\right]\tanh\left[\frac{y}{\theta}\right]\sin[k_m(Z_0+x)] \end{array}\right\}\exp[i\omega_m t]
\end{aligned} \tag{5.65}$$

5.4.2 Solution to the Unsteady Rotational Velocity $\tilde{\mathbf{u}}_1$

There is no easy way out when calculating the unsteady rotational velocity $\tilde{\mathbf{u}}_1$. The stream function amplitude ϕ has to be computed explicitly. The velocity components $\tilde{u}_1$ and $\tilde{v}_1$ arise from differentiation of the stream function Ψ with respect to x and y. The solutions for ϕ and $\tilde{\mathbf{u}}_1$ feature complicated hypergeometric functions. Some detail is shown in appendix A.4.

However, a statement about the order of magnitude of $\tilde{\mathbf{u}}_1$ can be made without determining an explicit solution. Recall equations 5.59 and 5.60:

$$\phi''_i - k_m^2\phi_i \approx \left(\frac{R_m a_0 \sin[i[x]]}{\gamma k_m}\right)\frac{M_0}{\theta^2}\mathrm{sech}^2\left[\frac{y}{\theta}\right]\tanh\left[\frac{y}{\theta}\right]$$

$$\phi''_r - k_m^2\phi_r \approx -\left(\frac{R_m a_0 \cos[i[x]]}{\gamma}\right)\frac{M_0}{2\theta}\mathrm{sech}^2\left[\frac{y}{\theta}\right]$$

Mind that the right hand sides both multiply the mean flow Mach number M_0, which is carried through to the solutions of ϕ and $\tilde{\mathbf{u}}_1$. The solutions are of the form:

$$\phi_i = -M_0 \frac{R_m a_0 \sin[i[x]]}{\gamma k_m} \{\star[y]\} \tag{5.66}$$

$$\phi_r = -M_0 \frac{R_m a_0 \cos[i[x]]}{\gamma} \{\star[y]\} \tag{5.67}$$

The $\star$-symbols represent hypergeometric functions dependent on y that are not shown here for clarity. Taking the derivatives with respect to x and y in order to arrive at the velocity components $\tilde{u}_1$ and $\tilde{v}_1$ does not change the order of magnitude.

Now remember the equations 5.28 and 5.29 for the acoustic velocities $\hat{u}_1$ and $\hat{v}_1$:

$$\hat{u}_1 = -i \frac{a_0 R_m}{\gamma} \cos[i[x]] \exp[i\omega_m t] \sin[k_m (Z_0 + x)]$$

$$\hat{v}_1 = i \frac{a_0 R_m}{\gamma} \sin[i[x]] \exp[i\omega_m t] \sin[k_m (Z_0 + x)]$$

When comparing the order of magnitude of $\hat{\mathbf{u}}_1$ and $\tilde{\mathbf{u}}_1$, it becomes apparent that the rotational velocity components are much smaller than the acoustic velocity components, therefore:

$$\hat{u}_1 \gg \tilde{u}_1 \tag{5.68}$$

$$\hat{v}_1 \gg \tilde{v}_1 \tag{5.69}$$

$$\mathbf{u}_1 = \hat{\mathbf{u}}_1 + \tilde{\mathbf{u}}_1 \approx \hat{\mathbf{u}}_1 \tag{5.70}$$

5.5 Linear Growth Rate α_{VS}

The total change of energy due to interaction between the shear layer and the acoustics is described by equation 5.71, which is an expanded version of equation 5.4.

$$\frac{\partial}{\partial t}\iiint\limits_V \left(\underbrace{\frac{p_1^2}{2\rho_0 a_0^2}}_{A} + \underbrace{\rho_1 \mathbf{u}_0 \cdot \mathbf{u}_1}_{B} + \underbrace{\frac{1}{2}\rho_0 \left(\mathbf{u}_1 \cdot \mathbf{u}_1\right)}_{C}\right) dV = \iiint\limits_V \underbrace{-\rho_0 \mathbf{u}_0 \cdot \left(\mathbf{u}_1 \times \omega_1\right)}_{D} dV \qquad (5.71)$$

Solving this equation yields the (linear) growth rate α_{VS} for vortex driven flow instability. By now all components of equation 5.71 have been determined and the time averaging and integration over the volume can be carried out. Since this involves some more tedious algebra, it is done for each term on the right hand side and the left hand side separately. The right hand side represents the total change of energy, while the left hand side represents a source term.

5.5.1 Change of Energy

Part A

$$\frac{p_1^2}{2\rho_0 a_0^2} = \frac{P_0^2}{2\rho_0 a_0^2}\sum_{m=1}^{\infty}\sum_{n=1}^{\infty} R_m \sin\left(\omega_m t\right) R_n \sin\left(\omega_n t\right) \cos[k_m \left(Z_0 + x\right)] \cos[k_n \left(Z_0 + x\right)] \qquad (5.72)$$

From the orthogonality considerations in section 4.2.1 it is already known that addends only contribute to the result if $m = n$, therefore:

$$\frac{{p_1}^2}{2\rho_0 {a_0}^2} = \frac{P_0^2}{2\rho_0 a_0^2}\sum_{m=1}^{\infty} {R_m}^2 \sin^2\left(\omega_m t\right) \cos^2[k_m \left(Z_0 + x\right)] \qquad (5.73)$$

Now take the time average. The amplitude R_m is quasi-constant over one period of the oscillations and is therefore pulled out of the time-wise integral. Using the results from section 4.2.2:

$$\left\langle \frac{{p_1}^2}{2\rho_0 {a_0}^2} \right\rangle = \frac{P_0^2}{4\rho_0 a_0^2}\sum_{m=1}^{\infty} {R_m}^2 \cos^2[k_m \left(Z_0 + x\right)] \qquad (5.74)$$

Integrating over the volume and combining and simplifying the thermodynamic variables:

$$\int_V \left\langle \frac{{p_1}^2}{2\rho_0 {a_0}^2} \right\rangle dV = \frac{P_0^2}{4\rho_0 a_0^2}\frac{\pi R^2 L}{2}\sum_{m=1}^{\infty} {R_m}^2 = \frac{P_0}{8\gamma}\pi R^2 L \sum_{m=1}^{\infty} {R_m}^2 \tag{5.75}$$

Part B

$$\rho_1 \mathbf{u}_0 \cdot \mathbf{u}_1 = \rho_1 U_0 (\hat{u}_1 + \tilde{u_1}) \approx \rho_1 U_0 \hat{u}_1 \tag{5.76}$$

The acoustic field shows that this term vanishes in the time average. The real part of the acoustic velocity $\hat{u}$ depends on $\sin[\omega t]$, whereas the density ρ_1 on $\cos[\omega t]$. The integral over one period of the product of both functions equals zero.

$$\hat{u}_1 = -i\frac{a_0}{\gamma}\sum_{m=1}^{\infty} R_m \cos\left[i[x]\right] \exp[i\omega_m t] \sin[k_m (Z_0 + x)]$$

$$\rho_1 = \rho_0 \sum_{m=1}^{\infty} R_m \cos(\omega_m t) \cos[k_m (Z_0 + x)]$$

$$\langle \rho_1 U_0 \hat{u}_1 \rangle = 0 \tag{5.77}$$

Part C

Since the acoustic velocity $\hat{\mathbf{u}}_\mathbf{1}$ is an order of magnitude larger than the rotational velocity $\tilde{\mathbf{u}}_\mathbf{1}$, part C can be written as:

$$\frac{1}{2}\rho_0 (\mathbf{u}_1 \cdot \mathbf{u}_1) \approx \frac{1}{2}\rho_0 (\hat{\mathbf{u}}_1 \cdot \hat{\mathbf{u}}_1) \tag{5.78}$$

Physically speaking, kinetic energy carried by vorticity waves is ignored at this point. This simplification was addressed by Flandro and Majdalani [54]. They included the rotational velocity into the computations of the energy balance for a general case and found that the result for the $\frac{\partial E}{\partial t}$-term in equation 2.1 was 25% larger. Since this is within the accuracy level of all the simplifications and truncations that have been used before, the rotational part is neglected here.

The velocity component $\hat{v}_1$ arose from the deformation of the acoustic streamlines in the near field. However, when the dot product $\hat{\mathbf{u}}_\mathbf{1} \cdot \hat{\mathbf{u}}_\mathbf{1}$ is carried out the dependence on the angle $i[x]$ disappears:

$$\frac{1}{2}\rho_0 {u_1}^2 = \frac{1}{2}\rho_0 \frac{a_0^2}{\gamma^2} \sum_{m=1}^{\infty} \sum_{n=1}^{\infty} R_m \cos(\omega_m t)\, R_n \cos(\omega_n t) \sin[k_m x] \sin[k_n x] \tag{5.79}$$

$$= \frac{1}{2}\rho_0 \frac{a_0^2}{\gamma^2} \sum_{m=1}^{\infty} {R_m}^2 \cos^2(\omega_m t) \sin^2[k_m x] \tag{5.80}$$

Taking the time average and cleaning up the thermodynamic variables:

$$\left\langle \frac{1}{2}\rho_0 {u_1}^2 \right\rangle = \frac{P_0}{4\gamma} \sum_{m=1}^{\infty} {R_m}^2 \sin^2[k_m x] \tag{5.81}$$

Finally integrating over the volume:

$$\int_V \left\langle \frac{1}{2}\rho_0 {u_1}^2 \right\rangle dV = \frac{P_0}{8\gamma} \pi R^2 L \sum_{m=1}^{\infty} {R_m}^2 \tag{5.82}$$

5.5.2 Source

Expanding part D leads to the scalar expression:

$$-\rho_0 \mathbf{u}_0 \cdot (\mathbf{u}_1 \times \omega_1) = -\rho_0 \begin{pmatrix} U_0 \\ 0 \\ 0 \end{pmatrix} \cdot \left[\left\{ \begin{pmatrix} \hat{u}_1 \\ \hat{v}_1 \\ 0 \end{pmatrix} + \begin{pmatrix} \tilde{u}_1 \\ \tilde{v}_1 \\ 0 \end{pmatrix} \right\} \times \begin{pmatrix} 0 \\ 0 \\ \omega_1 \end{pmatrix} \right] \tag{5.83}$$

$$= \rho_0 U_0 \omega_1 \tilde{v}_1 - \rho_0 U_0 \omega_1 \hat{v}_1 \tag{5.84}$$

It has been shown previously that $\tilde{v}_1$ is an order of magnitude smaller than $\hat{v}_1$, therefore:

$$\rho_0 U_0 \omega_1 \tilde{v}_1 - \rho_0 U_0 \omega_1 \hat{v}_1 \approx -\rho_0 U_0 \omega_1 \hat{v}_1 \tag{5.85}$$

After all the hard work in the previous sections the individual components of equation 5.85 are already known. Inserting equations 5.11, 5.65 and 5.29:

$$
\begin{aligned}
&-\rho_0 U_0 \omega_1 \hat{v}_1 = \\
&\qquad -\rho_0 U_0 \sum_{m=1}^{\infty} \left\{ \begin{array}{l} \left(\dfrac{R_m a_0 \cos\left[i[x]\right]}{\gamma}\right)\left(\dfrac{k_m {U_0}''}{\omega_m + U_0 k_m}\right)\cos[k_m\left(Z_0 + x\right)] \\ + \left(\dfrac{R_m a_0 \sin\left[i[x]\right]}{\gamma k_m}\right)\left(\dfrac{k_m {U_0}'}{\omega_m + U_0 k_m}\right)\sin[k_m\left(Z_0 + x\right)] \end{array} \right\} \\
&\qquad\qquad i\frac{a_0 R_m}{\gamma}\sin[i[x]]\sin[k_m\left(Z_0 + x\right)]\exp[i2\omega_m t] \qquad (5.86)
\end{aligned}
$$

Several terms of equation 5.86 can be simplified and combined, which yields to a much simpler expression after also taking the time average and dropping the imaginary part:

$$
\langle -\rho_0 U_0 \omega_1 \hat{v}_1 \rangle = \frac{\rho_0 {a_0}^2}{2\gamma} \sum_{m=1}^{\infty} R_m^2 \left\{ \begin{array}{l} \left(\dfrac{\sin[2i[x]]}{4\gamma}\right)\left(\dfrac{U_0 {U_0}'}{a_0 + U_0}\right)\sin[2k_m\left(Z_0 + x\right)] \\ -\left(\dfrac{\sin^2[i[x]]}{\gamma k_m}\right)\left(\dfrac{U_0 {U_0}''}{a_0 + U_0}\right)\sin^2[k_m\left(Z_0 + x\right)] \end{array} \right\} \qquad (5.87)
$$

The next step is the integration of equation 5.87 over the volume. For a cylindrical chamber polar coordinates are used most conveniently. The azimuthal angel is represented by χ, the axial position by z and the radial position by y. The integration can be performed for the three coordinates separately.

Note that the unsteady vorticity has a non-zero value only inside the "hot-zone". The integration over the whole chamber therefore equals the integration over the "hot-zone" only.

In axial direction this yields:

$$
\int_0^L \langle -\rho_0 U_0 \omega_1 \hat{v}_1 \rangle \, dz = \int_0^d \langle -\rho_0 U_0 \omega_1 \hat{v}_1 \rangle \, dx \qquad (5.88)
$$

In radial direction this yields:

$$
\int_0^R \langle -\rho_0 U_0 \omega_1 \hat{v}_1 \rangle \, dy = \int_{-\infty}^{\infty} \langle -\rho_0 U_0 \omega_1 \hat{v}_1 \rangle \, \theta d\xi \qquad (5.89)
$$

Integration with Respect to χ

Since the flow field is axial symmetric, there is no function with azimuthal dependence in equation 5.87.

$$\int_0^{2\pi} R_0 d\chi = 2\pi R_0 \tag{5.90}$$

Integration with respect to y

Equation 5.87 contains two functions of y:

$$\left(\frac{U_0 U_0{}'}{a_0 + U_0}\right) = \frac{W_0 M_0}{4\theta}\left[\frac{(1+\tanh[\xi])\,\text{sech}^2[\xi]}{1+\frac{M_0}{2}(1+\tanh[\xi])}\right] \tag{5.91}$$

$$= \frac{W_0 M_0}{4\theta}(1+\tanh[\xi])\,\text{sech}^2[\xi] + O[M_0^2] \tag{5.92}$$

$$\left(\frac{U_0 U_0{}''}{a_0 + U_0}\right) = -\frac{W_0 M_0}{2\theta^2}\left[\frac{(1+\tanh[\xi])\,\text{sech}^2[\xi]\tanh[\xi]}{1+\frac{M_0}{2}(1+\tanh[\xi])}\right] \tag{5.93}$$

$$= -\frac{W_0 M_0}{2\theta^2}(1+\tanh[\xi])\,\text{sech}^2[\xi]\tanh[\xi] + O[M_0^2] \tag{5.94}$$

Knowing that:

$$\int_{-\infty}^{\infty} \text{sech}^2[\xi] d\xi = 2 \tag{5.95}$$

$$\int_{-\infty}^{\infty} \tanh[\xi]\text{sech}^2[\xi] d\xi = 0 \tag{5.96}$$

$$\int_{-\infty}^{\infty} \tanh^2[\xi]\text{sech}^2[\xi] d\xi = \frac{2}{3} \tag{5.97}$$

Therefore:

$$\int_{-\infty}^{\infty}\left(\frac{U_0 U_0{}'}{a_0 + U_0}\right)\theta d\xi = \frac{W_0 M_0}{4\theta}\theta\,[2+0] = \frac{W_0 M_0}{2} \tag{5.98}$$

$$\int_{-\infty}^{\infty}\left(\frac{U_0 U_0{}''}{a_0 + U_0}\right)\theta d\xi = -\frac{W_0 M_0}{2\theta^2}\theta\left[0+\frac{2}{3}\right] = -\frac{W_0 M_0}{3\theta} \tag{5.99}$$

Integration with Respect to z

Equation 5.87 contains two functions of z:

$$\frac{1}{4\gamma}\sin[2i[x]]\sin[2k_m(Z_0+x)] \tag{5.100}$$

$$-\frac{1}{\gamma k_m}\sin^2[i[x]]\sin^2[k_m(Z_0+x)] \tag{5.101}$$

Recalling equation 5.10 for the angle $i[x]$:

$$i[x]=\frac{\pi}{2}\left(1-\frac{x}{d}\right)\left(1-\frac{R_0}{R}\right)$$

Integrating the equations 5.100 and 5.101 with respect to x yields to a confusing result, which can be simplified by taking advantage of the different scales of the variables invovled. The shear layer thickness θ as well as the length of the "hot-zone" d are much smaller than the radius or the length of the chamber:

$$\theta, d \ll R, R_0, Z_0, L \tag{5.102}$$

Furthermore θ and d are also much smaller than unity, therefore:

$$\theta, d \ll 1 \tag{5.103}$$

$$\sin[2k_m d] \approx 2k_m d \tag{5.104}$$

$$\cos[2k_m d] \approx 1 \tag{5.105}$$

The details of the integration of the equations 5.100 and 5.101 and the simplification process are shown in appendix A.5.

The integration over equation 5.100 yields to:

$$\int_0^d \frac{1}{4\gamma}\sin[2i[x]]\sin[2k_m(Z_0+x)]dx =$$

$$\frac{1}{4\gamma}d\sin[2k_m Z_0]\left[\frac{1}{\pi\left(1-{}^{R_0}/_{R}\right)}\right]\left(1+\cos\left[\pi{}^{R_0}/_{R}\right]\right) \quad (5.106)$$

Integration over equation 5.101 yields to:

$$\int_0^d -\frac{1}{\gamma k_m}\sin^2[i[x]]\sin^2[k_m(Z_0+x)]dx =$$

$$-\frac{1}{\gamma k_m}\frac{1}{4}d\left(1-\cos[2k_m Z_0]\right)\left(1-\frac{\sin\left[\pi{}^{R_0}/_{R}\right]}{\pi\left(1-{}^{R_0}/_{R}\right)}\right) \quad (5.107)$$

Source Combined

Gathering and recombining all parts of the right hand side finally leads to:

$$\iiint_V \langle -\rho_0\mathbf{u}_0\cdot(\mathbf{u}_1\times\omega_1)\rangle\, dV \approx$$

$$\frac{\rho_0 {a_0}^2}{2\gamma}2\pi R_0\sum_{m=1}^{\infty}R_m^2\left[\begin{array}{l}\dfrac{W_0M_0}{2}\left\{\dfrac{1}{4\gamma}d\sin[2k_mZ_0]\left[\dfrac{1}{\pi\left(1-{}^{R_0}/_{R}\right)}\right]\left(1+\cos\left[\pi{}^{R_0}/_{R}\right]\right)\right\}\\ -\left\{-\dfrac{W_0M_0}{3\theta}\right\}\left\{\dfrac{1}{4\gamma k_m}d\left(1-\cos[2k_mZ_0]\right)\left(1-\dfrac{\sin\left[\pi{}^{R_0}/_{R}\right]}{\pi\left(1-{}^{R_0}/_{R}\right)}\right)\right\}\end{array}\right] \quad (5.108)$$

Numerous approximations had to be made up to this point in order to arrive at the comparatively simple equation 5.108. Therefore, one last simplification can be used without increasing the error of the solution. Having in mind that the shear layer thickness θ is much smaller than unity yields:

$$\frac{W_0 M_0}{2} \ll \frac{W_0 M_0}{3\theta} \tag{5.109}$$

Using this and remembering that $\frac{\rho_0 {a_0}^2}{\gamma} = P_0$ and $\frac{M_0}{k_m} = \frac{W_0}{\omega_m}$, equation 5.108 becomes:

$$\iiint\limits_V \langle -\rho_0 \mathbf{u}_0 \cdot (\mathbf{u}_1 \times \omega_1) \rangle \, dV \approx$$

$$\pi \frac{p_0}{12\gamma} \frac{R_0 {W_0}^2 d}{\theta \omega_m} \sum_{m=1}^{\infty} R_m^2 \left(1 - \cos[2k_m Z_0]\right) \left(1 - \frac{\sin\left[\pi {}^{R_0}\!/_{R}\right]}{\pi \left(1 - {}^{R_0}\!/_{R}\right)}\right) \tag{5.110}$$

5.5.3 Solving for the Growth Rate α_{VS}

All terms in equation 5.71 have been fully determined and the time averaging and integration over the volume has been carried out. Collecting the results for part A through D transforms the governing equation 5.71 into:

$$\underbrace{\frac{P_0}{8\gamma} \pi R^2 L \sum_{m=1}^{\infty} \frac{\partial}{\partial t} {R_m}^2}_{A} + \underbrace{0}_{B} + \underbrace{\frac{P_0}{8\gamma} \pi R^2 L \sum_{m=1}^{\infty} \frac{\partial}{\partial t} {R_m}^2}_{C} =$$

$$\underbrace{\pi \frac{P_0}{12\gamma} \frac{R_0 {W_0}^2 d}{\theta \omega_m} \sum_{m=1}^{\infty} {R_m}^2 \left(1 - \cos[2k_m Z_0]\right) \left(1 - \frac{\sin\left[\pi {}^{R_0}\!/_{R}\right]}{\pi \left(1 - {}^{R_0}\!/_{R}\right)}\right)}_{D} \tag{5.111}$$

Rearranging equation 5.111 and using $\frac{\partial}{\partial t} {R_m}^2 = 2R_m \frac{\partial}{\partial t} R_m$ and $\omega_m = 2\pi f_m$, where f_m is the oscillation frequency of the m-th mode:

$$\sum_{m=1}^{\infty} \frac{1}{R_m} \frac{\partial}{\partial t} R_m = \frac{1}{12} \frac{R_0 d}{\pi f_m R^2 L \theta} {W_0}^2 \sum_{m=1}^{\infty} \left(1 - \cos[2k_m Z_0]\right) \left(1 - \frac{\sin\left[\pi {}^{R_0}\!/_{R}\right]}{\pi \left(1 - {}^{R_0}\!/_{R}\right)}\right) \tag{5.112}$$

Equation 5.112 is a linear differential equation for the wave amplitude R_m. Solving for R_m yields to an expression of the form:

$$R_m[t] = R_m e^{\alpha_{VS} t} \tag{5.113}$$

The right hand side of equation 5.112 corresponds to the (linear) growth rate α_{VS}, with:

$$\alpha_{VS} = \frac{1}{12} \frac{R_0 d}{\pi f_m R^2 L \theta} {W_0}^2 \sum_{m=1}^{\infty} \left(1 - \cos[2 k_m Z_0]\right) \left(1 - \frac{\sin\left[\pi {R_0}/{R}\right]}{\pi \left(1 - {R_0}/{R}\right)} \right) \tag{5.114}$$

Figure 5.2 depicts α_{VS} in dependence of the relative axial position of the point of separation of the shear layer Z_0/L and the oscillation frequency f_m. Contour plots of α_{VS} can be seen in figure 5.3. For the plots a set of parameters was chosen that matches the conditions of the experiment in chapter 7: $L = 89'', R_0/R = 0.47, W_0 = 17m/s, a_0 = 340m/s, \theta = 10^{-4}m$. Values of α_{VS} larger than zero mean that energy from the mean flow is diverted into oscillations. Apparently it depends on the relative position of Z_0/L - that is on the relative position of an obstacle in the flow - which particular modes of the oscillations are driven. There is no value Z_0/L for which no oscillations are excited.

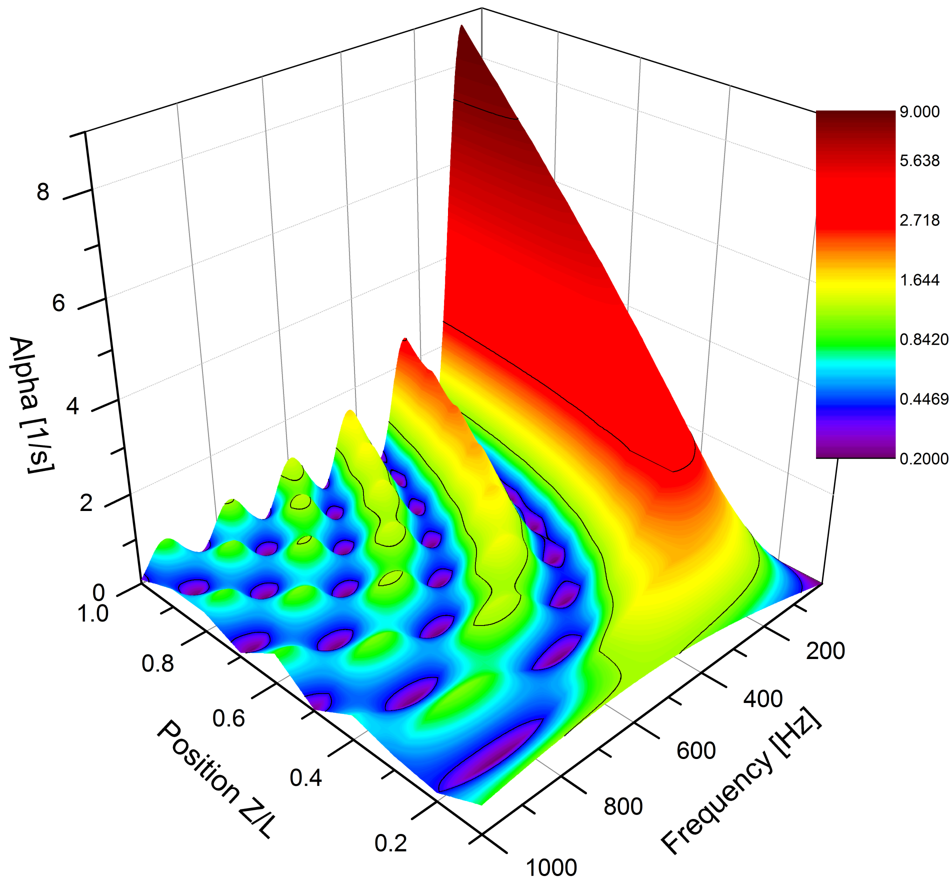

Figure 5.2: Growth Rate α_{VS} as a Function of Z_0/L and f_m

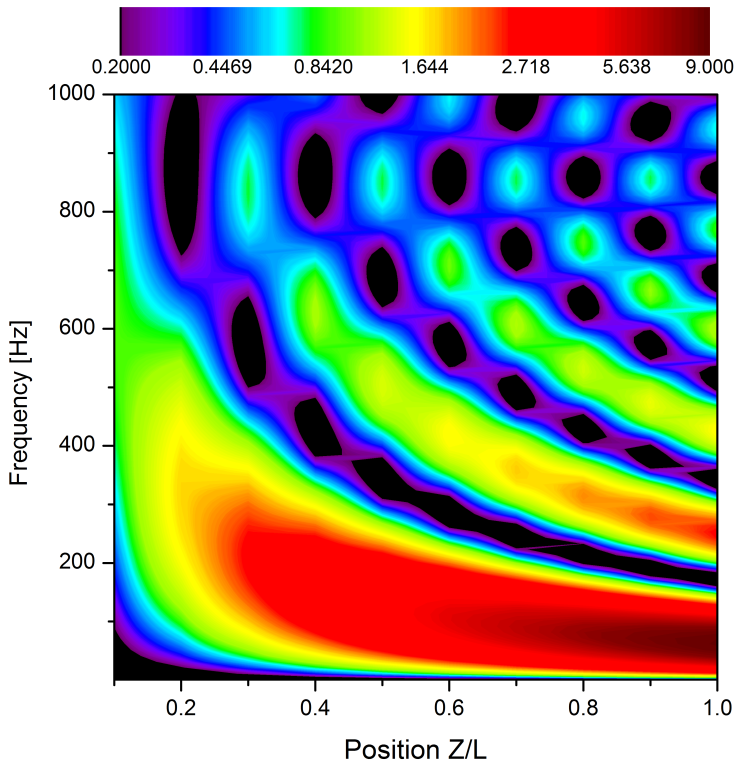

(a) Colored Contours of α_{VS}

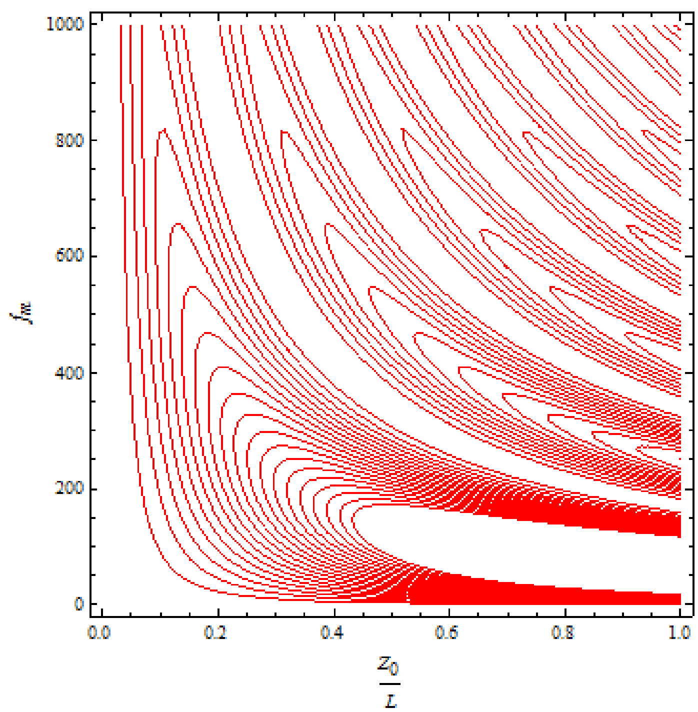

(b) Contour Lines of α_{VS}

Figure 5.3: Growth Rate α_{VS} as a Function of Z_0/L and f_m. Contour Plots.

Chapter 6

Linear vs. Non-Linear Behavior

Calculating the oscillation amplitudes R_m based on the second order expansion of the energy according to equation 3.38 always results in a linear differential equation of the form:

$$\frac{\partial R_m}{\partial t} = \alpha R_m \tag{6.1}$$

A solution to equation 6.1 is an exponential function with the exponent α.

$$R_m[t] = R_m e^{\alpha t} \tag{6.2}$$

The exponent α determines the growth of the amplitude R_m and therefore represents a growth rate. If α is positive equation 6.2 describes exponential and unbounded growth of the amplitude R_m. This behavior is unphysical and cannot be proved in experiments. In reality the formation of limit cycle amplitudes bounds the wave amplitudes to finite values [3]. This is caused by non-linear effects, which redistribute energy from each oscillation mode into its harmonics.

The redistribution phenomenon is not captured in calculations based on the second order energy. Growth rates that result from these are therefore called <u>linear</u> growth rates.

If the energy balance is expanded to the third order, the linking of each mode to its harmonics becomes evident. This procedure is laid out beautifully and in great detail by Jacob [42]

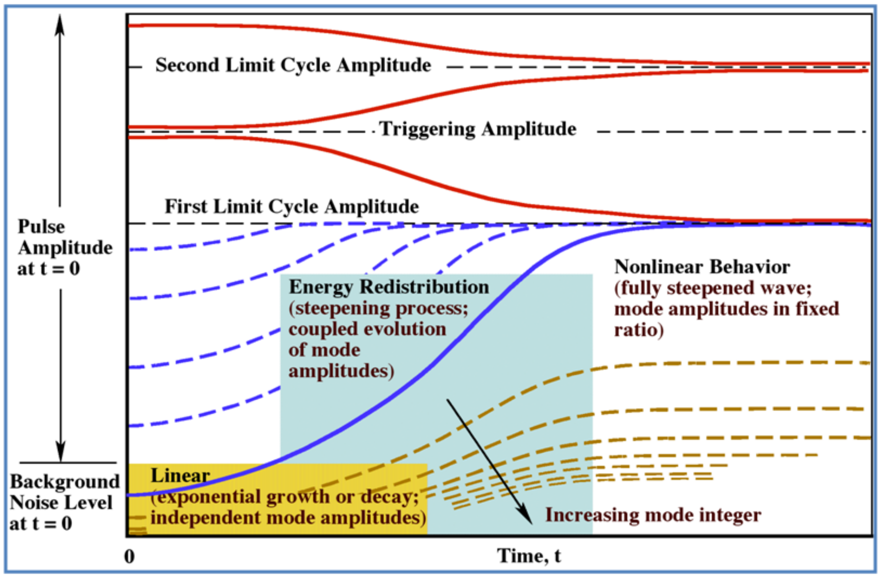

Figure 6.1: Wave Amplitude Growth over Time [3]

and yields to a non-linear correction of equation 6.1.

$$\frac{\partial}{\partial t}R_m = R_m\alpha_m - \left(\frac{2-\gamma}{8\gamma}\right)\omega_m \sum_{n=1}^{\infty}\sum_{l=1}^{\infty} R_l R_n E_{mnl} \tag{6.3}$$

$$E_{mnl} = \begin{cases} \delta(l-m-n) \\ +\delta(l+m-n) \\ -\delta(l-m+n) \end{cases}$$

Figure 6.1 displays the amplitudes of oscillatory waves and shows the non-linear coupling between the modes. Note that initially (linear) exponential growth is observed before the non-linear effects take place.

For this reason the calculation of the linear growth rates still gives valuable hints whether oscillations in a system are driven or damped, although predictions of the final amplitudes cannot be made. In fact, the widely used Standard Stability Prediction program (SSP) is based entirely on linear considerations [47].

The onset of non-linear behavior arises from deviations of the wave forms from the classical (linear) sinusoidal profile.

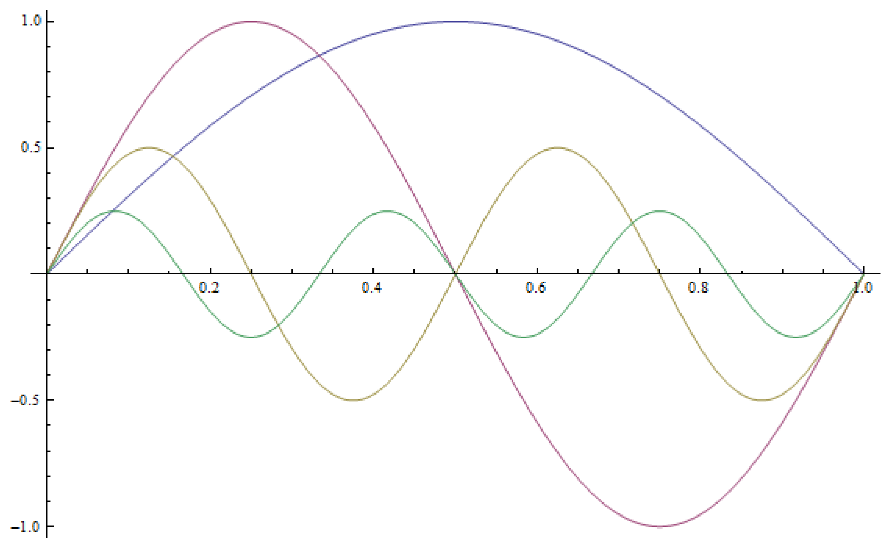

Figure 6.2: First Four Modes of Longitudinal Wave

6.1 Classic Acoustics

The classic acoustic wave equation is derived by combining the momentum and continuity equations.

$$\frac{1}{c^2}\frac{\partial^2 p}{\partial t^2} - \nabla^2 p = 0 \tag{6.4}$$

Detailed discussions on acoustics can be found in [48] or [49], an abbreviated derivation is found in Appendix A.2. The solution to equation 6.4 depends on the geometry involved as well as on the type of oscillation. Bessel functions solve the equation for radial and tangential modes, sine and cosine functions are appropriate solutions for longitudinal waves. Closed-closed end conditions, as they are found in the combustion chamber of a solid rocket motor, require velocity nodes and pressure anti-nodes at the end planes. Figure 6.2 depicts the mode shapes of the first four longitudinal modes.

6.2 Wave Steepening

The linear sinusoidal mode shapes don't persist for long in reality. As an acoustic wave travels through a medium, it locally changes the speed of sound which directly depends on

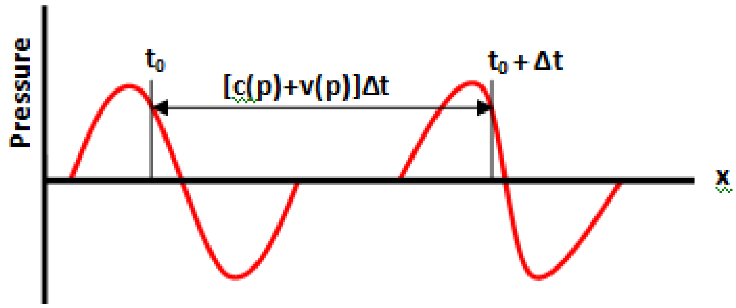

Figure 6.3: Wave Steepening [49]

the local pressure. This causes different parts of the wave to travel at different speeds, which in return causes the wave to deform and the wavefront to "steepen" - much like surface waves break on a beach. This behavior is depicted in figure 6.3. Once the wavefront of a mode is fully steepened, the energy cannot be restrained in this particular mode and cascades into its harmonics. This process limits the wave growth as the higher modes require more energy to be sustained [49]. The initial exponential growth of the oscillation amplitudes is only valid as long as this coupling mechanism between the individual modes has not set in.
Non-linear wave steepening can cause another interesting phenomenon in a closed chamber. The mean pressure increases as can be seen in figure 1.14. This so called "DC-shift" stems from work being done on the fluid by the waveform at the surface. It has to be considered in the design process of any rocket as the shift of the mean pressure can result in catastrophic failure of the pressure vessel.

Chapter 7

Experimental Verification

Any theory is otiose as long as it can't be validated experimentally. The main features of vortex driven flow instability are independent from any combustion processes. For this reason a cold flow experiment is performed in order to find experimental verification for the theory presented above.

The theory only covers the linear growth rate α_{VS}, therefore predictions of the final non-linear limit cycle amplitudes cannot be made. For this reason, only a qualitative comparison between the theory and the experimental data can be achieved. The measured oscillation amplitudes are expected to be highest for a set of parameters Z_0/L and f_m, if the theoretical growth rate peaks as well.

The experiment consists of a tube with acoustic closed-closed end conditions into which flow is injected radially at the upstream end. At the exit plane choked flow is maintained at all times. This configuration simulates the internal flow conditions of a solid rocket motor.

An annular baffle is inserted into the flow from which vortices are shed. Both the size of the baffle as well as its relative position in the flow are varied. Measurements of the pressure oscillations in the tube are taken.

Figure 7.1 depicts a schematic view of the experimental configuration.

A very similar experimental set up was used by Flatau [55] with the significant difference that there were two baffles in the flow and hole-tone acoustic responses were investigated.

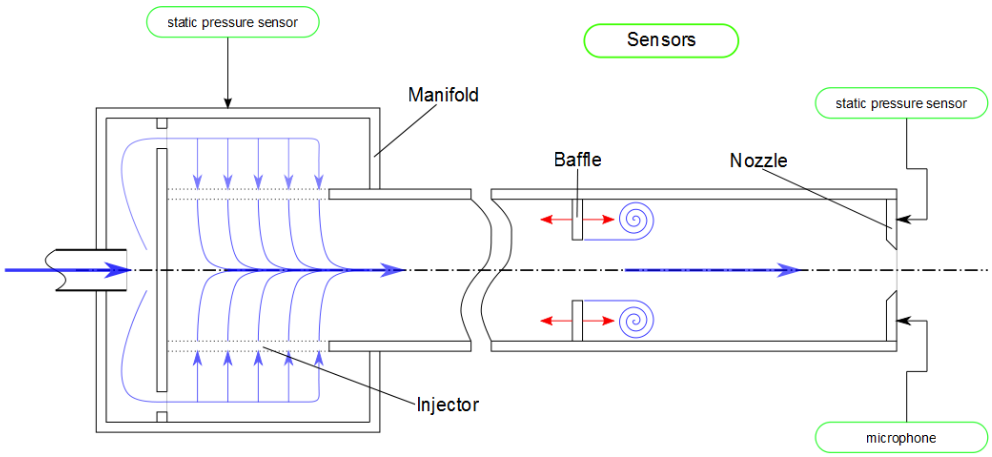

Figure 7.1: Schematic View of the Experimental Set Up.

Any kind of cavity flow like effects are ruled out in the current experiment by the presence of a single baffle only.

7.1 The Apparatus

The resonating test chamber is built from an aluminum tube with a wall thickness of 1/8 of an inch, an inner diameter of 4.25 inches and an overall length including the injector of 7 foot and 5 inches. The upstream head end is a solid aluminum plate. The downstream end consists of a disk of acrylic plastic with a thickness of 1/2 of an inch. The end plate features a nozzle with a 1.25 inch diameter and a steep converging-diverging profile. The flow is choked when the apparatus is operated on design. The profile of the nozzle creates a sharp edge on the inside, which fixes the position of the shock that forms at the exit plane. Without a defined edge the shock tends to oscillate back and forth, adding high frequency noise to the system.

The air flow through the apparatus is provided by an 2 inch pressurized air pipe, which can deliver pressures up to 3000psi.

The experimental configuration provides (approximately) closed-closed acoustic end conditions similar to a solid rocket motor and results in a natural frequency of 75 HZ for the first axial mode.

The annular baffles that are inserted into the chamber are made from 1/32 inch thick aluminum sheet. Various sizes are used with internal diameters between 3.5 and 2.0 inches. The baffles are glued to a plastic support slider ring with a wall thickness of 3/32 of an inch and a length of 1 inch. The slider ring ensures the square alignment of the baffle in the flow and provides a base, to which two 1/8 inch steel rods are mounted.

The steel rods are 6 foot long and run through two holes in the nozzle plate from the inside of the chamber to the outside. A stepper motor, which is connected to the rods over a simple gearing, is used to change the axial position of the baffle.

Figure 7.2 shows the main chamber and the nozzle end plate with a baffle in the chamber.

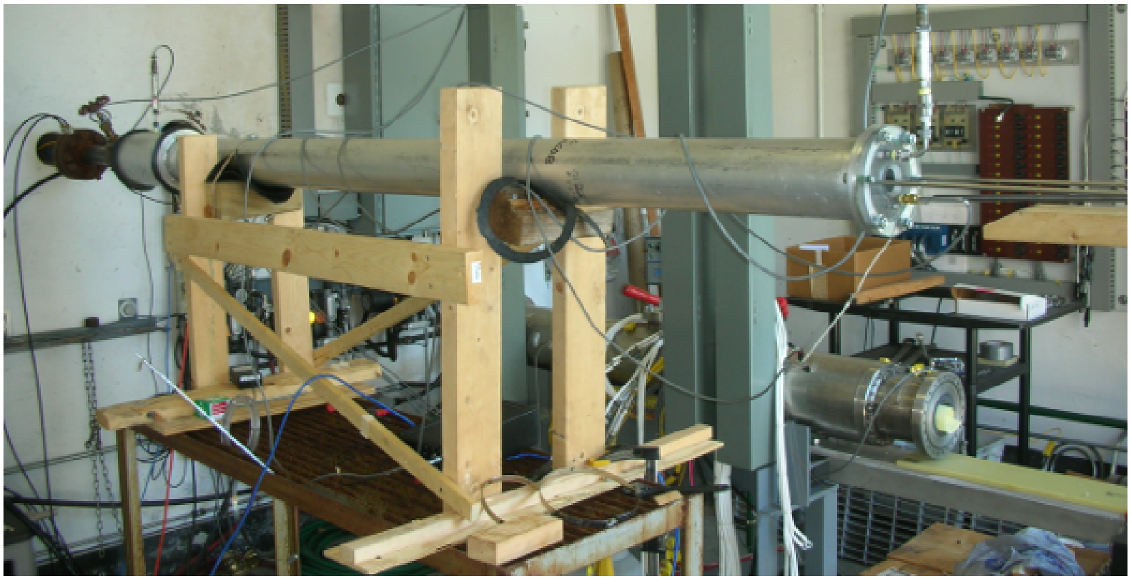

(a) Main Chamber

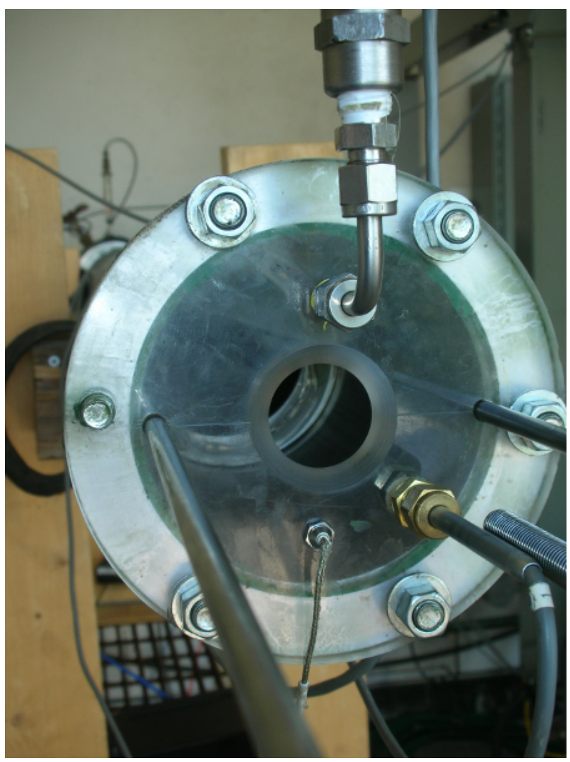

(b) Nozzle End Plate

Figure 7.2: Experimental Set Up

7.1.1 Injector

Special attention has to be paid towards the design of the injector since it has to fulfill several tasks at once.

Primarily it needs to inject the flow into the main chamber as smooth and turbulence free as possible. It also has to decouple the acoustic field inside the test chamber from any resonance with the gas column upstream from the injection point by generating a high pressure drop. At the same time the maximal pressure has to be limited to a level that does not jeopardize the structure of the apparatus. The pressure drop is also limited by the choked flow condition, as shock waves must not form at the injection. Furthermore the injector needs to provide a constant air mass flow that is large enough to maintain choked flow at the exit plane and a sufficiently high mean flow speed in the chamber.

Flatau used an injector built from sintered bronze [55]. For cost reasons this was not possible in this study. In order to emulate a porous material, a PVC tube with a large number of radial holes is used instead.

Determining an appropriate number of holes with an appropriate diameter is not straight forward. The equations that are available to quantify the pressure drop across an orifice have all been developed empirically. The following expression is widely used for a standard "sharp" orifice in a pipe:

$$Q = C_d \sqrt{\frac{2\Delta p}{\rho}} \frac{A_2}{\sqrt{1 - \left({}^{A_2}\!/_{A_1} \right)^2}} \tag{7.1}$$

Here Q stands for the volumetric flow rate, Δp for the pressure drop, ρ for the density, A_1 for the cross-sectional area of the pipe and A_2 for the cross-sectional area of the orifice hole. The factor C_d accounts for the production of entropy, and therefore for the net pressure loss, as the flow passes the orifice. Obviously it depends on whether the flow is compressible or incompressible, viscous or inviscid and the exact geometry of the orifice. For many cases the value for C_d is tabulated based on experimental data, but for the more complex geometry of a radial injector with multiple "orifices" no data exists.

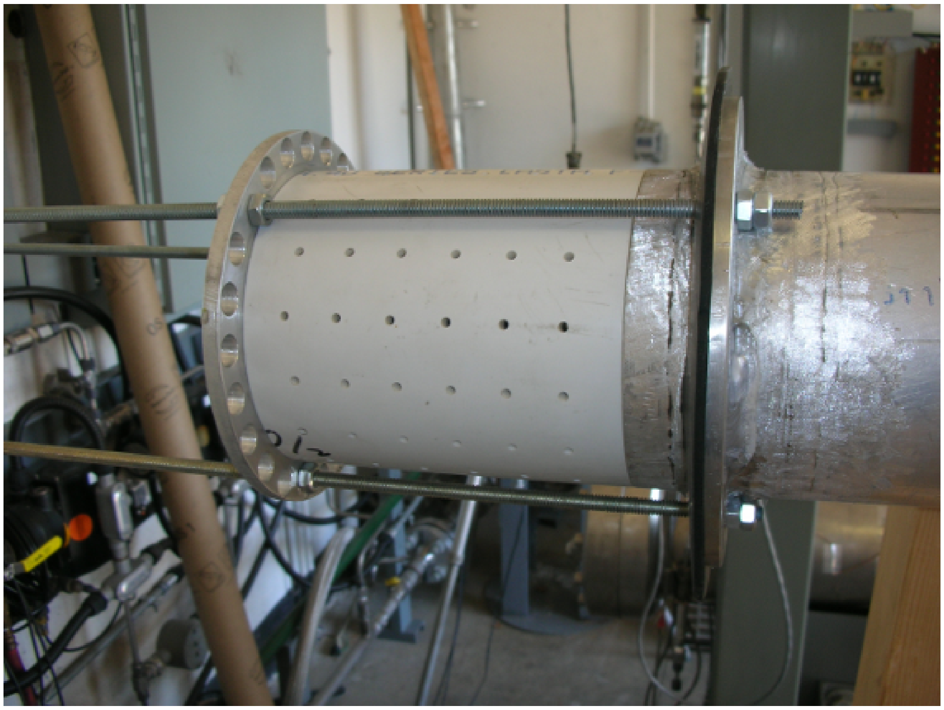

Figure 7.3: Injector

For this reason equation 7.1 is slightly modified:

$$Q = nC_d\sqrt{\frac{2\Delta p}{\rho}}\frac{\pi}{4}\frac{{D_H}^2}{\sqrt{1-\left(\frac{{D_H}^2}{{D_{Man}}^2-{D_{Inj}}^2}\right)^2}} \tag{7.2}$$

Here n represents the number of holes in the injector, D_H the diameter of the holes, D_{Man} the diameter of the manifold and D_{Inj} the diameter of the injector. The factor C_d has to be determined by a trial and error approach. The estimated flow rate Q based on equation 7.2 is within 5% of the measured flow rate if C_d equals unity, therefore:

$$C_d \approx 1 \tag{7.3}$$

The final design features 96 holes with a 1/8 inch diameter. It is built from a 5 inch long PVC tube with an inner diameter of 4 inches. Figure 7.3 displays the injector with the manifold removed. The resulting "on design" flow conditions are listed in table 7.1.

Table 7.1: Flow Conditions

Mass Flow Rate	$\dot{m}$	0.75	$\frac{lbm}{s}$
Mean Pressure in Main Chamber	p_0	16	psi
Pressure Drop across Injector	Δp	9	psi
Mean Flow Speed in Main Chamber	W_0	17	$\frac{m}{s}$
Mach Number in Main Chamber	M_0	0.05	
Speed of Sound	a_0	330	$\frac{m}{s}$
Natural Frequency of the First Longitudinal Mode	f_1	75	Hz
Background Noise		107	dB

7.1.2 Instrumentation

Four quantities are measured while the experiment is performed. The mass flow rate, the static pressure in the manifold, the static pressure in the main chamber and the dynamic sound pressure level in the main chamber. The positioning of the sensors is indicated in figure 7.1.

The mass flow rate is determined by two static pressure sensors that are installed in the air supply pipe upstream and downstream from an orifice with known properties. The mass flow rate is calculated from the pressure difference across this orifice.

An Omega PX605-060GI static pressure sensor with the range of 60psi is installed in the sidewall of the manifold upstream of the injector, another Omega PX605-030GI static pressure sensor with the range of 30psi is installed in the end plate of the main chamber. These two sensors are used to monitor the pressure drop across the injector and to verify that choked flow at the nozzle is maintained continuously while data is collected.

The dynamic pressure in the chamber is measured using a Bruel & Kjær model 4138 1/8 inch microphone, which is mounted flush in the end wall with a radial distance from the nozzle of 1 inch. The microphone works with an accuracy of 0.2dB over a range from 0 to 20kHz.

The position of the microphone is chosen, because all longitudinal oscillation modes have a pressure anti-node at the end plate. This is also true for the head end, but noise generated by the injection process might impair the measurements. A disadvantage of the mounting of the microphone in the end wall is that the noise level increases dramatically as the position of

the baffle approaches $Z_0/L \approx 0.8$. The microphone is then hit directly by decaying vortices shed form the baffle, which drowns the signal of the pressure oscillations.
The data is recorded in terms of the sound pressure level L_p with a reference pressure of $p_{ref} = 20\mu Pa$, which is considered the threshold of human hearing.

$$L_p = 20\log_{10}\left(\frac{p_1}{p_{ref}}\right) dB \tag{7.4}$$

7.2 The Procedure

The experiment is operated with an air mass flow of 0.75lbm/s. This flow rate results in a static pressure of 16psi in the main chamber and 25psi in the manifold. Figure 7.4 shows a typical pressure trace of a run. The sawtooth-like profile stems from a slightly ever increasing mass flow rate, which has to be adjusted several times during a run of the experiment. This phenomenon occurs due to cooling of the regulating valves as the air flow is expanded from 3000psi upstream at the compressor to 25psi in the manifold. Collecting a full dataset for a baffle takes approximately 40 minutes.
At the beginning of a run each baffle is positioned at $Z_0/L = 0.25$. It is then moved downstream with increments of 1 inch to $Z_0/L = 0.75$. Spectral data of the dynamic sound pressure level is recorded for every position of the baffle. The analog signal from the microphone is converted to a digital output using a National Instruments SCX1313 converter. Raw data in the time domain is collected over a span of 2 seconds and then decomposed into its constituent frequencies by running a Fourier transformation on it using LabView. For each position of the baffle this procedure is repeated 10 times. A final data point is obtained by taking the average of the 10 spectra. The averaging and post-processing of the spectral data is done with Wolfram Mathematica.
The experiment is performed with various baffle sizes, their dimensions are given in table 7.2.

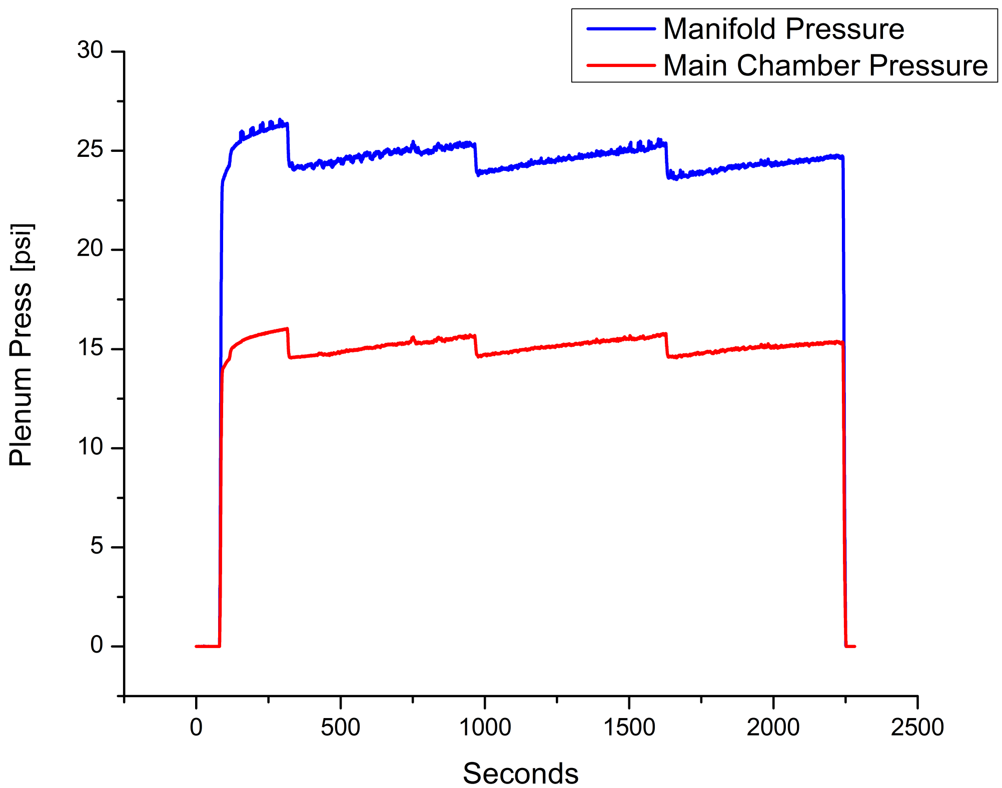

Figure 7.4: Pressure Trace of a Typical Run of the Experiment

Table 7.2: Dimensions of Tested Baffles

External Diameter [in]	Internal Diameter [in]	Relative Height R_0/R
4.25	3.5	0.82
4.25	3.25	0.75
4.25	3.0	0.70
4.25	2.75	0.65
4.25	2.5	0.59
4.25	2.25	0.53
4.25	2.0	0.47

7.3 Data

The data obtained from the experiment is first presented without explanation. Conclusions that can be drawn from the results are discussed in section 7.4. The discussion is done exemplarily for the baffle size of $R_0/R = 0.47$. In this case the vortex shedding effects are most pronounced, whereas the statements also apply to the other cases.
Enlarged versions of the plots can be found in appendix B.1.

7.3.1 Base Flow

The base flow is determined by running the experiment with an empty main chamber. In this configuration the data ideally only shows broadband white noise and no distinct oscillation modes can be detected. If this was the case, the effect of the vortex shedding on the acoustics could be isolated easily. Figure 7.5 shows the frequency spectrum for the base flow. It is very evident that ideal white noise frequency distribution is not achieved. In fact, all longitudinal modes from the 1st to the 13th mode can be identified individually. Finding a conclusive explanation why this effect occurs is difficult, but it is most likely related to the injection process. The injector does not sufficiently inhibit acoustic feedback from the manifold and the air column in the supply pipe. A higher pressure drop across the injector would be desirable but could not be realized in the present study. When interpreting the data for the test runs with the baffles, the base flow must be considered.

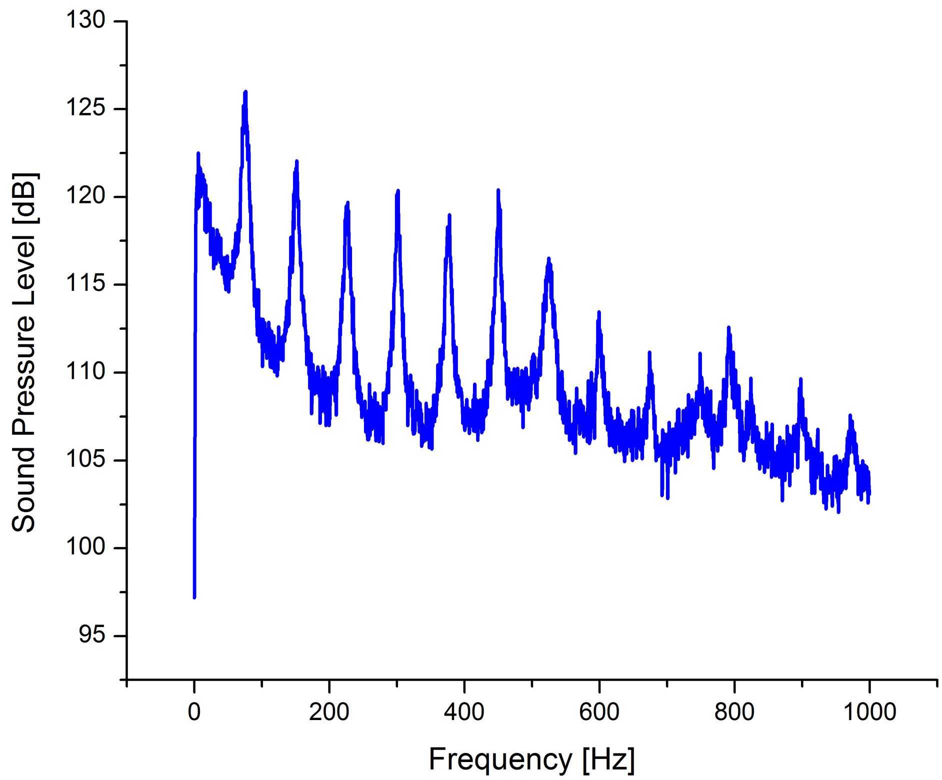

Figure 7.5: Frequency Spectrum of the Base Flow

7.3.2 Baffle with $R_0/R = 0.82$

An annular baffle with the relative height of $R_0/R = 0.82$ is inserted into the main chamber and moved from $Z_0/L = 0.25$ to $Z_0/L = 0.75$ in 1 inch increments while air is flowing at a rate of 0.75lbm/s. This relatively low baffle blocks one third of the chamber cross section. Figure 7.6 displays a 3-D surface plot of the sound pressure level as a function of the position Z_0/L and the oscillation frequency f_m. An enlarged version of figure 7.6 as well as a contour plot can be found in appendix B.1.1.

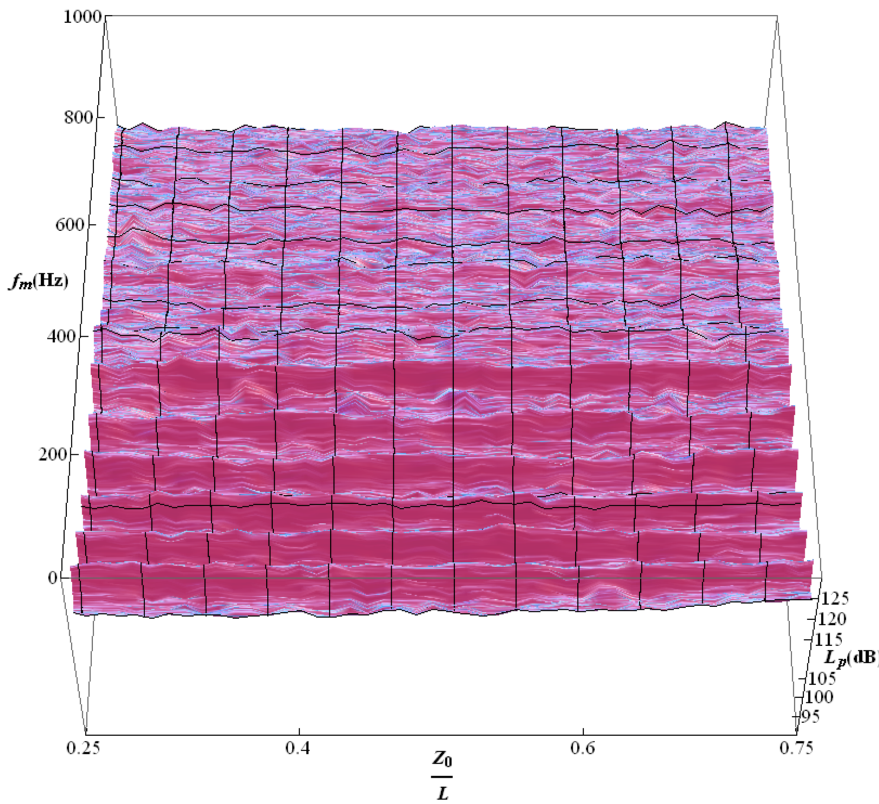

Figure 7.6: Spectral Data. Baffle with $R_0/R = 0.82$

7.3.3 Baffle with $R_0/R = 0.75$

An annular baffle with the relative height of $R_0/R = 0.75$ is inserted into main chamber and moved from $Z_0/L = 0.25$ to $Z_0/L = 0.75$ in 1 inch increments while air is flowing at a rate of 0.75lbm/s. This baffle blocks 44% of the chamber cross section. Figure 7.7 displays a 3-D surface plot of the sound pressure level as a function of the position Z_0/L and the oscillation frequency f_m. An enlarged version of figure 7.7 as well as a contour plot can be found in appendix B.1.2.

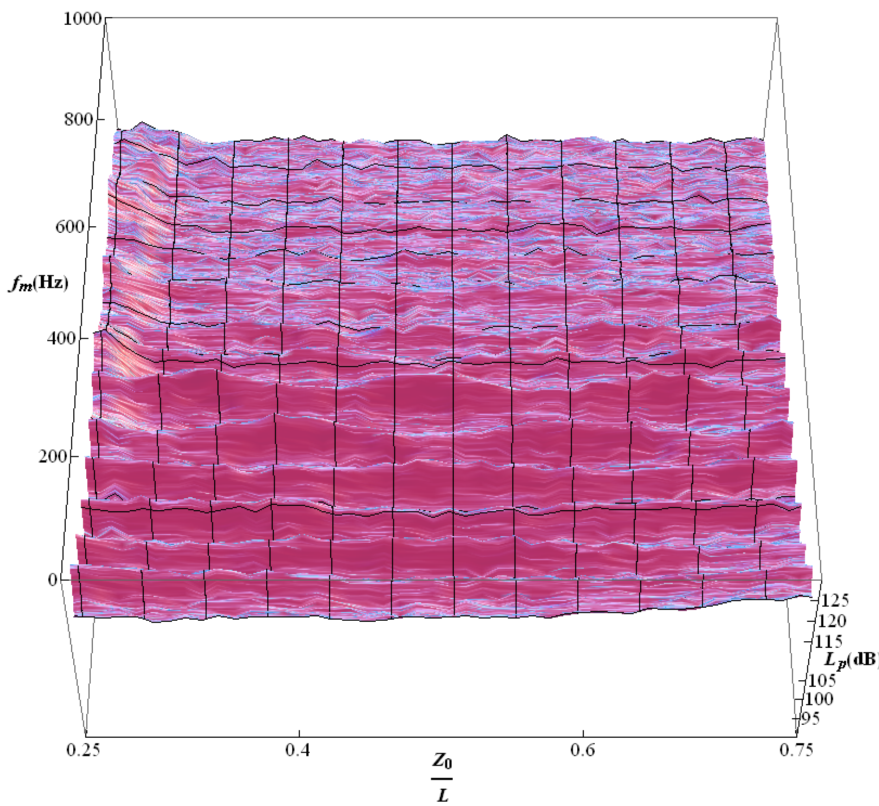

Figure 7.7: Spectral Data. Baffle with $R_0/R = 0.75$

7.3.4 Baffle with $R_0/R = 0.70$

An annular baffle with the relative height of $R_0/R = 0.70$ is inserted into main chamber and moved from $Z_0/L = 0.25$ to $Z_0/L = 0.75$ in 1 inch increments while air is flowing at a rate of 0.75lbm/s. This baffle blocks 51% of the chamber cross section. Figure 7.8 displays a 3-D surface plot of the sound pressure level as a function of the position Z_0/L and the oscillation frequency f_m. An enlarged version of figure 7.8 as well as a contour plot can be found in appendix B.1.3.

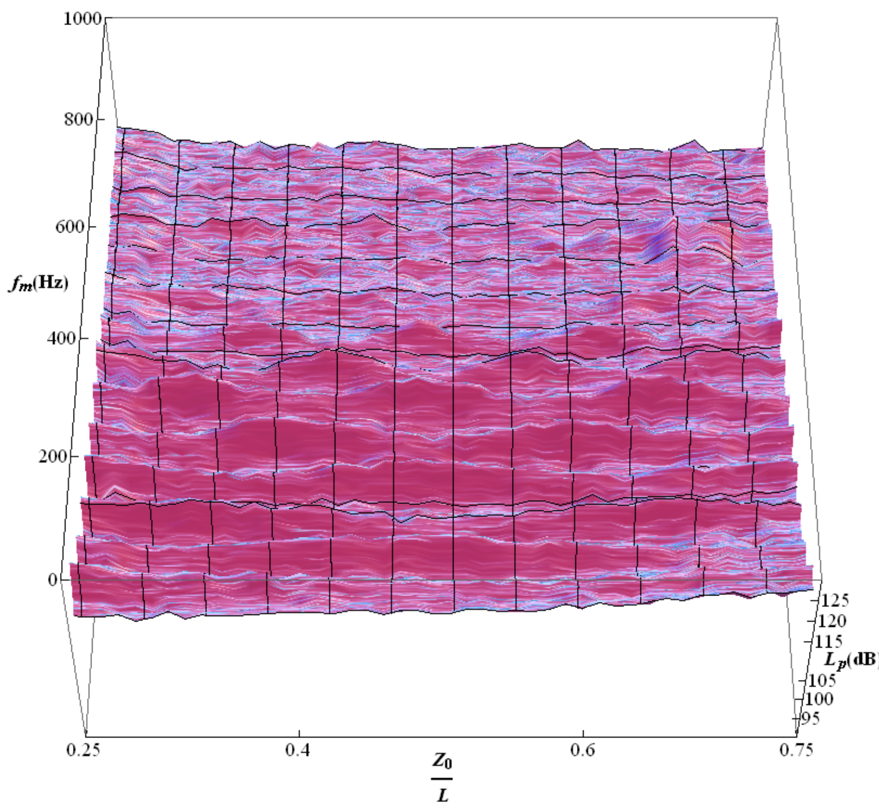

Figure 7.8: Spectral Data. Baffle with $R_0/R = 0.70$

7.3.5 Baffle with $R_0/R = 0.65$

An annular baffle with the relative height of $R_0/R = 0.65$ is inserted into main chamber and moved from $Z_0/L = 0.25$ to $Z_0/L = 0.75$ in 1 inch increments while air is flowing at a rate of 0.75lbm/s. This baffle blocks 58% of the chamber cross section. Figure 7.9 displays a 3-D surface plot of the sound pressure level as a function of the position Z_0/L and the oscillation frequency f_m. An enlarged version of figure 7.9 as well as a contour plot can be found in appendix B.1.4.

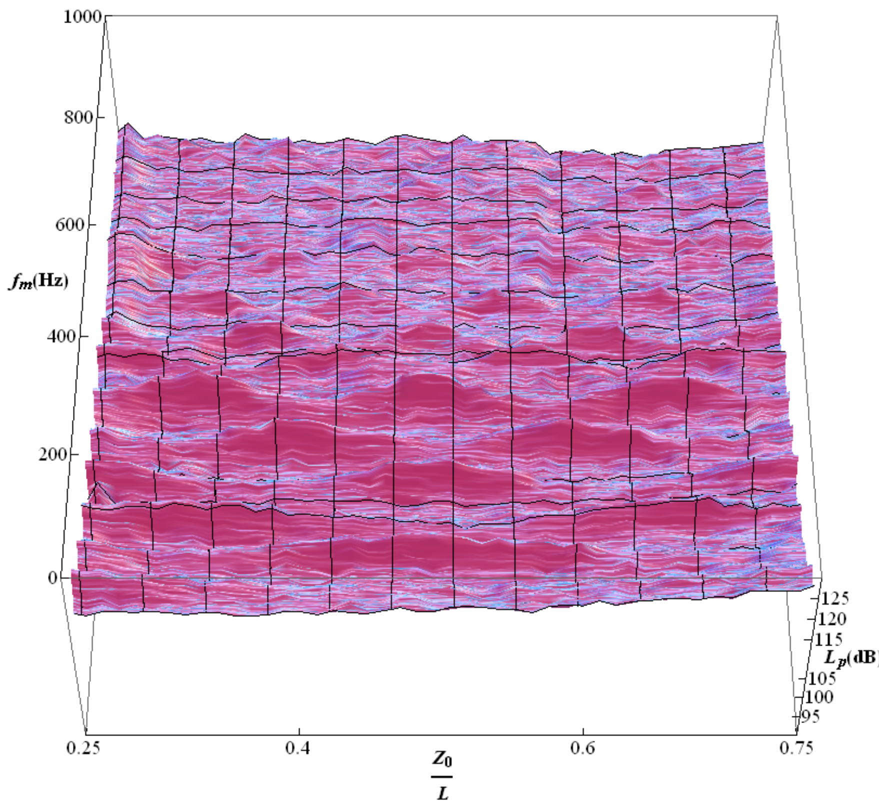

Figure 7.9: Spectral Data. Baffle with $R_0/R = 0.65$

7.3.6 Baffle with $R_0/R = 0.59$

An annular baffle with the relative height of $R_0/R = 0.59$ is inserted into main chamber and moved from $Z_0/L = 0.25$ to $Z_0/L = 0.75$ in 1 inch increments while air is flowing at a rate of 0.75lbm/s. This baffle blocks 65% of the chamber cross section. Figure 7.10 displays a 3-D surface plot of the sound pressure level as a function of the position Z_0/L and the oscillation frequency f_m. An enlarged version of figure 7.10 as well as a contour plot can be found in appendix B.1.5.

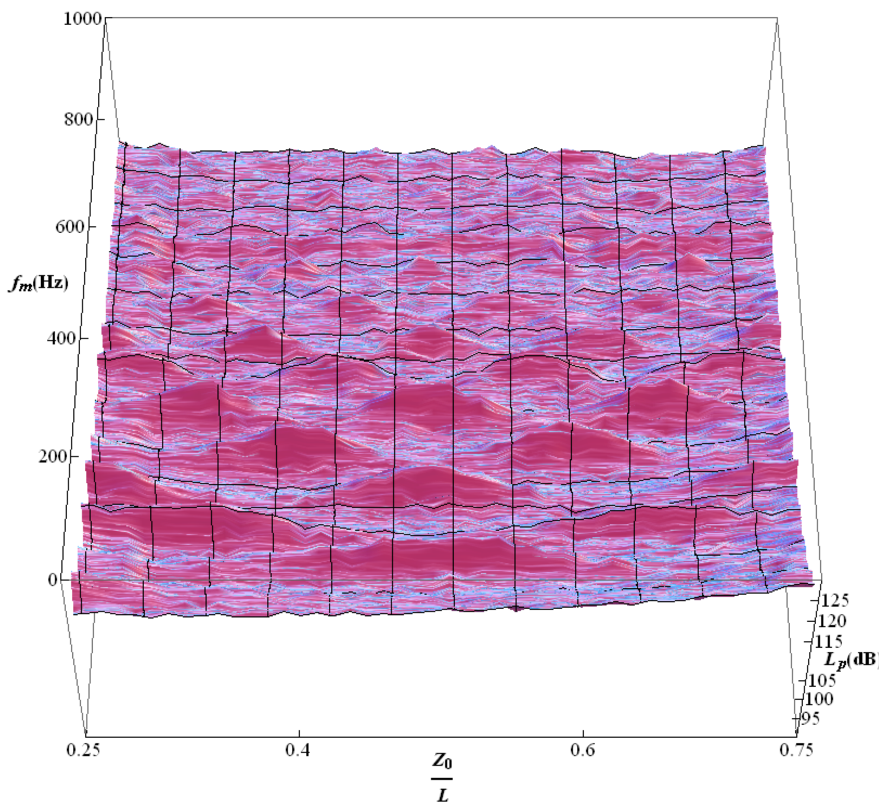

Figure 7.10: Spectral Data. Baffle with $R_0/R = 0.59$

7.3.7 Baffle with $R_0/R = 0.53$

An annular baffle with the relative height of $R_0/R = 0.53$ is inserted into main chamber and moved from $Z_0/L = 0.25$ to $Z_0/L = 0.75$ in 1 inch increments while air is flowing at a rate of 0.75lbm/s. This baffle blocks 72% of the chamber cross section. Figure 7.11 displays a 3-D surface plot of the sound pressure level as a function of the position Z_0/L and the oscillation frequency f_m. An enlarged version of figure 7.11 as well as a contour plot can be found in appendix B.1.6.

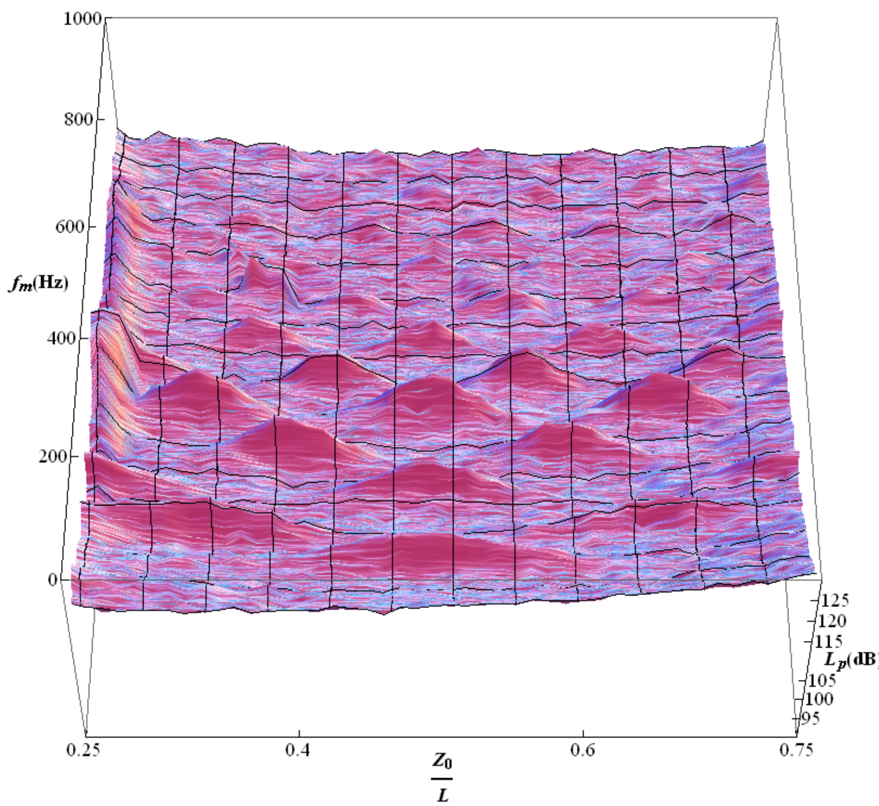

Figure 7.11: Spectral Data. Baffle with $R_0/R = 0.53$

7.3.8 Baffle with $R_0/R = 0.47$

An annular baffle with the relative height of $R_0/R = 0.47$ is inserted into main chamber and moved from $Z_0/L = 0.25$ to $Z_0/L = 0.75$ in 1 inch increments while air is flowing at a rate of 0.75lbm/s. This baffle blocks 78% of the chamber cross section. Figure 7.12 displays a 3-D surface plot of the sound pressure level as a function of the position Z_0/L and the oscillation frequency f_m. A contour plot of the data can be seen in figure 7.13, the dashed orange lines correspond to the (longitudinal) harmonics of the test chamber (multiples of 75Hz). Enlarged versions of figure 7.12 and figure 7.13 can be found in appendix B.1.7.

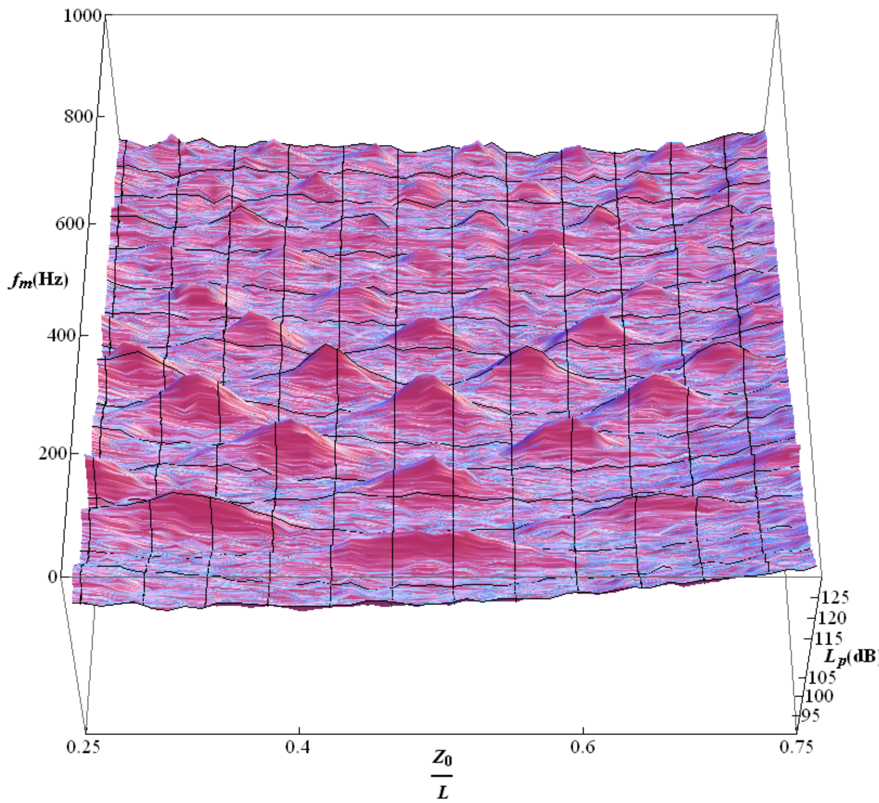

Figure 7.12: Spectral Data. Baffle with $R_0/R = 0.47$

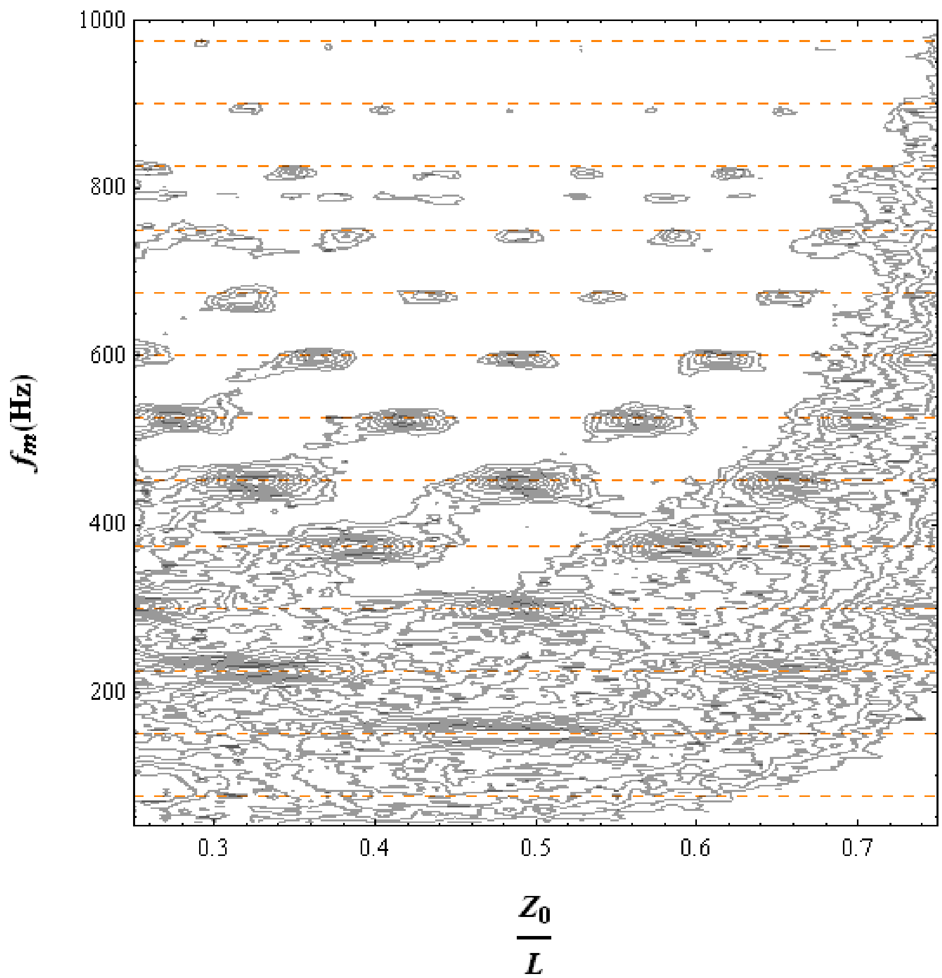

Figure 7.13: Contour Plot of the Spectral Data. Baffle with $R_0/R = 0.47$

7.4 Discussion

The theoretical linear growth rate α_{VS} is compared qualitatively to the experimental data. Pressure oscillations of those longitudinal Normal modes, for which α_{VS} is greatest, are expected to be most prominent. A direct quantitative comparison of theoretical and experimental (limit-cycle) amplitudes is impeded by the linear nature of the growth rate (see chapter 6). However, the widely used Standard Stability Prediction program (SSP) is based entirely on linear considerations [47].

All statements made here apply to all experimental test cases, but can be elucidated most easily based on data from the run with the tallest ring size of $R_0/R = 0.47$.

The size of the ring affects how much the spectral pattern deviates from the base flow. The taller the baffle, the more distinct the pattern of figure 7.14 becomes. More oscillatory energy is concentrated into narrower regions, which includes a slight decrease of the background noise, at the same time higher modes become more pronounced.

Figure 7.14 shows a contour plot of the theoretical α_{VS} (red contours, also see figure 5.3(b)) on top of a contour plot of the experimental data for $R_0/R = 0.47$ (black contours, also see figure 7.13). The dashed orange horizontal lines mark the longitudinal natural frequencies of the main chamber (multiples of 75Hz). The green lines 1, 2 and 3 have been inserted to highlight certain positions of the baffle, the green lines 4 and 5 follow the first two branches on which α_{VS} peaks. The growth rate α_{VS} is calculated according to equation 5.114 with a set of parameters that matches the conditions of the experiment in chapter 7: $L = 89'', R_0/R = 0.47, W_0 = 17m/s, a_0 = 340m/s, \theta = 10^{-4}m$.

Figure 7.15 depicts a colored contour plot of α_{VS} for comparison (also see fig. 5.3(a)).

The experimental data shows that the position of the baffle has a distinct effect on which particular modes are driven. These modes happen to be the longitudinal Eigenmodes of the main chamber. Even for the tallest baffle with a blockage of the tube of 78 % , only the full chamber resonates. Effects like the acoustic separation of the tube into two parts and the associated resonance of alien modes are not observed. Note that the ring size cannot be increased much further without choking the flow at the baffle, which is an unlikely scenario in a real solid rocket motor.

A very important conclusion can be drawn when looking at the intersection of the green lines 3 and 4. Along line 3 the growth rate of the second mode is higher than the growth rate of the first mode. Consequently the first mode disappears completely and all energy is shifted into the second mode (150Hz) - as predicted by the theory! This is remarkable because the base flow exhibits its highest oscillation amplitude of 127dB at the first mode (75Hz), still the second mode prevails in the experimental data.

The same applies to the intersection of line 2 and line 4. Along line 2 the growth rate of the third mode is higher than the growth rate of the first and second mode and consequently only the third mode is evident in the experimental data. Another example, this time for the fourth mode, can be found at the intersection of line 1 and line 4.

While the experimental data closely matches the predictions on the first branch, following line 5 shows that there are no amplitude peaks in the data along this line, even though α_{VS} peaks along line 5 on the second branch. This can be explained by non-linear cascading of oscillatory energy into the multiples of a mode [42].

When following line 3 it is evident that the second mode is driven strongly. Energy from the first and third is absorbed into the second mode. Although α_{VS} of the fourth mode is comparatively low, it shows up clearly in the data. This is because energy has cascaded from the second into the forth mode - and also into the sixth, the eighth and tenth mode. On the second branch α_{VS} is maximal for the seventh mode at the intersection of line 3 and 5. However, the neighboring sixth and eighth mode are fed from the second mode, therefore energy is pulled from the seventh, which consequently does not show up in the data. Similar behavior can be observed along line 2, this time with multiples of the third mode.

In conclusion, some remarks on the Strouhal number: Brown et al. [17] defined a critical Strouhal number for the onset of vortex driven flow instability of the order of unity or less according to equation 1.2, where f denotes the oscillation frequency, D the internal diameter of the baffle and U the mean flow speed:

$$\mathrm{St} = \frac{fD}{U}$$

Figure 7.14 shows that all modes from the first through the 12th mode are driven, depending on the position of the baffle. For the experimental configuration used here, this translates into a range of Strouhal numbers of 0.2 for the first mode to 2.7 for the 12th mode - which is in good agreement with the prediction of Brown et al. [17].

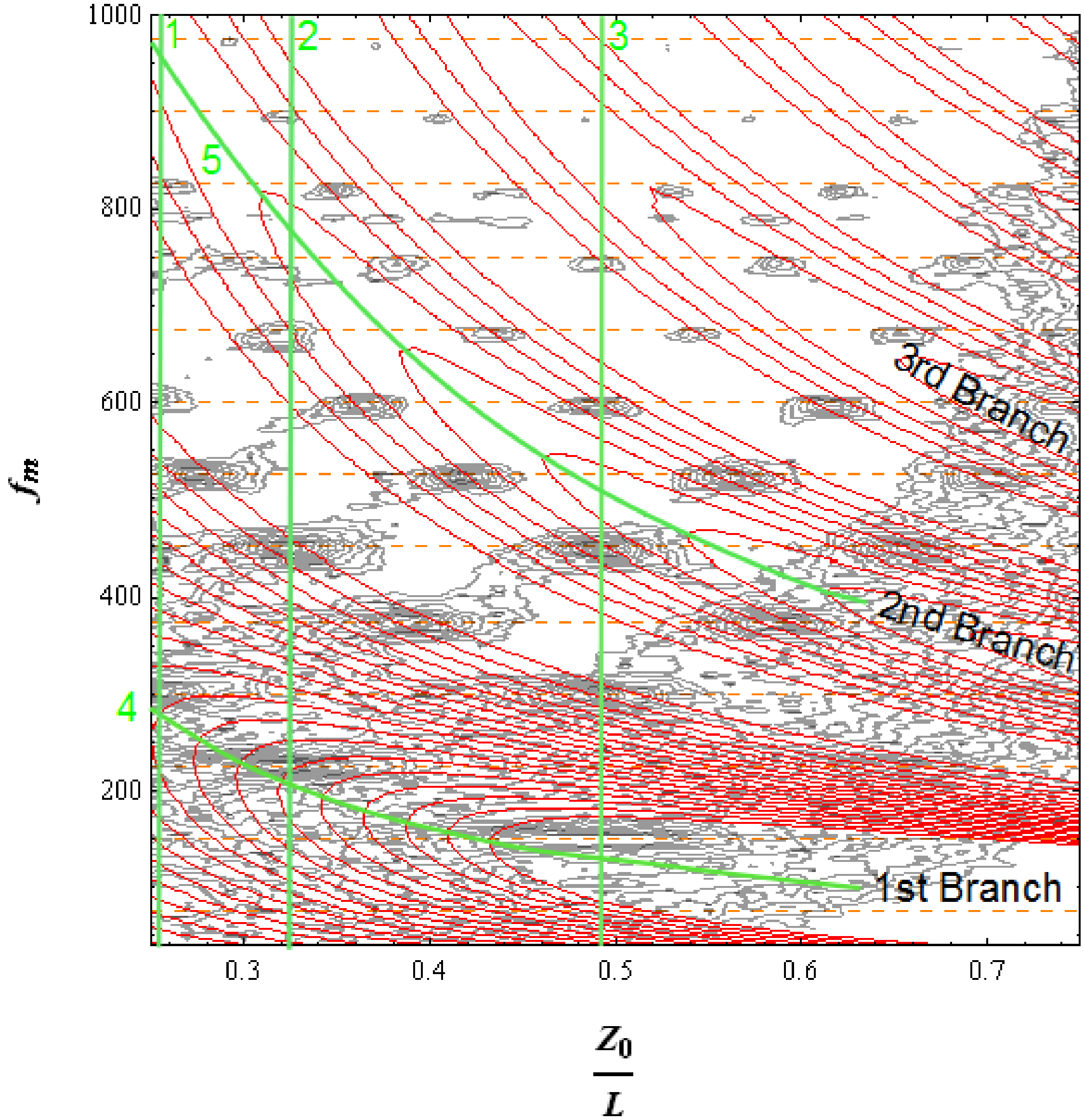

Figure 7.14: Contour Plots of α_{VS} (red) and Experimental Data for $R_0/R = 0.47$ (black)

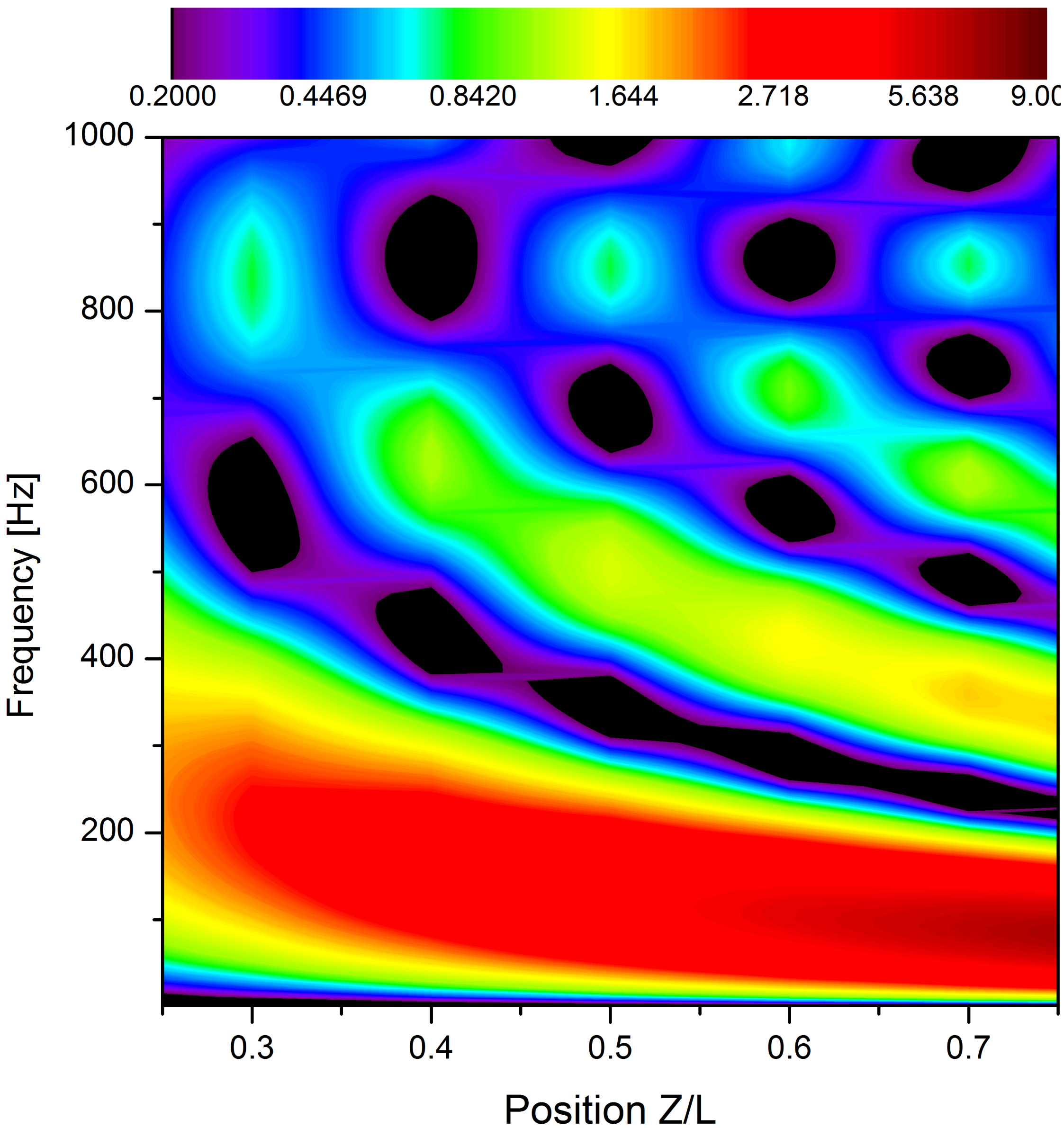

Figure 7.15: Contour Plot of Theoretical Growth Rate α_{VS}

Chapter 8

Summary and Recommendations

This dissertation investigates the interaction between vortex shedding and the internal acoustics of a solid rocket motor. Two different mechanisms that drive pressure oscillations by the presence of vortices in the flow have been identified in the literature [9]. One is the periodical impingement of the vortices on a a hard surface, another one is the instability of the shear layer itself under the influence of an acoustic field.

The present study focuses on the latter phenomenon and therefore on the linking of the acoustics to the unsteady vorticity that is created in the highly sheared flow behind an obstacle. This shear layer is objected to longitudinal pressure oscillations in a chamber with acoustic closed-closed end conditions.

A theoretical approach is developed based on modeling of the second order acoustic energy. The energy model is applied to the specific flow conditions behind a baffle or backward facing step in a solid rocket motor. This method leads to the (linear) growth rate of the oscillation amplitudes α_{VS}. The growth rate is found to be a function of the position of the point of separation of the shear layer and the oscillation frequency.

In order to validate the theoretical findings, a cold flow experiment is performed. A single annular baffle is inserted into a tube with a solid head end and a choked nozzle at the exit plane. An airflow is injected radially at the head end. The size of the baffle and its axial position are varied while spectral data of the pressure oscillations is recorded.

The experimental results are then compared qualitatively to the theoretical growth rates of the oscillations. Those longitudinal Normal modes, which feature the highest theoretical growth rates, are expected to be most prominent in the experimental data. Even though the theoretical part does not include non-linear effects and therefore does not allow for predictions of limit cycle amplitudes, good agreement between the theory and the experimental data is found.

Future investigations may start from the second order considerations and incorporate the third order energy expansions yielding the non-linear growth rates of the oscillation amplitudes. In this process the assumption that the kinetic energy carried by the vorticity waves is much smaller than the kinetic energy carried by acoustic waves might have to be relaxed, which would require an explicit solution for the rotational velocities. Based on the non-linear growth rates, the final non-linear limit cycle amplitudes could be predicted and compared to experimental data not only qualitatively but also quantitatively.

In order to match predictions of the limit cycle amplitudes with experimental data, all energy sources (and sinks) for the pressure oscillations have to be precisely controlled. The experimental data presented here is impaired by the fact that oscillations are driven not only by the presence of an unstable shear layer downstream from a flow restrictor but also by the injection process of the airflow into the test chamber. The effect of the injection on the pressure oscillations would have to be either investigated analytically or eliminated experimentally, in order to successfully prove a non-linear expansion of the theory for vortex driven flow instability. The easier solution to this problem appears to be the elimination of oscillations driven by the injection. This could be achieved by using a more sophisticated injector. An injector made from a porous sintered material might create a much smoother airflow at the head end and generate a higher pressure drop. This would ensure that the test chamber is acoustically decoupled from the gas column upstream of the injector. Of course, a higher pressure drop would lead to higher pressures in the system, which would require an overall sturdier build of the apparatus.

Bibliography

[1] Bloomshield, F. S., "Lessons Learned in Solid Rocket Combustion Instability", *43th AIAA Joint Propulsion Conference*, AIAA-2007-5803, Cincinnati, OH, July 2007.

[2] Flandro, G. A., "Effects of Vorticity on Rocket Combustion Stability," *Journal of Propulsion and Power*, Vol. 11, No. 4, 1995, pp. 607-625.

[3] Flandro, G. A., Perry, E. H., and French, J. C., "Nonlinear Rocket Motor Stability Computations: Understanding the Brownlee-Marble Observations" *44th AIAA Aerospace Sciences Meeting and Exhibit* AIAA-2006-539, 2006.

[4] Oefelein, J., and Yang, V., "Comprehensive Review of Liquid Propellant Combustion Instabilities in F-1 Engines," *J. Prop. and Power*, Vol. 9, No. 5, 1993, pp. 657-677.

[5] Blomshield, F. S., Stalnaker, R. A., Beckstead, M. W.and Stokes, B., "Aluminum Combustion Effects on Combustion Instability of High Burn Rate Propellants," *28th JANNAF Combustion Meeting*, CPIA Publication 573, Vol. III, pp. 419-438, October 1991.

[6] Beckstead, M. W., and Brooks,K. P., "A Model for Distributed Combustion in Solid Propellants," *27th JANNAF Combustion Meeting*, CPIA Publication 557, Vol. II, pp. 237-258, November 1990

[7] Coates, R. L., Horton, M. D., Ryan, N. W., "T-Burner Method of Determining the Acoustic Admittance of Burning Propellants," *AIAA Journal*, 1964, pp 1119-1127.

[8] Flandro, G. A., "Vortex Driving Mechanisms in Oscillatory Rocket Flows," *AIAA Journal*, Vol. 2, No. 3, 1986, pp. 208-214.

[9] Vuillot, F., "Vortex Shedding Phenomena in Solid Rocket Motors," *J. Propulsion and Power*, Vol. 11, No. 4, 1995, pp. 626-639.

[10] Culick, F. E. C., "Stability of Longitudinal Oscillations with Pressure and Velocity Coupling in Solid Propellant Rocket", *Combustion Science and Technology*, Vol. 2, pp. 179-201, 1970.

[11] Blomshield, F. S., Stalnaker,R. A., and Beckstead, M. W., "Combustion Instability Additive Investigation" *AIAA Joint Propulsion Meeting*, Paper No. 99-2226, Los Angeles, June 1999.

[12] Flandro, G.A., "On Flow Turning," *31st AIAA Joint Propulsion Conference*, AIAA 95-2730, San Diego, CA, July 1995.

[13] Wilson, A., "Nonlinear Acoustics of Piston-Driven Gas-Column Ascillations," MS Thesis, The Univeristy of Tennessee Space Institute, 2010.

[14] Culick, F. E. C., "The Stability of One-Dimensional Motions on a Rocket Motor," *Combustion Science and Technology*, Vol. 7, No. 4, 1973, pp. 165-175.

[15] Scippa, S., Pascal, P., and Zanier, F., "Ariane5 MPS Chamber Pressure Oscillations Full Scale Firing Results Analysis and Further Studies", AIAA Paper 94-3068, June 1994

[16] Nesman, T., "RSRM Chamber Pressure Oscillations: Full Scale Ground and Flight Test Summary and Air Flow Test Results", *31st AIAA Joint Propulsion Conference*, July 1995.

[17] Brown, R.S., Dunlap, R., Young, S.W., and Waugh, R.C., "Vortex Shedding as a Source of Acoustic Energy in Segmented Solid Rockets", *Journal of Spacecrafts and Rockets*, Vol.18, No 4, 1981, pp. 312-319.

[18] Feretti, V., Flavini, B., Cavallini, E., Serraglia, F., Di Giacinto, M., "Numerical Simulations of Acoustic Resonance of Solid Rocket Motor" *46th AIAA Joint Propulsion Conference* AIAA 2010-6996, Nashville, TN, July 2010.

[19] French, J., "Non-Linear Combustion Stability Prediction of SRMS Using SPP/SSP" *39th AIAA Joint Propulsion Conference* AIAA 2003-4668, Huntsville, AL, July 2003.

[20] Flandro, G. A., "Vortex Driving Mechanisms in Oscillatory Rocket Flows," *Journal of Propulsion and Power*, Vol. 2, No. 3, 1986, pp. 206-214.

[21] Dawson, M. C., Andrepont, W. C., Luther, D. L., and Flandro, G. A., "Elimination of Flow Induced Instabilities in Solid Rocket.

[22] Jacob, E. J., Flandro, G. A, and Banuti, D., "Forced Resonant Shock Waves and Mean Pressure Shift in a Closed Tube," *AIAA Joint Propulsion Conference*, AIAA-2007-5806, 2007.

[23] Isakowitz, S., "The Commercial Evolution of the Titan Program", *24th AIAA Joint Propulsion Conference*, AIAA-88-3119, Boston, MA, July 1988.

[24] Lovine, R. L. and Waugh, R.C., "Standard Stability Prediction Method for Solid Rocket Motors", CPIA Publication 273, Aug. 1975.

[25] Prévost, M., Godon, J. C., Innegraeve, O., "Thrust Oscillations in reduced Scale Solid Rocket Motors, part I: Experimental Investigations", *41th AIAA Joint Propulsion Conference*, AIAA 2005-4003, Tucson, AZ, July 2005.

[26] Lupoglazoff, N. and Vuillot, F., "Parietal vortex shedding as a cause of instability for long solid propellant motors - Numerial simulations and comparisons with firing tests", *AIAA 34th Aerospace Sciences Meeting and Exhibit*, AIAA 96-0761, Reno, NV, January 1996.

[27] Blomshield, F. S., "Historical Perspective of Combustion Instability in Motors: Case Studies", *37th AIAA Joint Propulsion Conference*, AIAA-2001-3875, Salt Lake City, UT, July 2001.

[28] Blomshield, F. S. and Mathes, H. B., "Pressure Oscillations in Post-Challenger Space Shuttle Redesigned Solid Rocket Motors", *Journal of Propulsion and Power*, Vol.9, No. 2., pp 217-221, 1993.

[29] Blomshield F. S., and Bicker, C. J., "Pressure Oscillations in Shuttle Solid Rocket Motors," *33rd AIAA/ASME/SAE/ASEE Joint Propulsion Conference and Exhibit*, AIAA-1997-3252, 1997.

[30] Priskos, A. S. and Tiller, B., "Progress on Ares First Stage Propulsion", *44th AIAA Joint Propulsion Conference*, AIAA-2008-4895, Hartford, CT, July 2008.

[31] Carreau, M., "Severe Vibration Problem Plagues Moon Rocket Design," *Houston Chronicle*, Jan. 19, 2008.

[32] Brownlee, W. G., and Marble, F. E., "An Experimental Investigation of Unstable Combustion in Solid Propellant Rocket Motors," *ARS Progress in Astronautics and Rocketry: Solid Propellant Rocket Research*, Vol. 1, edited by M. Summerfield, Academic Press Inc., New York, 1960, pp. 455-494.

[33] Brownlee, W. G., "An Experimental Investigation of Unstable Combustion in Solid Propellant Rocket Motors," *PhD Thesis*, California Institute of Technology, 1959.

[34] Brownlee, W. G., "Nonlinear Axial Mode Combustion Instability in Solid Propellant Motors," *AIAA Journal*, Vol. 2, pp. 275-284, Feb. 1964.

[35] Culick, F. E. C., "Acoustic Oscillations in Solid Propellant Rocket Chambers", *Acta Astronautica*, Vol. 12, No.2, 1966, pp. 113-126.

[36] Myers, M. K., "Transport of Energy by Disturbances in Arbitrary Steady Flows," *J. Fluid Mechanics*, Vol. 226, 1991, pp. 383-400.

[37] Cantrell, R. H., and Hart, R. W., "Interaction Between Sound and Flow in Acoustic Cavities: Mass, Momentum, and Energy Considerations," *Journal of the Acoustical Society of America*, Vol. 36, No. 4, 1964, pp. 697-706.

[38] Morfey, C. L., "Acoustic Energy in Non-uniform Flows," *J. Sound and Vibrations*, Vol. 14, 1971, pp. 159-169.

[39] Flandro, G. A., Fischbach, S. R., Majdalani, J., and French, J. C., "Nonlinear Rocket Motor Stability Prediction: Limit Amplitude, Triggering, and Mean Pressure Shift," *Physics of FLuids*, Vol. 19, Issue 9, 094101, 2007.

[40] Flandro, G. A., and Jacob, E. J., "Irregular Burning: On the Origin of the DC Shift," *43rd AIAA Joint Propulsion Conference*, AIAA Paper No. 2007-5809, July 2007.

[41] Flandro, G. A., "On the Oscillatory Behavior of Liquid Propellant Rockets", *Advancements in Energetic Materials and Chemical Propulsion*, 2008, pp. 320-363.

[42] Jacob, E. J., "A Study of Nonlinear Combustion Instability," PhD Dissertation, The University of Tennessee Space Institute, 2009.

[43] Landau, L. D., and Lifshitz, E. M., "Fluid Mechanics," *Butterworth-Heinemann*, Second Edition, 1987, pp 1-92.

[44] Enflo, B. O., and Hedberg, C. M., "Theory of Nonlinear Acoustics in Fluids," *Kluwer Academic Publishers*, 2002, pp. 11-24.

[45] Liepmann, H. W., and Roshko, A., "Elements of Gasdynamics," *Dover Publications*, 1957.

[46] Nayfeh A. H., "Introduction to Perturbation Techniques", Wiley Classics Library Edition, *John Wiley & Sons*, 1981.

[47] Culick, F. E. C., and Yang, V., "Stability Predictions in Rockets," Nonsteady Burning and Combustion Stability of Solid Propellants, *Progress in Astronautics and Aeronautics*, TR 83-017, Vol. 143, 1992, pp. 719-799.

[48] Morse, P. M., and Ingard, K. U., "Theoretical Acoustics," *McGraw-Hill*, 1968.

[49] Pierce, A. D. "Acoustics: An Introduction to Its Physical Principles and Applications," *Acoustical Society of America*, 1989.

[50] Quarteroni, A., Sacco, R. and Saleri, F., "Numerical Mathematics," *Springer Berlin Heidelberg*, 2007, pp. 556-571.

[51] Lin, C.C., "The Theory of Hydrodynamic Instability", *Cambridge University Press*, 1955.

[52] Michalke, A., "On Spatially Growing Disturbances in an Inviscid Shear Layer", *Journal of Fluid Mechanics*, Vol. 23, 1965, pp. 521-544.

[53] French, J. C., Flandro, G. A., Personal Communication, 2010.

[54] Flandro, G. A., Majdalani, J., "Aeroacoustic Instability in Rockets," *37rd AIAA Joint Propulsion Conference*, AIAA Paper No. 2001-3868, July 2001.

[55] Flatau, A., Van Moorhem, W. K., "Vortex Shedding Induced Sound Inside a Cold-Flow Simulation of Segmented Chamber", *Journal of Propulsion and Power* Vol. 19, No. 2, 2003.

Appendices

Appendix A

A.1 Common Vector Identities:

Several vector identities are useful in the manipulation of vector equations.

$$
\begin{aligned}
\nabla \times (\nabla \mathrm{s}) &= 0 \\
\nabla \cdot (\nabla \times \mathbf{v}) &= 0 \\
\nabla \cdot (\nabla s) &= \nabla^2 s \\
\nabla \times \nabla \times \mathbf{v} &= \nabla (\nabla \cdot \mathbf{v}) - \nabla^2 \mathbf{v} \\
\nabla \cdot (\mathbf{u} + \mathbf{v}) &= \nabla \cdot \mathbf{u} + \nabla \cdot \mathbf{v} \\
\nabla \times (\mathbf{u} + \mathbf{v}) &= \nabla \times \mathbf{u} + \nabla \times \mathbf{v} \\
\nabla (\mathbf{u} \cdot \mathbf{v}) &= (\mathbf{u} \cdot \nabla) \mathbf{v} + (\mathbf{v} \cdot \nabla) \mathbf{u} + \mathbf{u} \times (\nabla \times \mathbf{v}) + \mathbf{v} \times (\nabla \times \mathbf{u}) \qquad \text{(A.1)} \\
\nabla \cdot (\mathbf{u} \times \mathbf{v}) &= \mathbf{v} \cdot \nabla \times \mathbf{u} - \mathbf{u} \cdot \nabla \times \mathbf{v} \\
\nabla \times (\mathbf{u} \times \mathbf{v}) &= \mathbf{u} (\nabla \cdot \mathbf{v}) - \mathbf{v} (\nabla \cdot \mathbf{u}) + (\mathbf{v} \cdot \nabla) \mathbf{u} - (\mathbf{u} \cdot \nabla) \mathbf{v} \\
\nabla \cdot (s\mathbf{v}) &= \mathbf{v} \cdot \nabla s + s \nabla \cdot \mathbf{v} \\
\nabla \times (s\mathbf{v}) &= s \nabla \times \mathbf{v} - \mathbf{v} \times \nabla s \\
\nabla (sa) &= s \nabla a + a \nabla s \\
\frac{1}{2} \nabla \left(\mathbf{v}^2 \right) &= \mathbf{v} \times (\nabla \times \mathbf{v}) + (\mathbf{v} \cdot \nabla) \mathbf{v}
\end{aligned}
$$

A.2 Acoustic Wave Equation Derivation

Shown below is a derivation of the acoustic wave equation following [48] or [49]. Start with the full continuity equation:

$$\frac{1}{\rho}\frac{D\rho}{Dt} + \nabla \cdot \mathbf{u} = q\left(\mathbf{r}, t\right) \tag{A.2}$$

And the momentum equation:

$$\frac{\partial\left(\rho\mathbf{u}\right)}{\partial t} + \left(\rho\mathbf{u}\right)\cdot\left(\nabla\mathbf{u}\right) + \mathbf{u}\nabla\cdot\left(\rho\mathbf{u}\right) = -\nabla p - \mu\nabla\times\omega + \left(\eta + \tfrac{4}{3}\mu\right)\nabla\left(\nabla\cdot\mathbf{u}\right) + \rho\mathbf{b} + \mathbf{F} \tag{A.3}$$

Linearize

$$\frac{1}{\rho_0}\frac{\partial\rho'}{\partial t} + \nabla\cdot\mathbf{u}' = q\left(\mathbf{r}, t\right) \tag{A.4}$$

$$\rho_0\frac{d\mathbf{u}'}{dt} + \nabla p' = \mathbf{F} \tag{A.5}$$

And apply the isentropic relation $\rho' = \frac{p'}{a^2}$ to A.4,

$$\frac{1}{\rho_0 a^2}\frac{\partial p'}{\partial t} + \nabla\cdot\mathbf{u}' = q\left(\mathbf{r}, t\right) \tag{A.6}$$

Take the divergence of A.5

$$\nabla\cdot\left\{\rho_0\frac{d\mathbf{u}'}{dt} + \nabla p' = \mathbf{F}\right\} = \rho_0\frac{d\left(\nabla\cdot\mathbf{u}'\right)}{dt} + \nabla^2 p' = \nabla\cdot\mathbf{F} \tag{A.7}$$

Multiply A.5 by $\rho_0\frac{\partial}{\partial t}$,

$$\rho_0\frac{\partial}{\partial t}\left\{\frac{1}{\rho_0 a^2}\frac{\partial p'}{\partial t} + \nabla\cdot\mathbf{u}' = q\left(\mathbf{r}, t\right)\right\} = \frac{1}{a^2}\frac{\partial^2 p'}{\partial t^2} + \rho_0\frac{\partial\left(\nabla\cdot\mathbf{u}'\right)}{\partial t} = \rho_0 q'\left(\mathbf{r}, t\right) \tag{A.8}$$

Combine A.8 and A.7 to obtain

$$\nabla^2 p' - \frac{1}{a^2}\frac{\partial^2 p'}{\partial t^2} = \nabla\cdot\mathbf{F} - \rho_0 q'\left(\mathbf{r}, t\right) \tag{A.9}$$

A.3 Leading and First Order Energy

A.3.1 Leading Order Energy

Follow Jacob [42] and start with the leading order energy.

$$\nabla \cdot (\mathbf{m}_0 H_0) - \mathbf{m}_0 \cdot \boldsymbol{\psi}_0 - T_0 Q_0 = 0 \tag{A.10}$$

Expanding the divergence term and rearranging.

$$H_0 \nabla \cdot \mathbf{m}_0 + \mathbf{m}_0 \cdot (\nabla H_0 - \boldsymbol{\psi}_0) - T_0 Q_0 = 0 \tag{A.11}$$

Insert the leading order relations 3.27 through 3.29 into equation A.10.

$$\mathbf{m}_0 \cdot \mathbf{L}_0 = \mathbf{m}_0 \cdot (\boldsymbol{\zeta}_0 + \nabla H_0 - T_0 \nabla s_0) \tag{A.12}$$

Solve for $\mathbf{m}_0 \cdot \nabla H_0$:

$$\mathbf{m}_0 \cdot \nabla H_0 = \mathbf{m}_0 \cdot \mathbf{L}_0 - \mathbf{m}_0 \cdot \boldsymbol{\zeta}_0 + \mathbf{m}_0 \cdot T_0 \nabla s_0 \tag{A.13}$$

Insert into A.11.

$$H_0 \nabla \cdot \mathbf{m}_0 - \mathbf{m}_0 \cdot \boldsymbol{\psi}_0 - T_0 Q_0 + \mathbf{m}_0 \cdot \mathbf{L}_0 - \mathbf{m}_0 \cdot \boldsymbol{\zeta}_0 + \mathbf{m}_0 \cdot T_0 \nabla s_0 = 0 \tag{A.14}$$

Find that:

$$\mathbf{m}_0 \cdot \boldsymbol{\zeta}_0 = \rho_0 \mathbf{u}_0 \cdot (\boldsymbol{\omega}_0 \times \mathbf{u}_0) = 0 \tag{A.15}$$

Therefore

$$H_0 \nabla \cdot \mathbf{m}_0 + \mathbf{m}_0 \cdot (\mathbf{L}_0 - \boldsymbol{\psi}_0) - T_0 Q_0 + \mathbf{m}_0 \cdot T_0 \nabla s_0 = 0 \tag{A.16}$$

Expand leading order entropy equation S_o and multiply by T_o.

$$S_0 = \nabla \cdot (\mathbf{m}_0 s_0) = s_0 \nabla \cdot \mathbf{m}_0 + \mathbf{m}_0 \cdot \nabla s_0$$
$$\mathbf{m}_0 \cdot \nabla s_0 = S_0 - s_0 \nabla \cdot \mathbf{m}_0$$
$$T_0 \mathbf{m}_0 \cdot \nabla s_0 = T_0 S_0 - T_0 s_0 \nabla \cdot \mathbf{m}_0 \tag{A.17}$$

Insert back into equation A.16.

$$H_0 \nabla \cdot \mathbf{m}_0 + \mathbf{m}_0 \cdot (\mathbf{L}_0 - \boldsymbol{\psi}_0) - T_0 Q_0 + T_0 S_0 - T_0 s_0 \nabla \cdot \mathbf{m}_0 = 0 \tag{A.18}$$

Collect the terms.

$$(H_0 - T_0 s_0) \nabla \cdot \mathbf{m}_0 + \mathbf{m}_0 \cdot (\mathbf{L}_0 - \boldsymbol{\psi}_0) + T_0 (S_0 - Q_0) = 0 \tag{A.19}$$

Insert the base order continuity equation, $\nabla \cdot \mathbf{m}_0 = C_0$

$$(H_0 - T_0 s_0) C_0 + \mathbf{m}_0 \cdot (\mathbf{L}_0 - \boldsymbol{\psi}_0) + T_0 (S_0 - Q_0) = 0 \tag{A.20}$$

Because of equations 3.39 through 3.41 equation A.20 reduces to:

$$0 = 0 \tag{A.21}$$

A.3.2 First Order Energy

Follow Jacob [42] and start with the first order energy:

$$\frac{\partial}{\partial t}(\rho H - p)_1 + \nabla \cdot (\mathbf{m}_0 H_1 + \mathbf{m}_1 H_0) - \mathbf{m}_0 \cdot \boldsymbol{\psi}_1 - \mathbf{m}_1 \cdot \boldsymbol{\psi}_0 - T_0 Q_1 - T_1 Q_0 = 0 \tag{A.22}$$

Working with the time derivative term. Insert the definition of the total enthalpy and expand:

$$
\begin{aligned}
(\rho H - p)_1 &= \left(\rho\left(h + \frac{1}{2}\mathbf{u}^2\right) - p\right)_1 \\
&= \left(\rho\left(e + \frac{p}{\rho} + \frac{1}{2}\mathbf{u}^2\right) - p\right)_1 \\
&= \left(\rho e + \frac{1}{2}\rho\mathbf{u}^2\right)_1 \\
&= (\rho e)_1 + \frac{1}{2}\rho_1 {u_0}^2 + \rho_0\mathbf{u}_0 \cdot \mathbf{u}_1 \\
&= h_0\rho_1 + \rho_0 T_0 s_1 + \frac{1}{2}\rho_1 {u_0}^2 + \rho_0\mathbf{u}_0 \cdot \mathbf{u}_1 \\
(\rho H - p)_1 &= \rho_1 H_0 + \rho_0 T_0 s_1 + \rho_0\mathbf{u}_0 \cdot \mathbf{u}_1
\end{aligned}
\tag{A.23}
$$

Substitute back:

$$
\begin{aligned}
&\frac{\partial}{\partial t}\left(\rho_1 H_0 + \rho_0 T_0 s_1 + \rho_0\mathbf{u}_0 \cdot \mathbf{u}_1\right) + \nabla \cdot \left(\mathbf{m}_0 H_1 + \mathbf{m}_1 H_0\right) \\
&\qquad\qquad - \mathbf{m}_0 \cdot \boldsymbol{\psi}_1 - \mathbf{m}_1 \cdot \boldsymbol{\psi}_0 - T_0 Q_1 - T_1 Q_0 = 0
\end{aligned}
\tag{A.24}
$$

Leaving out detail that can be found in [42], but taking care of vorticity terms:

$$
\begin{aligned}
\mathbf{m}_1 &= \rho_0\mathbf{u}_1 + \rho_1\mathbf{u}_0 \\
\boldsymbol{\zeta}_1 &= \boldsymbol{\omega}_0 \times \mathbf{u}_1 + \boldsymbol{\omega}_1 \times \mathbf{u}_0
\end{aligned}
\tag{A.25}
$$

Therefore:

$$
\begin{aligned}
\mathbf{m}_1 \cdot \boldsymbol{\zeta}_0 + \mathbf{m}_0 \cdot \boldsymbol{\zeta}_1 &= (\rho_0\mathbf{u}_1 + \rho_1\mathbf{u}_0) \cdot (\boldsymbol{\omega}_0 \times \mathbf{u}_0) \\
&\quad + \rho_0\mathbf{u}_0 \cdot (\boldsymbol{\omega}_0 \times \mathbf{u}_1 + \boldsymbol{\omega}_1 \times \mathbf{u}_0) \\
&= \rho_0\mathbf{u}_1 \cdot (\boldsymbol{\omega}_0 \times \mathbf{u}_0) + \rho_1\mathbf{u}_0 \cdot (\boldsymbol{\omega}_0 \times \mathbf{u}_0) \\
&\quad + \rho_0\mathbf{u}_0 \cdot (\boldsymbol{\omega}_0 \times \mathbf{u}_1) + \rho_0\mathbf{u}_0 \cdot (\boldsymbol{\omega}_1 \times \mathbf{u}_0)
\end{aligned}
\tag{A.26}
$$

$$\begin{aligned}\rho_1 \mathbf{u}_0 \cdot (\boldsymbol{\omega}_0 \times \mathbf{u}_0) = 0 \\ \rho_0 \mathbf{u}_0 \cdot (\boldsymbol{\omega}_1 \times \mathbf{u}_0) = 0\end{aligned} \tag{A.27}$$

Using triple product rules this yields:

$$\mathbf{m}_1 \cdot \boldsymbol{\zeta}_0 + \mathbf{m}_0 \cdot \boldsymbol{\zeta}_1 = \rho_0 \mathbf{u}_1 \cdot (\boldsymbol{\omega}_0 \times \mathbf{u}_0) + \rho_0 \mathbf{u}_0 \cdot (\boldsymbol{\omega}_0 \times \mathbf{u}_1) = 0 \tag{A.28}$$

Regardless of entropy or vorticity fluctuations the energy equation for the first order reduces to zero.

$$(H_0 - T_0 s_0)\, C_1 + \mathrm{T}_0(\mathrm{S}_1 - Q_1) + \mathbf{m}_0 \cdot (\mathbf{L}_1 - \boldsymbol{\psi}_1) = 0 \tag{A.29}$$

A.4 Solutions to the stream function amplitude ϕ

$$\phi''_i - k_m^2 \phi_i = \left(\frac{R_m a_0 \sin[i[x]]}{\gamma k_m} \right) \left(\frac{k_m U_0''}{\omega_m + U_0 k_m} \right) \tag{A.30}$$

$$\phi''_r - k_m^2 \phi_r = -\left(\frac{R_m a_0 \cos[i[x]]}{\gamma} \right) \left(\frac{k_m U_0'}{\omega_m + U_0 k_m} \right) \tag{A.31}$$

Define:

$$\begin{aligned} M_0 F_1[y] = \left(\frac{k_m U_0''}{\omega_m + U_0 k_m} \right) = \frac{U_0''}{a_0 + U_0} = \\ -\frac{W_0}{\theta^2} \left[\frac{\operatorname{sech}^2\left[\frac{y}{\theta}\right] \tanh\left[\frac{y}{\theta}\right]}{a_0 + \frac{W_0}{2}\left(1 + \tanh\left[\frac{y}{\theta}\right]\right)} \right] = -\frac{M_0}{\theta^2} \left[\frac{\operatorname{sech}^2\left[\frac{y}{\theta}\right] \tanh\left[\frac{y}{\theta}\right]}{1 + \frac{M_0}{2}\left(1 + \tanh\left[\frac{y}{\theta}\right]\right)} \right] \\ \approx -\frac{M_0}{\theta^2} \operatorname{sech}^2\left[\frac{y}{\theta}\right] \tanh\left[\frac{y}{\theta}\right] + O[M_0{}^2] \end{aligned} \tag{A.32}$$

$$\begin{aligned} M_0 F_2[y] = \left(\frac{k_m U_0'}{\omega_m + U_0 k_m} \right) = \frac{U_0'}{a_0 + U_0} = \\ \frac{W_0}{2\theta} \left[\frac{\operatorname{sech}^2\left[\frac{y}{\theta}\right]}{a_0 + \frac{W_0}{2}\left(1 + \tanh\left[\frac{y}{\theta}\right]\right)} \right] = \frac{M_0}{2\theta} \left[\frac{\operatorname{sech}^2\left[\frac{y}{\theta}\right]}{1 + \frac{M_0}{2}\left(1 + \tanh\left[\frac{y}{\theta}\right]\right)} \right] \\ \approx \frac{M_0}{2\theta} \operatorname{sech}^2\left[\frac{y}{\theta}\right] + O[M_0{}^2] \end{aligned} \tag{A.33}$$

$$G_1 = \frac{R_m a_0 \sin[i[x]]}{\gamma k_m} \tag{A.34}$$

$$G_2 = \frac{R_m a_0 \cos[i[x]]}{\gamma} \tag{A.35}$$

Equations A.30 and A.31 become:

$$\phi_i'' - k_m^2 \phi_i = M_0 G_1 F_1 \tag{A.36}$$

$$\phi_r'' - k_m^2 \phi_r = M_0 G_2 F_2 \tag{A.37}$$

Equations A.36 and A.37 are of the form:

$$z(1-z)\,y'' + [c - (a+b+1)\,z]\,y' - aby = 0 \tag{A.38}$$

Solutions to equation A.38 are Gaussian hypergeometric functions:

$$y = A_2F_1[a,b;c;z] + B_2F_1[a+1-c, b+1-c; 2-c; z] \tag{A.39}$$

In particular solutions to A.36 and A.37 are:

$$\phi_i = \frac{M_0G_1}{4\left(k_m^2-4\right)}\left\{\begin{array}{l} e^{2y}k_m\left(k_m+2\right){}_2F_1\left[\left(1-\frac{1}{2}k_m\right),1;\left(2-\frac{1}{2}k_m\right);-e^{2y}\right] \\ +e^{2y}k_m\left(k_m-2\right){}_2F_1\left[\left(1+\frac{1}{2}k_m\right),1;\left(2+\frac{1}{2}k_m\right);-e^{2y}\right] \\ -\left(k_m^2-4\right){}_2F_1\left[\left(-\frac{1}{2}k_m\right),1;\left(1-\frac{1}{2}k_m\right);-e^{2y}\right] \\ -\left(k_m^2-4\right){}_2F_1\left[\left(\frac{1}{2}k_m\right),1;\left(1+\frac{1}{2}k_m\right);-e^{2y}\right] \\ -2\left(k_m^2-4\right)\tanh[y] \end{array}\right\} \tag{A.40}$$

$$\phi_i = \frac{M_0G_1}{4\left(k_m^2-4\right)}\{\star_1\} \tag{A.41}$$

$$\phi_r = \frac{M_0G_2}{2k_m\left(k_m^2-4\right)}\left\{\begin{array}{l} e^{2y}k_m\left(k_m+2\right){}_2F_1\left[\left(1-\frac{1}{2}k_m\right),1;\left(2-\frac{1}{2}k_m\right);-e^{2y}\right] \\ -e^{2y}k_m\left(k_m-2\right){}_2F_1\left[\left(1+\frac{1}{2}k_m\right),1;\left(2+\frac{1}{2}k_m\right);-e^{2y}\right] \\ -\left(k_m^2-4\right){}_2F_1\left[\left(-\frac{1}{2}k_m\right),1;\left(1-\frac{1}{2}k_m\right);-e^{2y}\right] \\ +\left(k_m^2-4\right){}_2F_1\left[\left(\frac{1}{2}k_m\right),1;\left(1+\frac{1}{2}k_m\right);-e^{2y}\right] \end{array}\right\} \tag{A.42}$$

$$\phi_r = \frac{M_0G_2}{2k_m\left(k_m^2-4\right)}\{\star_2\} \tag{A.43}$$

Remember:

$$\phi[y] = \phi_r + i\phi_i \tag{A.44}$$

$$\Psi = \phi \exp[i\omega_m t] \exp[ik_m (Z_0 + x)] \tag{A.45}$$

The components of the unsteady rotational velocity $\tilde{\mathbf{u}}_1$ could be calculated from the following expressions:

$$\begin{aligned}
\tilde{u}_1 = \frac{\partial \Psi}{\partial y} &= \left(\frac{\partial \phi_r}{\partial y} + i\frac{\partial \phi_i}{\partial y} \right) \exp[i\omega_m t] \exp[ik_m (Z_0 + x)] \\
&= M_0 \begin{pmatrix} \dfrac{G_2}{2k_m (k_m^2 - 4)} \dfrac{\partial \{\star_2\}}{\partial y} \\ +i\dfrac{G_1}{4(k_m^2 - 4)} \dfrac{\partial \{\star_1\}}{\partial y} \end{pmatrix} \exp[i\omega_m t] \exp[ik_m (Z_0 + x)]
\end{aligned} \tag{A.46}$$

$$\begin{aligned}
\tilde{v}_1 = -\frac{\partial \Psi}{\partial x} &= -\left\{ ik_m (\phi_r + i\phi_i) + \left(\frac{\partial \phi_r}{\partial x} + i\frac{\partial \phi_i}{\partial x} \right) \right\} \exp[i\omega_m t] \exp[ik_m (Z_0 + x)] \\
&= -\left\{ \begin{array}{l} ik_m \left(\dfrac{M_0 G_2}{2k_m (k_m^2 - 4)} \{\star_2\} + i\dfrac{M_0 G_1}{4(k_m^2 - 4)} \{\star_1\} \right) \\ + \left(\dfrac{M_0}{2k_m (k_m^2 - 4)} \dfrac{\partial G_2}{\partial x} \{\star_2\} + i\dfrac{M_0}{4(k_m^2 - 4)} \dfrac{\partial G_1}{\partial x} \{\star_1\} \right) \end{array} \right\} \exp[i\omega_m t] \exp[ik_m (Z_0 + x)] \\
&= -M_0 \left\{ \begin{array}{l} \dfrac{1}{2k_m (k_m^2 - 4)} \{\star_2\} \left(ik_m G_2 + \dfrac{\partial G_2}{\partial x} \right) \\ + \dfrac{1}{4(k_m^2 - 4)} \{\star_1\} \left(-k_m G_1 + i\dfrac{\partial G_1}{\partial x} \right) \end{array} \right\} \exp[i\omega_m t] \exp[ik_m (Z_0 + x)]
\end{aligned} \tag{A.47}$$

The important finding is that $\tilde{u}_1$ and $\tilde{v}_1$ are of the order M_0!

A.5 Details of the Integration over the Volume

Recall:

$$i[x] = \frac{\pi}{2}\left(1 - \frac{x}{d}\right)\left(1 - \frac{R_0}{R}\right) \tag{A.48}$$

Also already know that:

$$\theta, d \ll R, R_0, Z_0, L \tag{A.49}$$

Furthermore θ and d are much smaller than unity as well, therefore:

$$\theta, d \ll 1 \tag{A.50}$$

$$\sin[2k_m d] \approx 2k_m d \tag{A.51}$$

$$\cos[2k_m d] \approx 1 \tag{A.52}$$

Integrate over equation 5.100 with respect to x:

$$\int_0^d \frac{1}{4\gamma} \sin[2i[x]] \sin[2k_m (Z_0 + x)] dx =$$

$$\frac{1}{4\gamma}\left[\begin{array}{l} \frac{d}{2} R \frac{\sin\left[\frac{d\pi R_0 - 2k_m dRx + \pi Rx - \pi R_0 x - 2k_m dRZ_0}{dR}\right]}{-2k_m dR + \pi (R - R_0)} \\ -\frac{d}{2} R \frac{\sin\left[\frac{d\pi R_0 + 2k_m dRx + \pi Rx - \pi R_0 x + 2k_m dRZ_0}{dR}\right]}{2k_m dR + \pi (R - R_0)} \end{array}\right]_0^d \tag{A.53}$$

Now apply equation A.49:

$$\int_0^d \frac{1}{4\gamma} \sin[2i[x]] \sin[2k_m (Z_0 + x)] dx \approx$$

$$\frac{1}{4\gamma}\left[\begin{array}{l} \frac{d}{2} R \frac{\sin\left[\frac{d\pi R_0 - 2k_m dRx + \pi Rx - \pi R_0 x - 2k_m dRZ_0}{dR}\right]}{\pi (R - R_0)} \\ -\frac{d}{2} R \frac{\sin\left[\frac{d\pi R_0 + 2k_m dRx + \pi Rx - \pi R_0 x + 2k_m dRZ_0}{dR}\right]}{\pi (R - R_0)} \end{array}\right]_0^d \tag{A.54}$$

Equation A.54 can be simplified:

$$\int_0^d \frac{1}{4\gamma}\sin[2i[x]]\sin[2k_m(Z_0+x)]dx =$$

$$\frac{1}{4\gamma}\left[-dR\frac{\cos\left[\pi\left(dR_0+(R-R_0)x\right)\right]\sin\left[2k_m(Z_0+x)\right]}{\pi(R-R_0)}\right]_0^d \tag{A.55}$$

Apply the limits of the integration:

$$\int_0^d \frac{1}{4\gamma}\sin[2i[x]]\sin[2k_m(Z_0+x)]dx = \frac{1}{4\gamma}\left[\frac{dR\sin\left[2k_mZ_0\right]}{\pi(R-R_0)}\right]-\left[-\frac{dR\cos\left[\pi\frac{R_0}{R}\right]\sin\left[2k_mZ_0\right]}{\pi(R-R_0)}\right] \tag{A.56}$$

$$= \frac{1}{4\gamma}d\sin\left[2k_mZ_0\right]\left[\frac{1}{\pi\left(1-{R_0}/{R}\right)}\right]\left(1+\cos\left[\pi{R_0}/{R}\right]\right) \tag{A.57}$$

Integrate over equation 5.101 with respect to x:

$$\int_0^d -\frac{1}{\gamma k_m}\sin^2[i[x]]\sin^2[k_m(Z_0+x)]dx =$$

$$-\frac{1}{\gamma k_m}\frac{1}{8}\left[\begin{array}{l} 2d-\dfrac{\cos[2k_mZ_0]\sin[2k_md]}{k_m}-2d\dfrac{R\sin\left[\pi{R_0}/{R}\right]}{\pi(R-R_0)} \\ +\dfrac{\sin[2k_mZ_0]}{k_m}-\dfrac{\cos[2k_md]\sin[2k_mZ_0]}{k_m} \\ +d\dfrac{R\sin[2k_m(d+Z_0)]}{2dk_mR+\pi(R-R_0)}+d\dfrac{R\sin[2k_m(d+Z_0)]}{2dk_mR-\pi(R-R_0)} \\ +d\dfrac{R\sin\left[\pi{R_0}/{R}-2k_mZ_0\right]}{-2dk_mR+\pi(R-R_0)}+d\dfrac{R\sin\left[\pi{R_0}/{R}+2k_mZ_0\right]}{2dk_mR-\pi(R-R_0)} \end{array}\right] \tag{A.58}$$

Applying equation A.49 yields:

$$
\begin{aligned}
&\int_0^d -\frac{1}{\gamma k_m}\sin^2[i[x]]\sin^2[k_m(Z_0+x)]dx = \\
&-\frac{1}{\gamma k_m}\frac{1}{8}\left[\begin{array}{l}
2d-\frac{\cos[2k_mZ_0]\sin[2k_md]}{k_m}-2d\frac{R\sin\left[\pi^{R_0}/_R\right]}{\pi(R-R_0)} \\
+\frac{\sin[2k_mZ_0]}{k_m}-\frac{\cos[2k_md]\sin[2k_mZ_0]}{k_m} \\
+d\frac{R\sin[2k_mZ_0]}{\pi(R-R_0)}-d\frac{R\sin[2k_mZ_0]}{\pi(R-R_0)} \\
+d\frac{R\sin\left[\pi^{R_0}/_R-2k_mZ_0\right]}{\pi(R-R_0)}-d\frac{R\sin\left[\pi^{R_0}/_R+2k_mZ_0\right]}{\pi(R-R_0)}
\end{array}\right]
\end{aligned}
\tag{A.59}
$$

Then applying equations A.51 and A.52 results in:

$$
\begin{aligned}
&\int_0^d -\frac{1}{\gamma k_m}\sin^2[i[x]]\sin^2[k_m(Z_0+x)]dx = \\
&-\frac{1}{\gamma k_m}\frac{1}{8}\left[\begin{array}{l}
2d-2d\cos[2k_mZ_0]-2d\frac{R\sin\left[\pi^{R_0}/_R\right]}{\pi(R-R_0)} \\
+\frac{\sin[2k_mZ_0]}{k_m}-\frac{\sin[2k_mZ_0]}{k_m} \\
+d\frac{R\sin[2k_mZ_0]}{\pi(R-R_0)}-d\frac{R\sin[2k_mZ_0]}{\pi(R-R_0)} \\
+d\frac{R\sin\left[\pi^{R_0}/_R-2k_mZ_0\right]}{\pi(R-R_0)}-d\frac{R\sin\left[\pi^{R_0}/_R+2k_mZ_0\right]}{\pi(R-R_0)}
\end{array}\right]
\end{aligned}
\tag{A.60}
$$

Cancel terms:

$$\int_0^d -\frac{1}{\gamma k_m}\sin^2[i[x]]\sin^2[k_m(Z_0+x)]dx =$$

$$-\frac{1}{\gamma k_m}\frac{1}{8}\begin{bmatrix} 2d-2d\cos[2k_m Z_0]-2d\dfrac{R\sin\left[\pi^{R_0}\!/_R\right]}{\pi(R-R_0)} \\ +d\dfrac{R\sin\left[\pi^{R_0}\!/_R-2k_m Z_0\right]}{\pi(R-R_0)}-d\dfrac{R\sin\left[\pi^{R_0}\!/_R+2k_m Z_0\right]}{\pi(R-R_0)}\end{bmatrix} \tag{A.61}$$

Simplify:

$$\int_0^d -\frac{1}{\gamma k_m}\sin^2[i[x]]\sin^2[k_m(Z_0+x)]dx =$$

$$-\frac{1}{\gamma k_m}\frac{1}{8}\begin{bmatrix} 2d-2d\cos[2k_m Z_0]-2d\dfrac{R\sin\left[\pi^{R_0}\!/_R\right]}{\pi(R-R_0)} \\ +2d\dfrac{\cos[2k_m Z_0]}{\pi\left(1-{}^{R_0}\!/_R\right)}\sin\left[\pi^{R_0}\!/_R\right]\end{bmatrix} \tag{A.62}$$

And rearrange:

$$\int_0^d -\frac{1}{\gamma k_m}\sin^2[i[x]]\sin^2[k_m(Z_0+x)]dx =$$

$$-\frac{1}{\gamma k_m}\frac{1}{4}d\left(1-\cos[2k_m Z_0]\right)\left(1-\frac{\sin\left[\pi^{R_0}\!/_R\right]}{\pi\left(1-{}^{R_0}\!/_R\right)}\right) \tag{A.63}$$

Appendix B

B.1 Experimental Data

B.1.1 Baffle with $R_0/R = 0.82$

Figure B.1 displays a 3-D surface plot of the sound pressure level as a function of the position Z_0/L and the oscillation frequency f_m. Figure B.2 shows a contour plot of spectral data, figure B.3 shows a contour plot of spectral data and contour lines of the theoretical growth rate α_{VS}. The dashed orange lines correspond to the (longitudinal) harmonics of the test chamber (multiples of 75Hz).

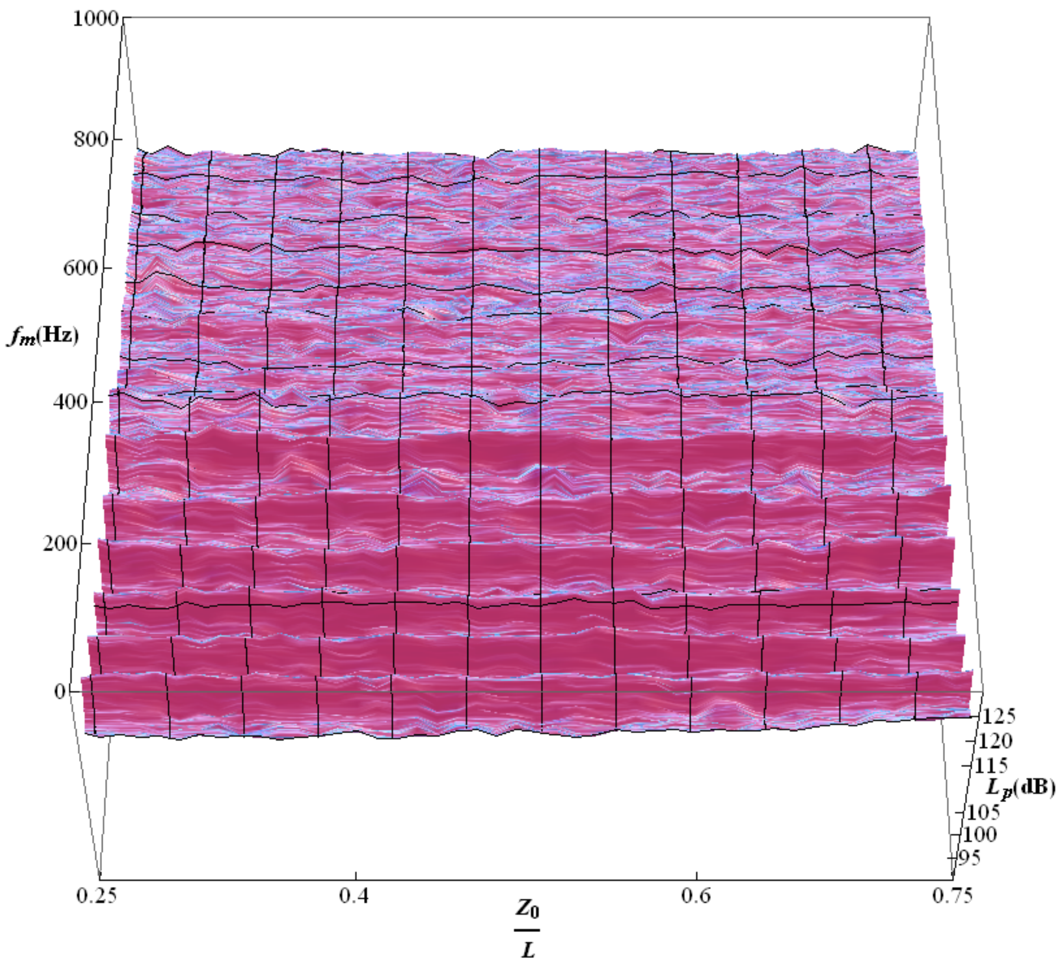

Figure B.1: 3-D Surface Plot of Spectral Data, $R_0/R = 0.82$

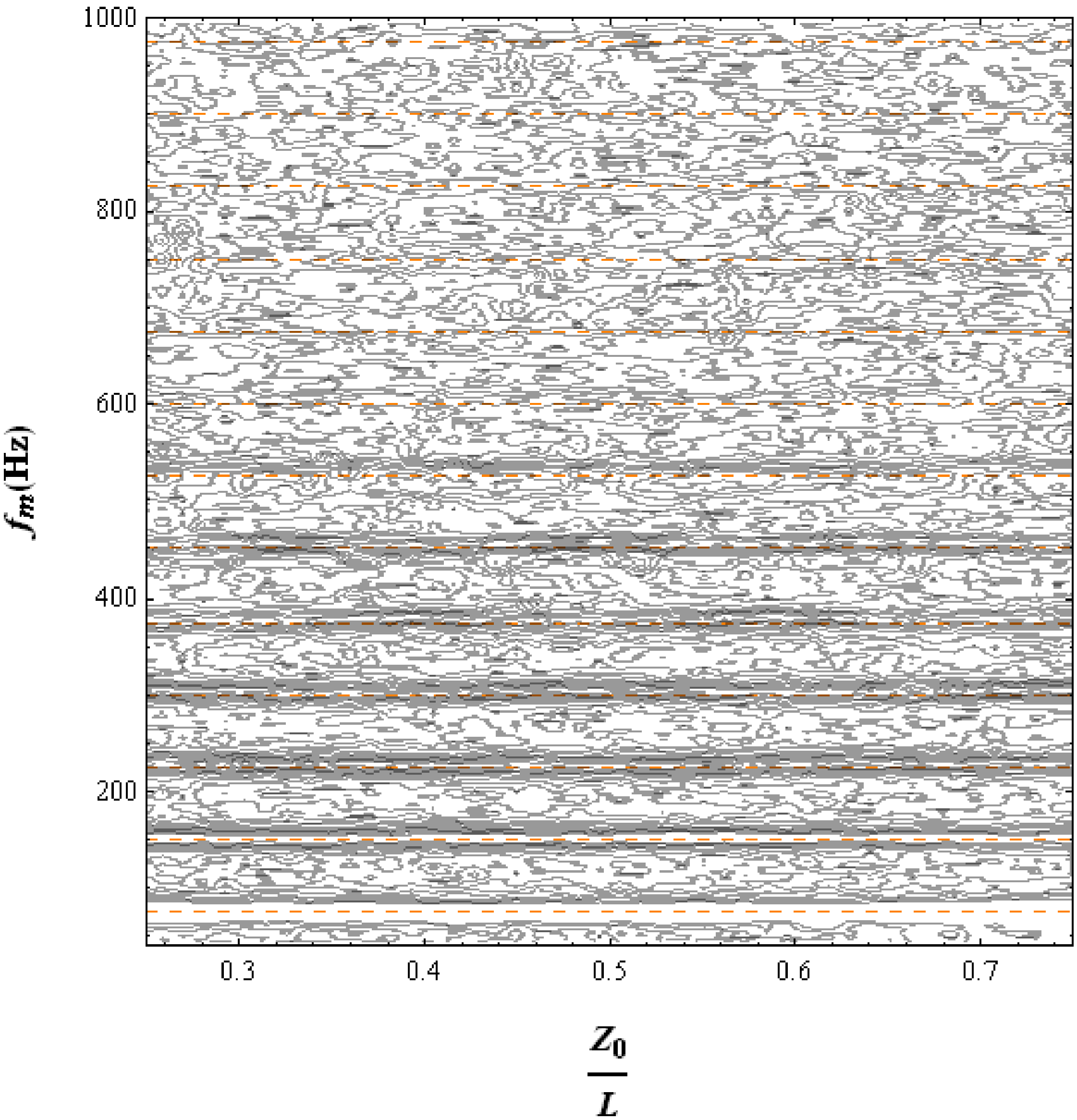

Figure B.2: Contour Plot of Spectral Data, $R_0/R = 0.82$

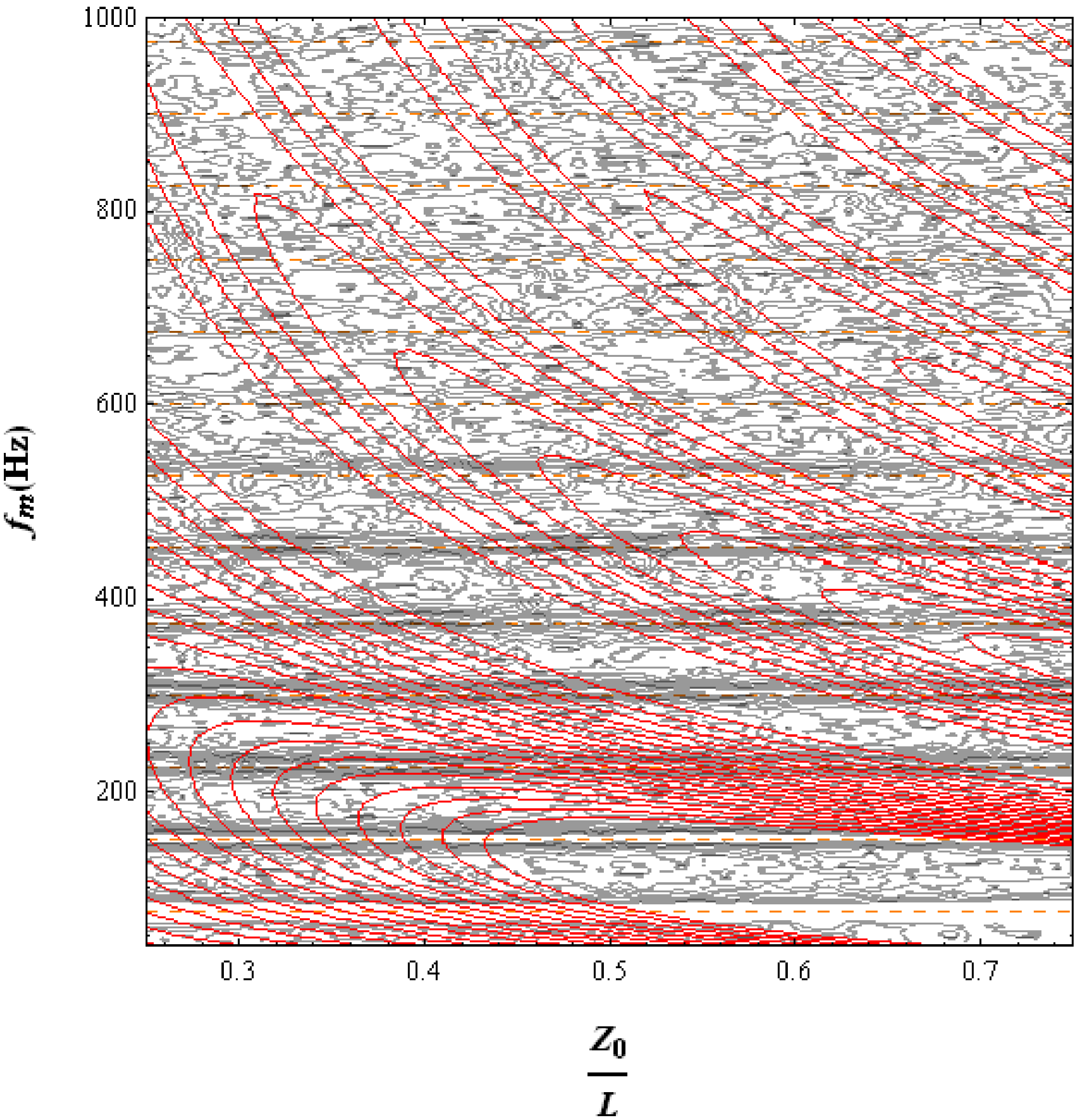

Figure B.3: Contour Plot of Spectral Data (black) and Contour Lines of α_{VS} (red), $R_0/R = 0.82$

B.1.2 Baffle with $R_0/R = 0.75$

Figure B.4 displays a 3-D surface plot of the sound pressure level as a function of the position Z_0/L and the oscillation frequency f_m. Figure B.5 shows a contour plot of spectral data, figure B.6 shows a contour plot of spectral data and contour lines of the theoretical growth rate α_{VS}. The dashed orange lines correspond to the (longitudinal) harmonics of the test chamber (multiples of 75Hz).

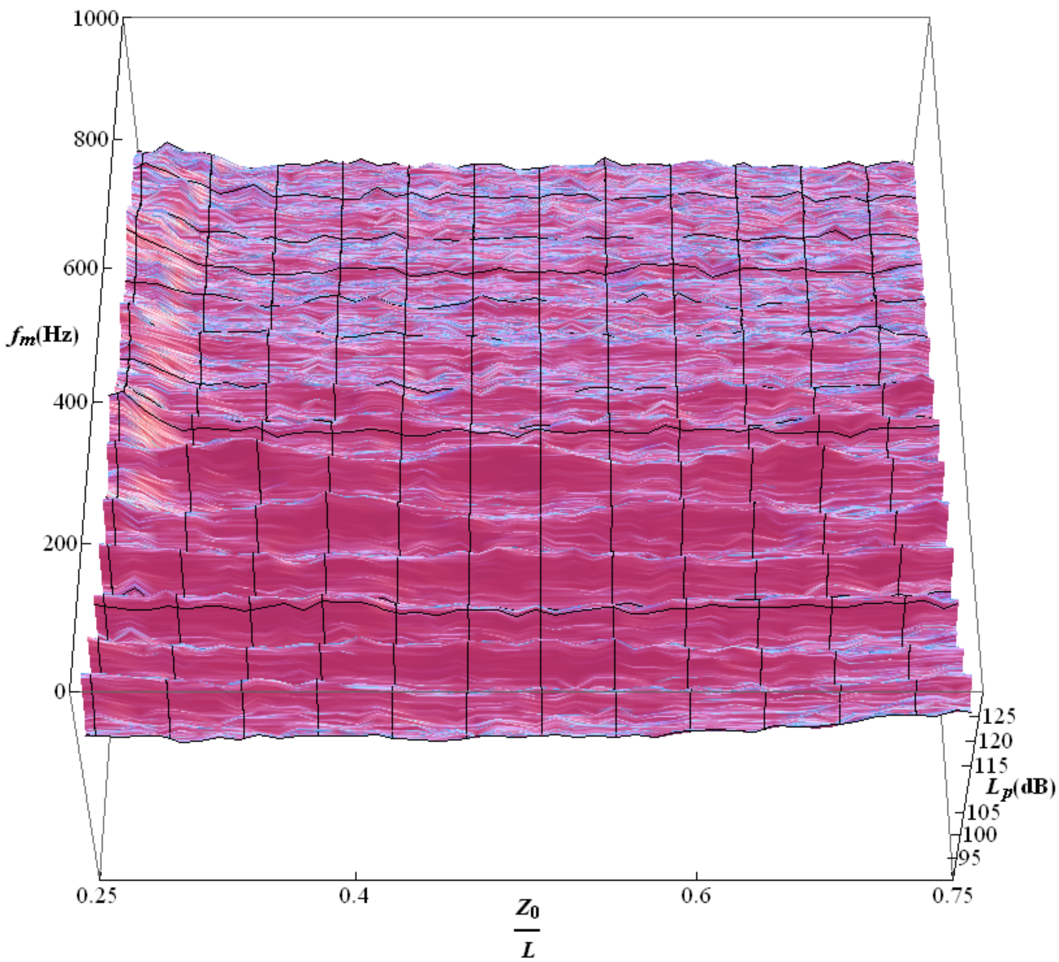

Figure B.4: 3-D Surface Plot of Spectral Data, $R_0/R = 0.75$

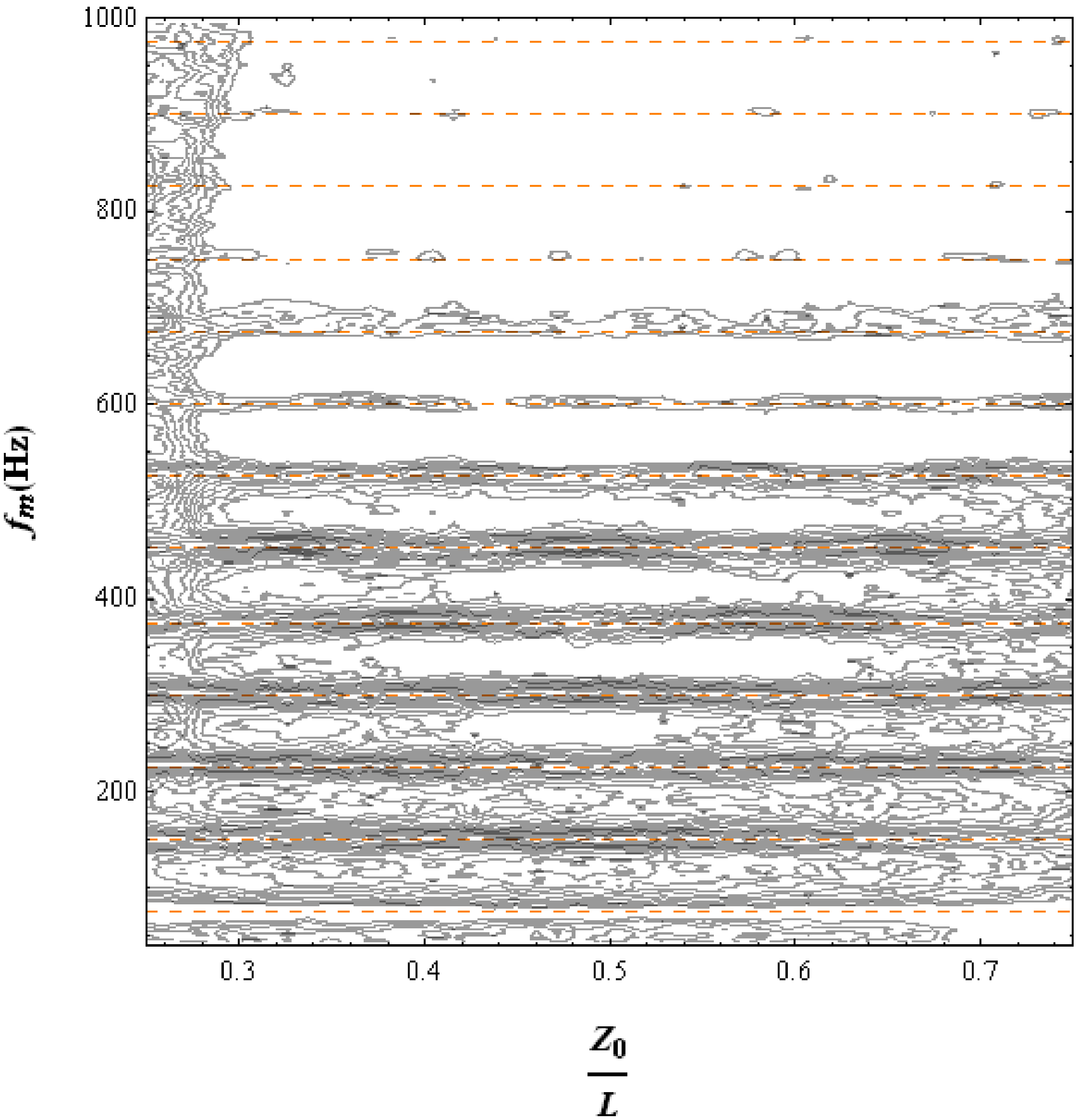

Figure B.5: Contour Plot of Spectral Data, $R_0/R = 0.75$

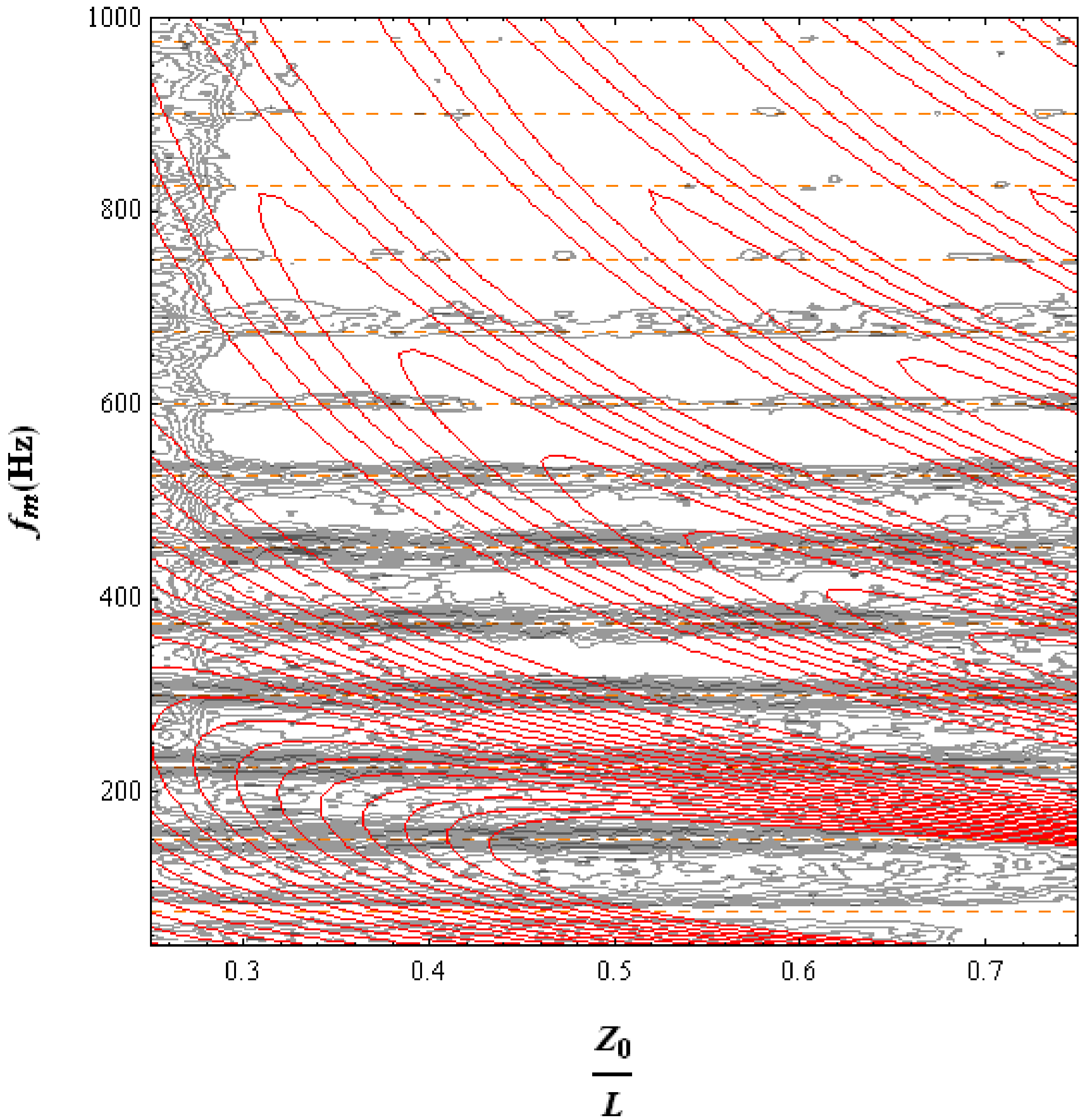

Figure B.6: Contour Plot of Spectral Data (black) and Contour Lines of α_{VS} (red), $R_0/R = 0.75$

B.1.3 Baffle with $R_0/R = 0.70$

Figure B.7 displays a 3-D surface plot of the sound pressure level as a function of the position Z_0/L and the oscillation frequency f_m. Figure B.8 shows a contour plot of spectral data, figure B.9 shows a contour plot of spectral data and contour lines of the theoretical growth rate α_{VS}. The dashed orange lines correspond to the (longitudinal) harmonics of the test chamber (multiples of 75Hz).

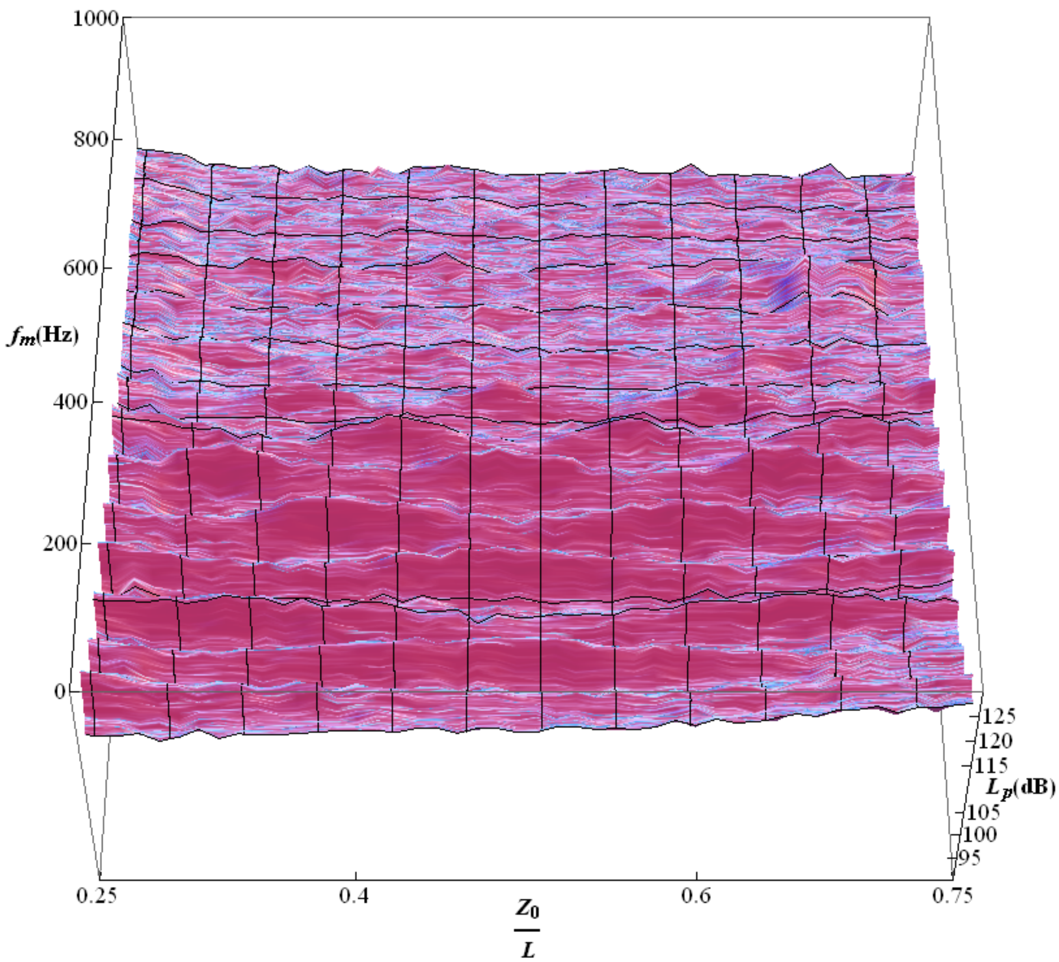

Figure B.7: 3-D Surface Plot of Spectral Data, $R_0/R = 0.70$

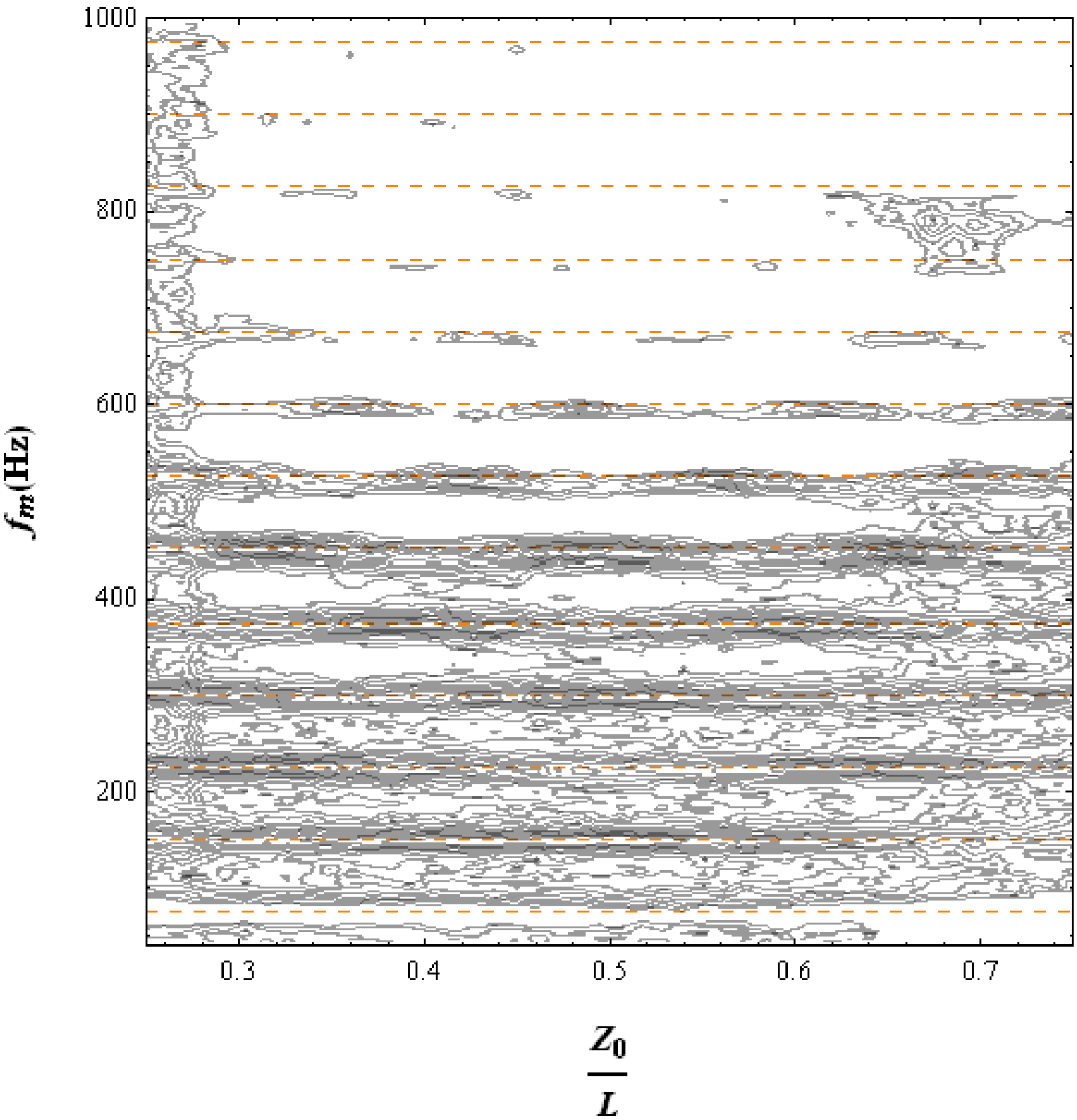

Figure B.8: Contour Plot of Spectral Data, $R_0/R = 0.70$

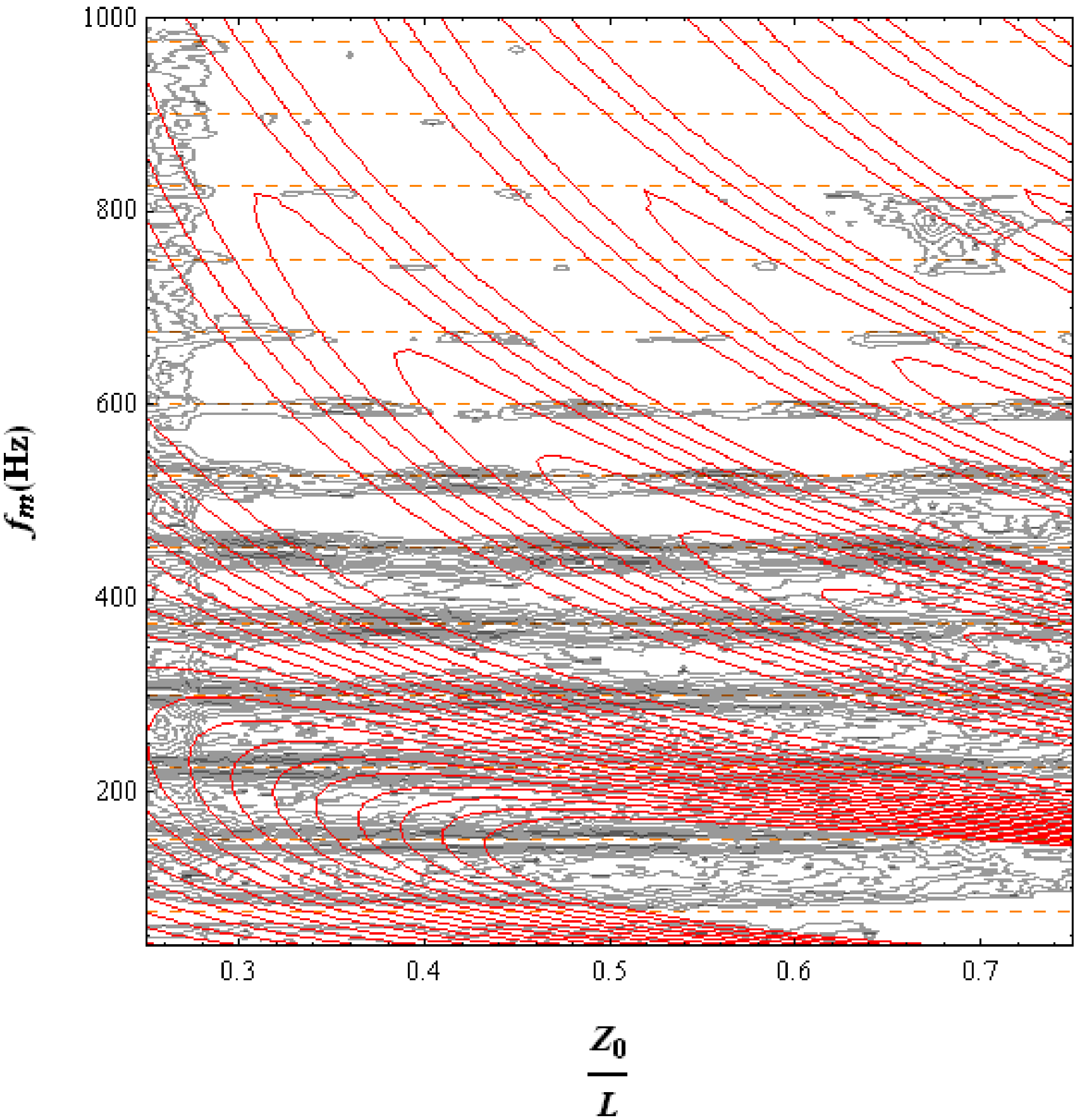

Figure B.9: Contour Plot of Spectral Data (black) and Contour Lines of α_{VS} (red), $R_0/R = 0.70$

B.1.4 Baffle with $R_0/R = 0.65$

Figure B.10 displays a 3-D surface plot of the sound pressure level as a function of the position Z_0/L and the oscillation frequency f_m. Figure B.11 shows a contour plot of spectral data, figure B.12 shows a contour plot of spectral data and contour lines of the theoretical growth rate α_{VS}. The dashed orange lines correspond to the (longitudinal) harmonics of the test chamber (multiples of 75Hz).

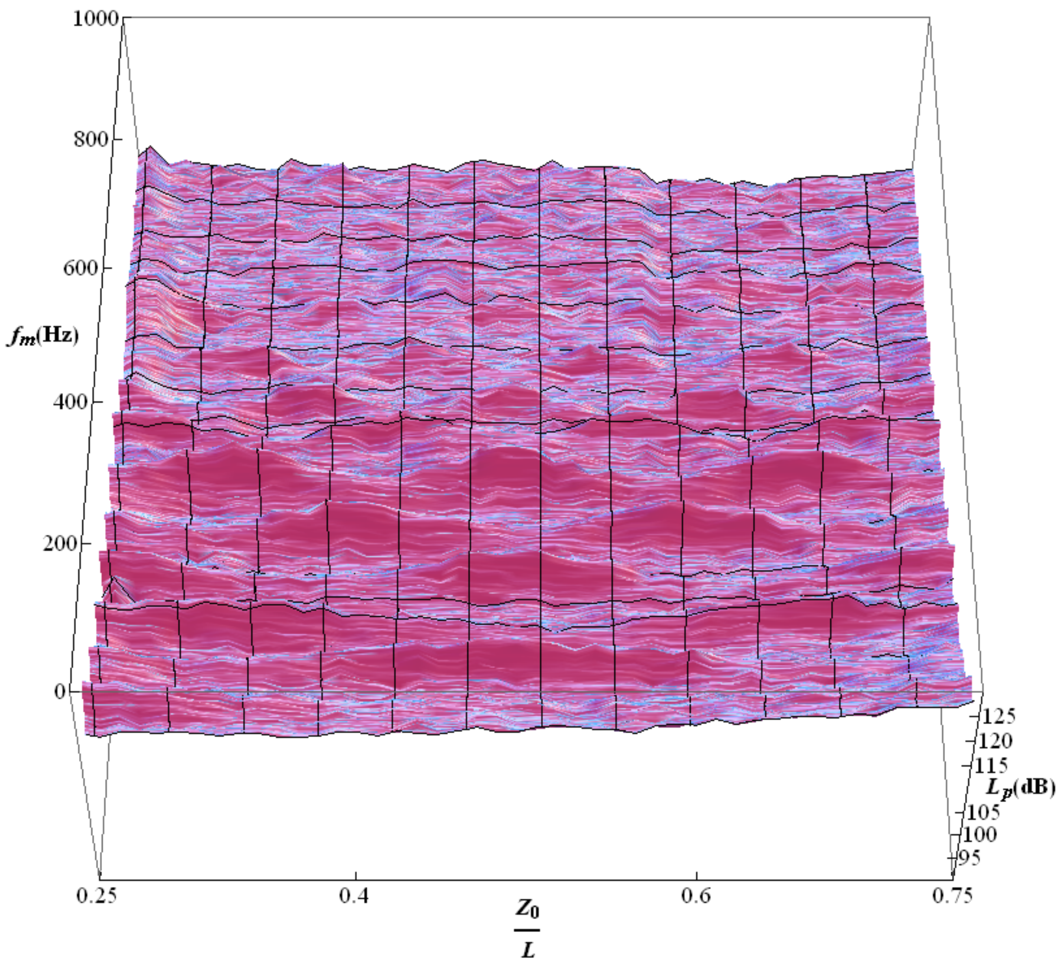

Figure B.10: 3-D Surface Plot of Spectral Data, $R_0/R = 0.65$

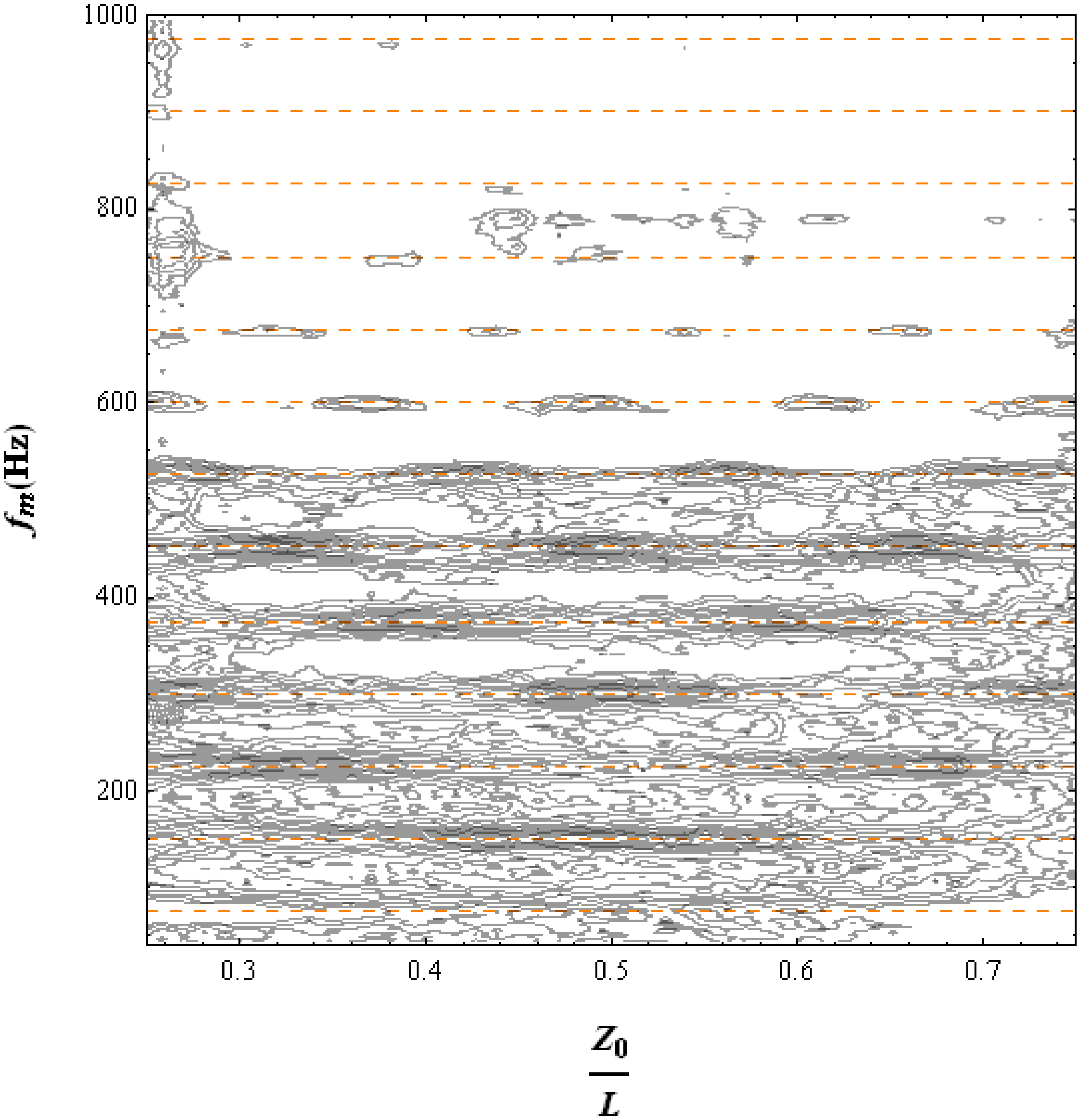

Figure B.11: Contour Plot of Spectral Data, $R_0/R = 0.65$

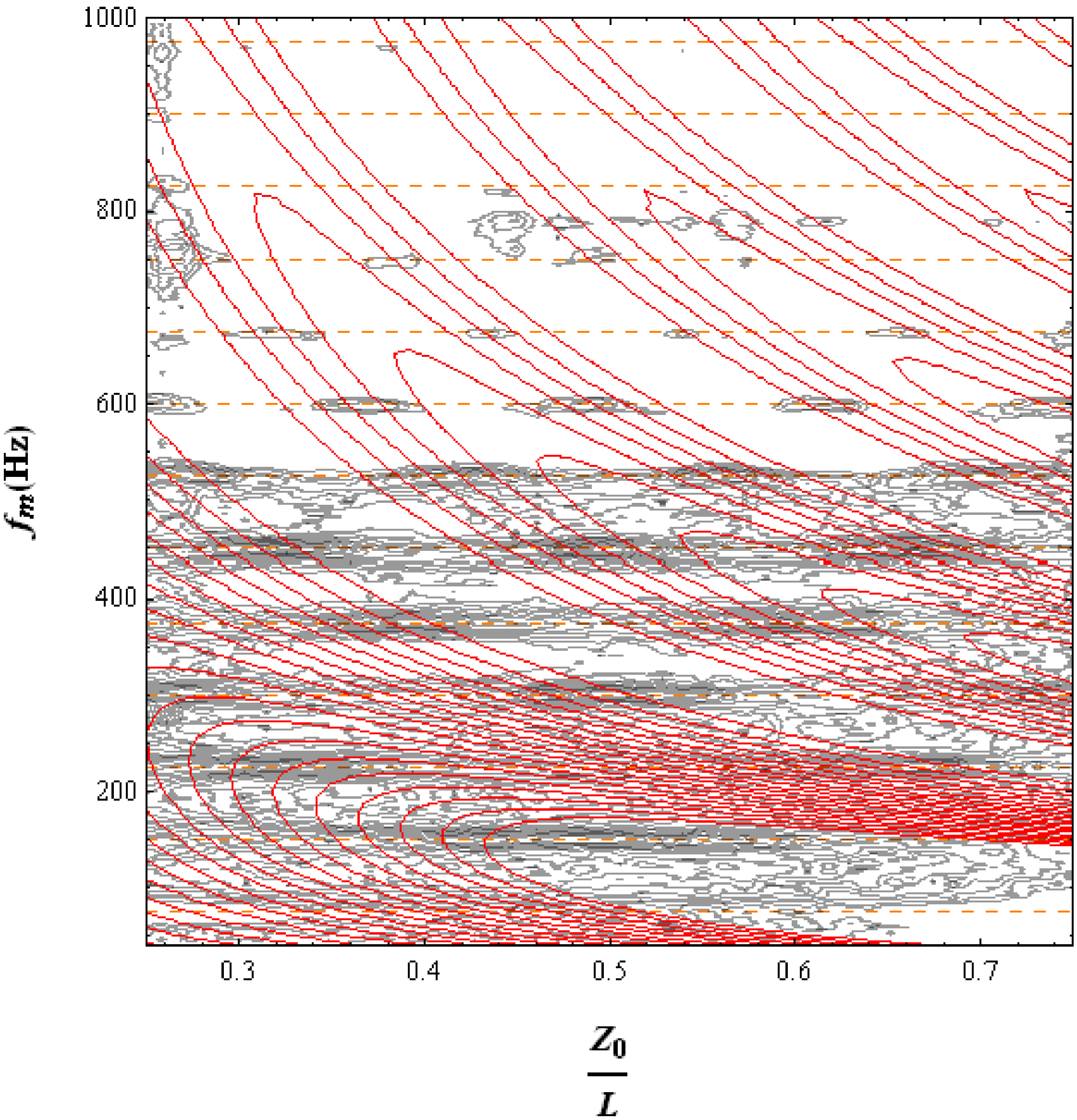

Figure B.12: Contour Plot of Spectral Data (black) and Contour Lines of α_{VS} (red), $R_0/R = 0.65$

B.1.5 Baffle with $R_0/R = 0.59$

Figure B.13 displays a 3-D surface plot of the sound pressure level as a function of the position Z_0/L and the oscillation frequency f_m. Figure B.14 shows a contour plot of spectral data, figure B.15 shows a contour plot of spectral data and contour lines of the theoretical growth rate α_{VS}. The dashed orange lines correspond to the (longitudinal) harmonics of the test chamber (multiples of 75Hz).

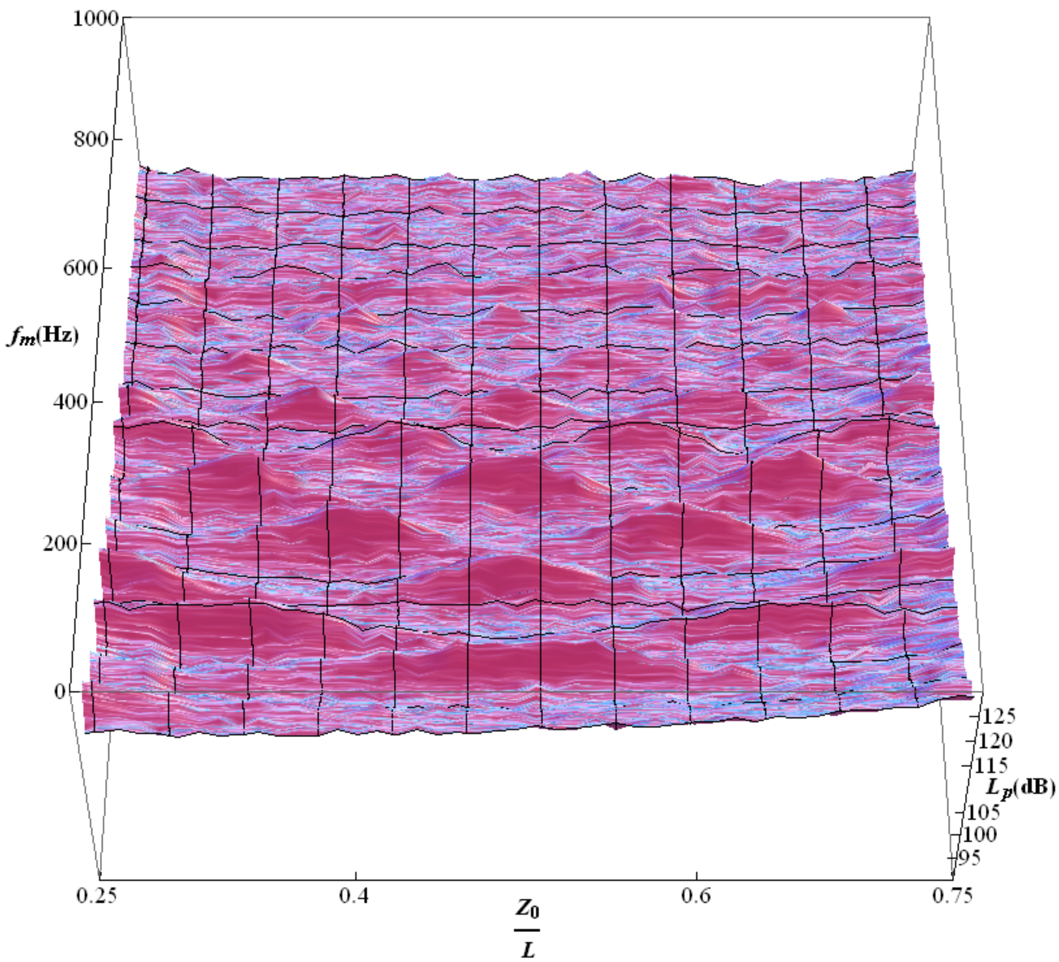

Figure B.13: 3-D Surface Plot of Spectral Data, $R_0/R = 0.59$

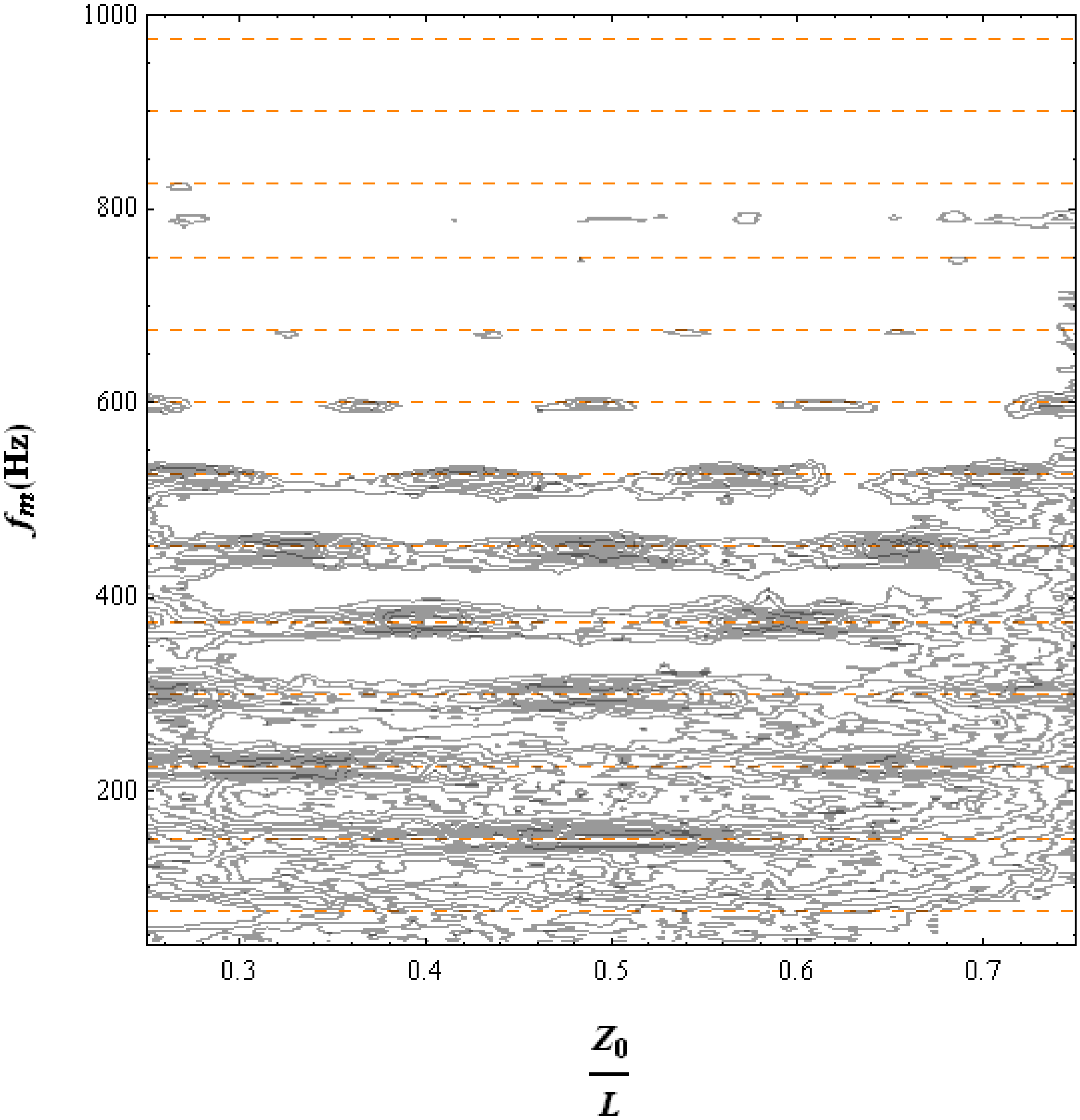

Figure B.14: Contour Plot of Spectral Data, $R_0/R = 0.59$

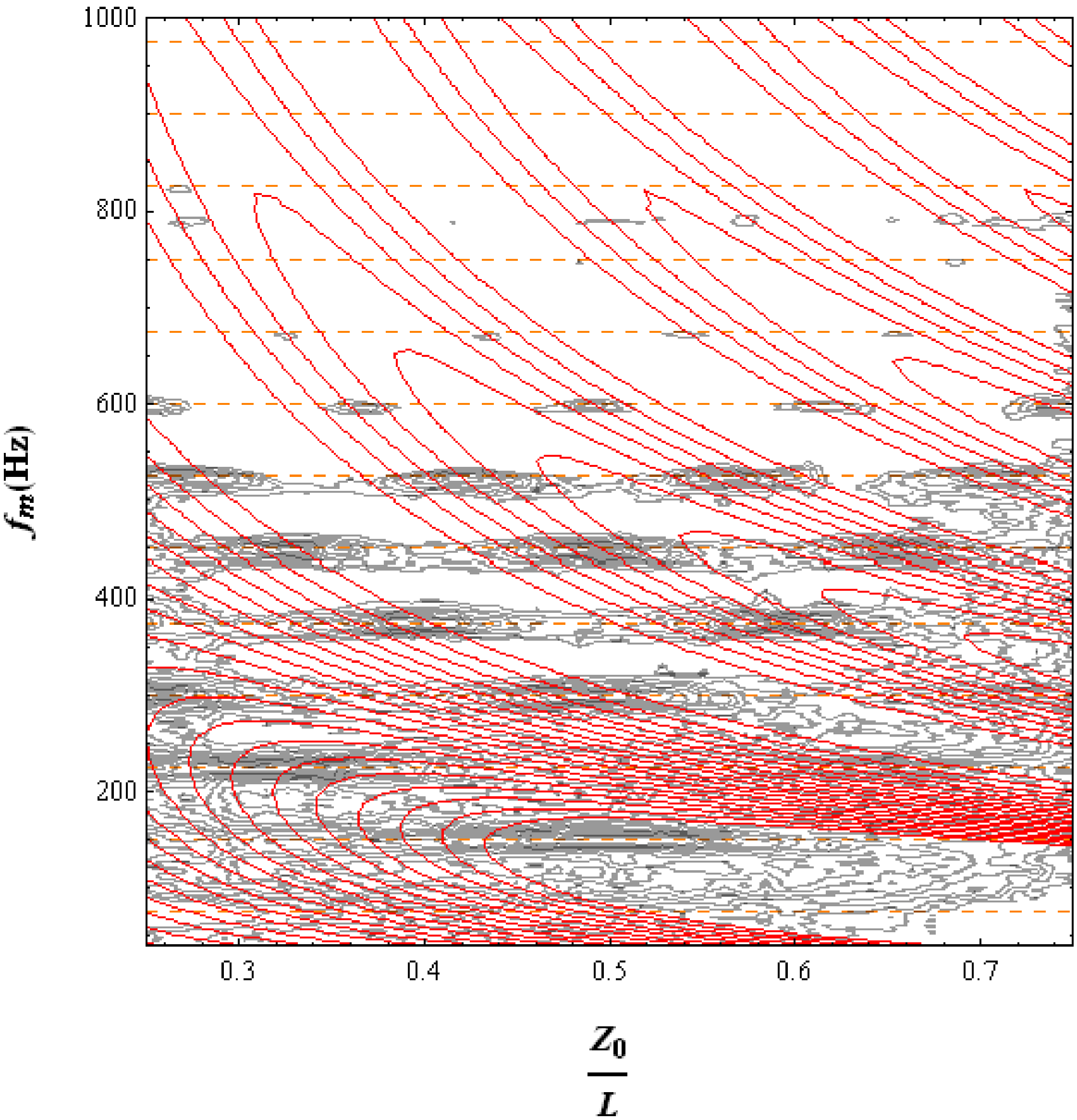

Figure B.15: Contour Plot of Spectral Data (black) and Contour Lines of α_{VS} (red), $R_0/R = 0.59$

B.1.6 Baffle with $R_0/R = 0.53$

Figure B.16 displays a 3-D surface plot of the sound pressure level as a function of the position Z_0/L and the oscillation frequency f_m. Figure B.17 shows a contour plot of spectral data, figure B.18 shows a contour plot of spectral data and contour lines of the theoretical growth rate α_{VS}. The dashed orange lines correspond to the (longitudinal) harmonics of the test chamber (multiples of 75Hz).

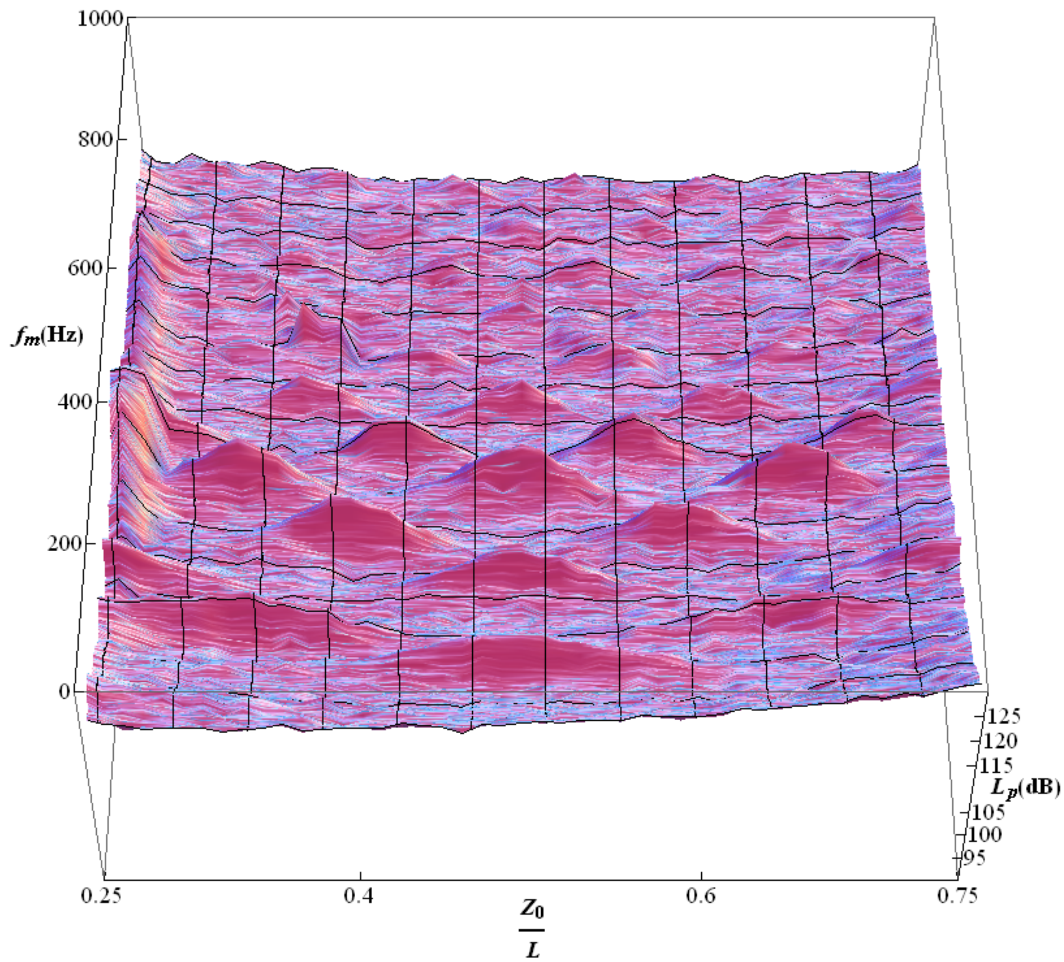

Figure B.16: 3-D Surface Plot of Spectral Data, $R_0/R = 0.53$

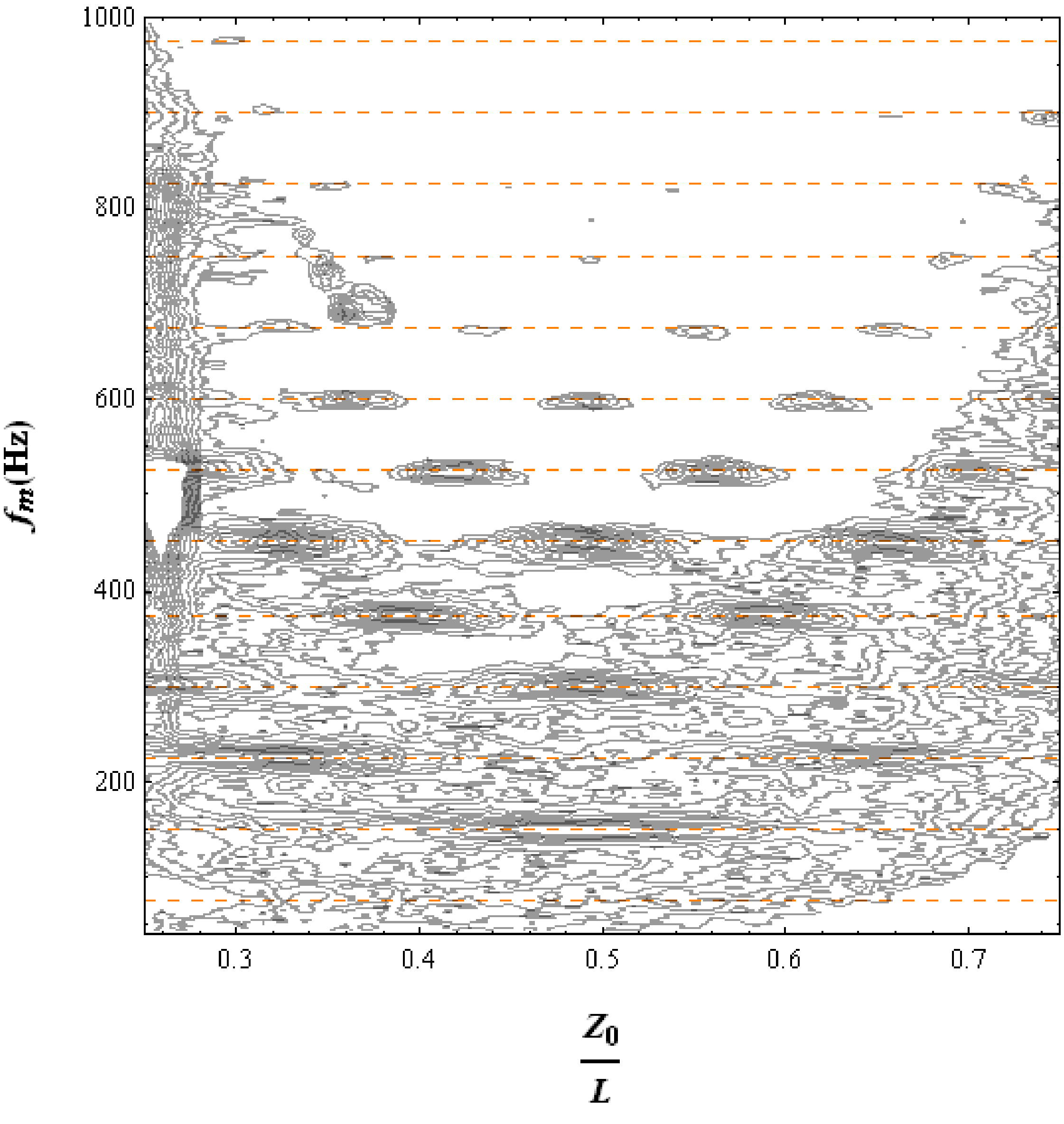

Figure B.17: Contour Plot of Spectral Data, $R_0/R = 0.53$

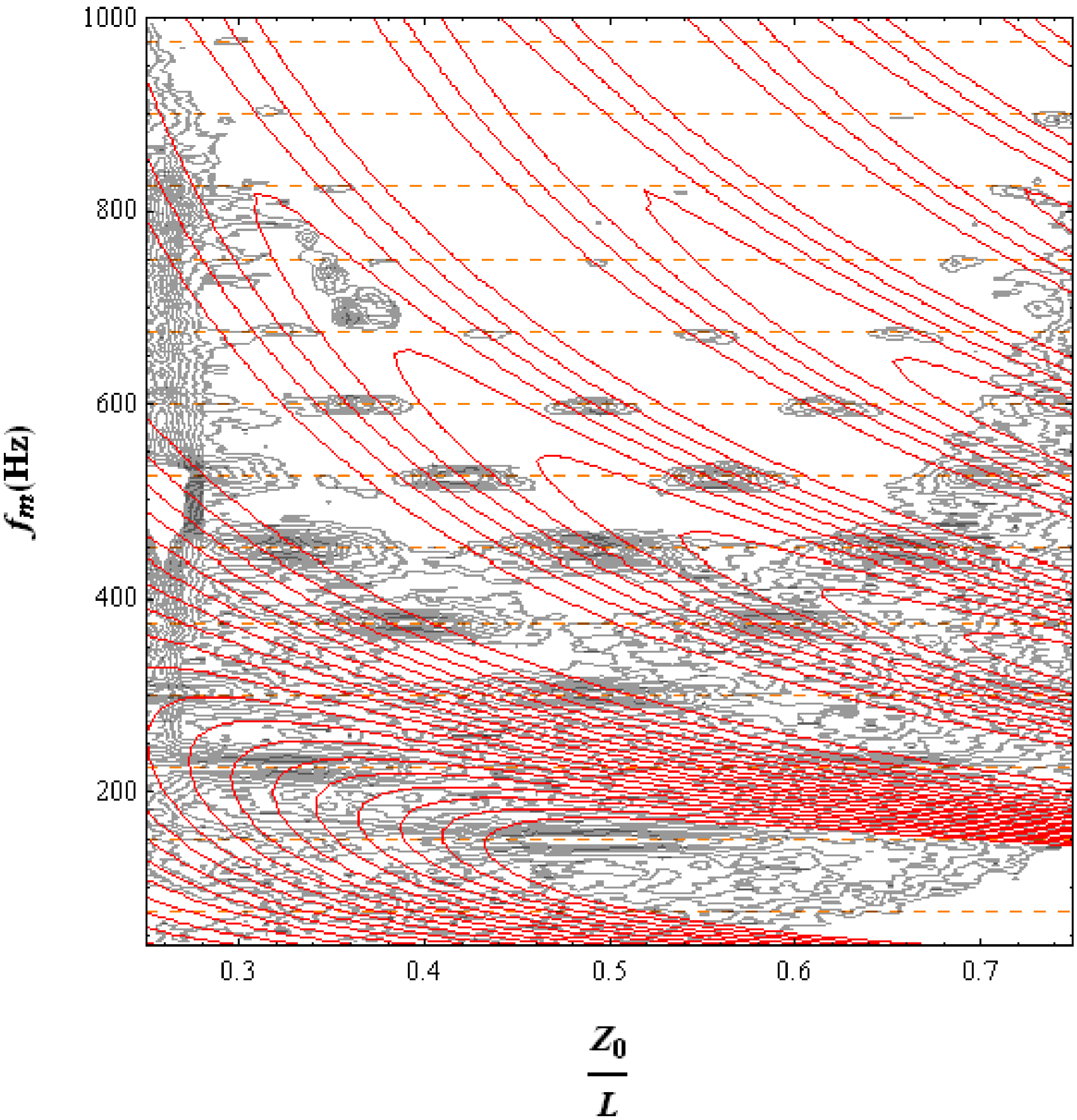

Figure B.18: Contour Plot of Spectral Data (black) and Contour Lines of α_{VS} (red), $R_0/R = 0.53$

B.1.7 Baffle with $R_0/R = 0.47$

Figure B.19 displays a 3-D surface plot of the sound pressure level as a function of the position Z_0/L and the oscillation frequency f_m. Figure B.20 shows a contour plot of spectral data, figure B.21 shows a contour plot of spectral data and contour lines of the theoretical growth rate α_{VS}. The dashed orange lines correspond to the (longitudinal) harmonics of the test chamber (multiples of 75Hz).

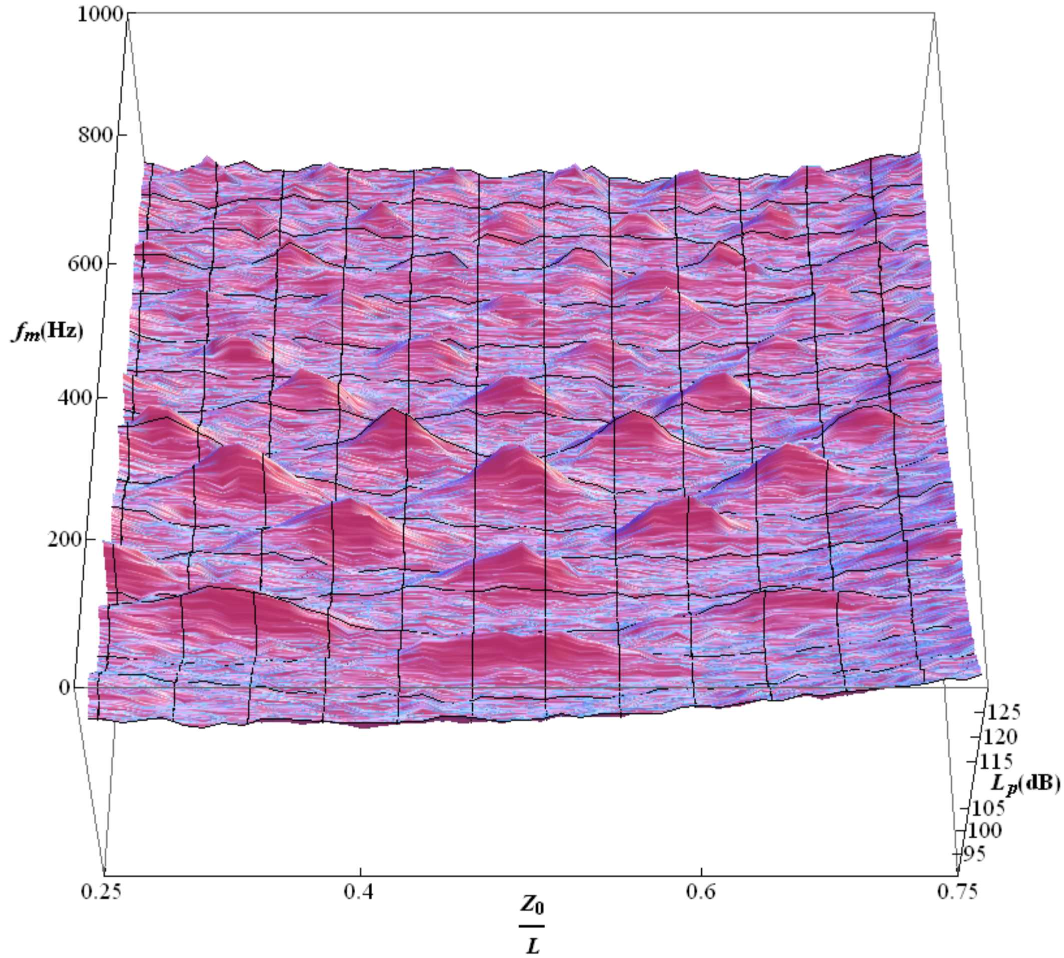

Figure B.19: 3-D Surface Plot of Spectral Data, $R_0/R = 0.47$

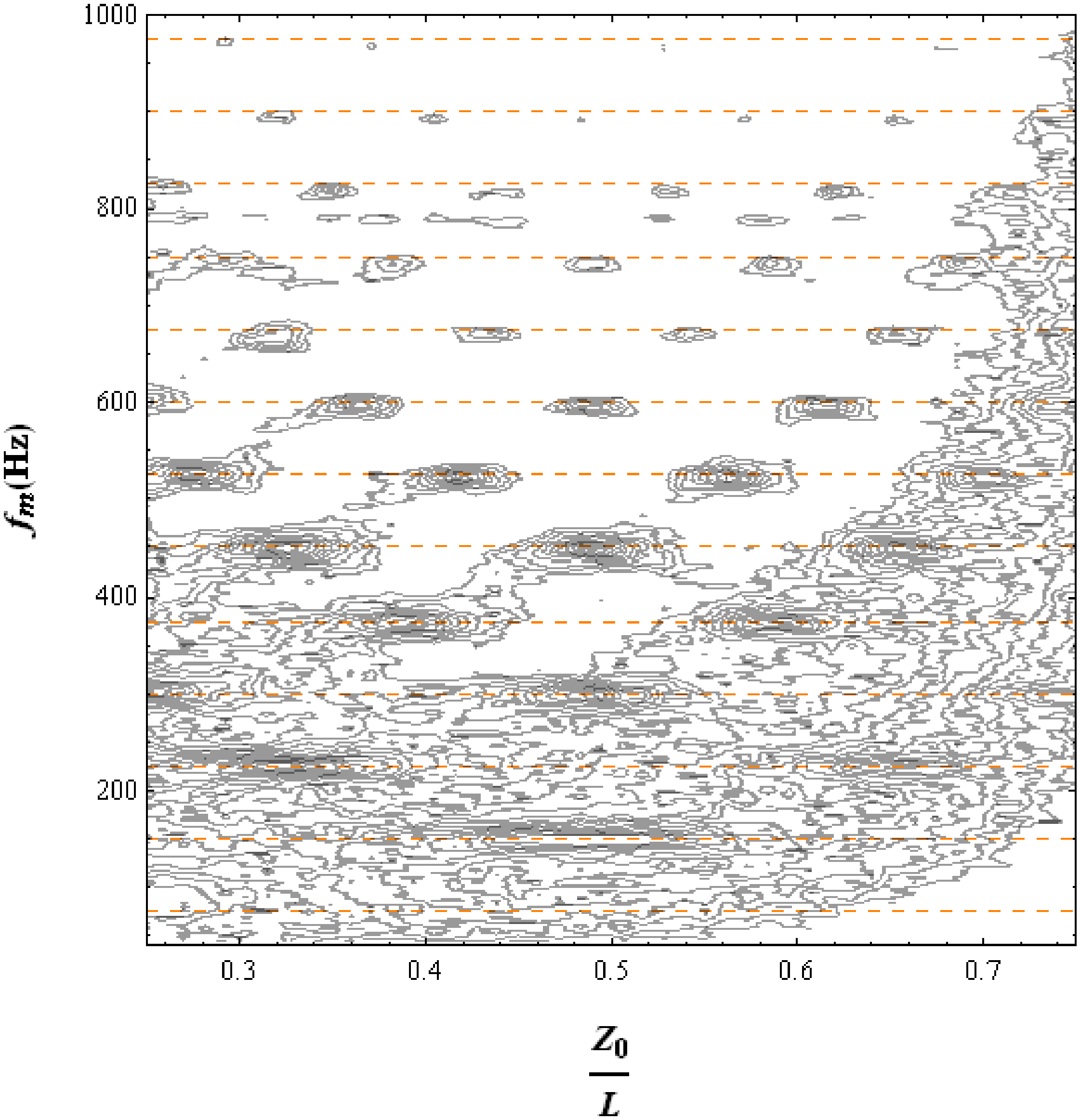

Figure B.20: Contour Plot of Spectral Data, $R_0/R = 0.47$

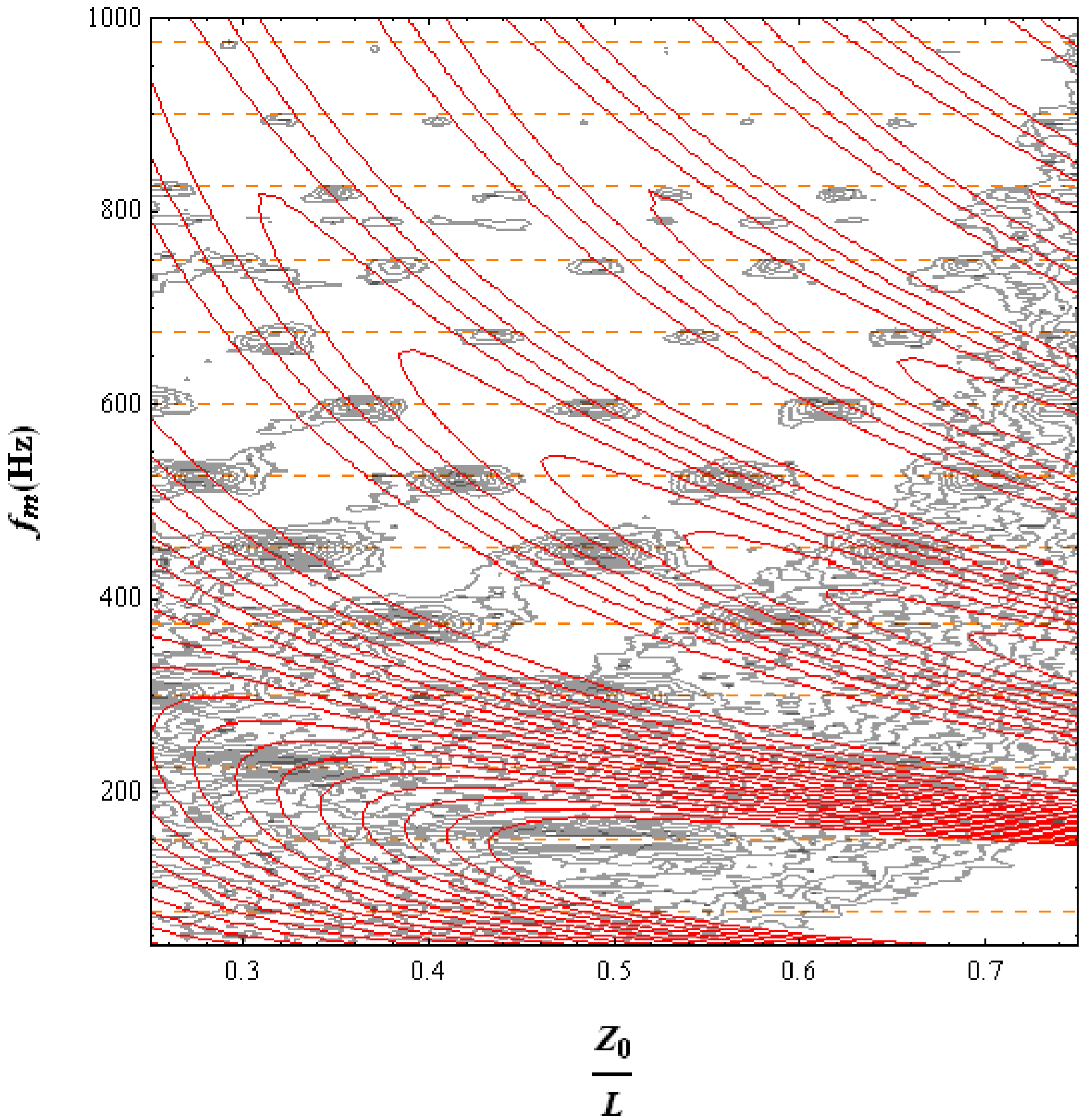

Figure B.21: Contour Plot of Spectral Data (black) and Contour Lines of α_{VS} (red), $R_0/R = 0.47$

Vita

Lutz Blätte was born in Offenbach am Main, Germany on April 24th, 1979. In 1998 he graduated from Wilhelm Dörpfeld Gymnasium in Wuppertal, Germany. After completing his national service working for the Hochschul Sozialwerk Wuppertal he began studying Mechanical Engineering at the Rheinisch-Westfälische Technische Hochschule (RWTH) Aachen in 1999. He finished his preliminary studies in 2002 and received his Vordiplom. He continued specializing in Aerospace Engineering and earned his “Diplom Ingenieur” from RWTH in 2007. His final thesis investigates the decay of the wake behind an airplane by running a RANS-simulation.

In the summer of 2007 Lutz joined the research group under Dr. Gary Flandro at the University of Tennessee Space Institute (UTSI). Under the guidance of Dr. Flandro he worked on the combustion instability phenomenon of large solid rocket motors approaching the problem both analytically and experimentally. In May of 2011 he recieved his PhD from UTSI.

Throughout his time at UTSI he served as a senator for the Student Government Association (SGA). He was elected in the summer of 2008 and re-elected in 2009 and 2010. Lutz also founded and presided over the UTSI Biking Club.